Università degli Studi dell'Insubria

Corso di Dottorato di Ricerca in Fisica e Astrofisica

PH.D. THESIS

Barred galaxies in cosmological simulations

Tidal perturbations and feedback

Candidate:
Tommaso Zana

Supervisor:
Prof. Francesco Haardt

Co-supervisor:
Prof. Massimo Dotti

Thesis accepted in 2018

"I am glad you are here with me.
Here at the end of all things"

Contents

List of Figures

List of Tables

Abstract

Bars are truly common objects among disc galaxies. Even though it is now commonly accepted that non-axisymmetric structures could deeply affect the life of isolated disc galaxies, by shaping their stellar and gaseous distribution, some fundamental aspects of their formation and growth are still debated. In particular, only recently, numerical simulations have reached the needed accuracy and technological level to detail such processes in a fully cosmological context.

The following manuscript is divided in two parts, in which I contribute to the study of bar formation and evolution through the use of state-of-the-art hydrodynamical and cosmological simulations.

In the first part of my work, I investigate the influence of tidal encounters on either unbarred, or already barred systems. To do this, I take advantage of two specific simulations belonging to the Eris suite – ErisBH and Eris2k – which evolve two Milky Way-sized barred galaxies in their cosmological volume. I both analyse the direct output of these simulations, and run a sample of new cosmological zoom-in simulations, by altering the original history of galaxy-satellite interactions in the ErisBH run. I study the major dynamical events in the evolutionary history of the galaxies, both to characterise the actual trigger of a non-axisymmetric perturbation and to evaluate the response of an already formed bar to subsequent encounters.

In the second part, I focus on the effect of the different feedback prescriptions implemented in the ErisBH and Eris2k runs. The enhanced feedback in the Eris2k case slows down the mass growth of the stellar disc and results in the creation of a very different bar structure with respect to its ErisBH counterpart.

My conclusions depict a scenario where, once the disc has grown to a mass large enough to sustain global non-axisymmetric modes, bar formation is inevitable and tidal encounters have, in general, a destructive effect on the two-fold overdensity, either by slowing down its growth, or by undermining its structural integrity. In addition, the self-gravity of the disc and its interplay with various internal processes (implemented in numerical simulations through sub-grid receipts), seem to be the main drivers of bar formation and growth. I confirm the importance of accurate feedback prescriptions in cosmological zoom-in simulations on the investigated processes, and propose a possible use of a statistical sample of barred galaxies to quantitatively assess this dependence.

Introduction

Amongst the wonders of the Universe, barred galaxies show some of the most fascinating beauty, maybe because of their dominant symmetry within the galactic disc. Figure 1 depicts one of the most popular and representative barred galaxy ever observed, NGC–1300, in the Eridanus Cluster, where all the elegance of this kind of objects immediately strikes the observer. However, not every bar is a massive large-scale structure as NGC–1300. Actually, they range from minimal nuclear structures, till the enormous systems which completely dominate the host disc and which cannot be studied just as simple perturbations of otherwise axisymmetric potentials. A wide variety of properties, such as their extent with respect to the galaxy, the possible presence of rings or spiral arms that directly arise from the bar itself, and the gaseous content of the host system, are usually catalogued in order to characterize bars, which can then be found in all types of disc galaxies along the Hubble sequence.

Figure 1: SB(s)bc galaxy NGC–1300; Hubble Space Telescope image.

Since the seminal papers by Hubble (1936) and de Vaucouleurs (1959), bars have been considered major actors in the long-term evolution of spiral galaxies (Binney and Merrifield, 1998; Elmegreen, 1998; Kormendy and Kennicutt, 2004; Combes, 2004; Kormendy, 2013). Indeed, they exert a significant torque over the material orbiting in the disc and, thus, allow both to redistribute angular momentum and to transport stellar and gaseous components on local and global scales (Tremaine and Weinberg, 1984; Lynden-Bell and Kalnajs, 1972; Athanassoula, 2003). The frequent occurrence of barred system, whose fraction measures more than 30 per cent of massive galaxies (Laurikainen, Salo, and Buta, 2004; Nair and Abraham, 2010; Masters et al., 2011; Lee et al., 2012; Gavazzi et al., 2015; Consolandi, 2016) when

observed in optical, but rises for near-infrared images (e.g. Eskridge et al., 2000; Menéndez-Delmestre et al., 2007), has promoted a wealth of observational and theoretical studies focussed on the effects that such non-axisymmetric structures can have on the galactic constituents. These include pre-existing components (e.g. Lütticke, Dettmar, and Pohlen, 2000; Bureau and Athanassoula, 2005; Kormendy, 2013) and newly formed stars (Ho, Filippenko, and Sargent, 1997; Martinet and Friedli, 1997; Hunt and Malkan, 1999; Laurikainen, Salo, and Buta, 2004; Jogee, Scoville, and Kenney, 2005), as well as diffuse gas (e.g. Sanders and Huntley, 1976; Roberts, Huntley, and van Albada, 1979; Athanassoula, 1992; Cheung et al., 2013; Fanali et al., 2015; Hakobyan et al., 2016) and dust (e.g. Consolandi et al., 2017).

Even though, by now, the study of bars and of their complex interplay with the host system has become a key factor in modern galaxy evolutionary theories, we are still far from a complete understanding of the precise dynamical nature of barred galaxies. Only today we are closing the technological gap which had hitherto prevented numerical simulations from accurately investigating some of the most puzzling problems. Moreover, the distance of the objects, the impossibility to observe a galaxy with more than one line of sight, the parametrization of the dark matter contribute, etc. remain hardly-to-overcome issues and make even observations rarely able to provide the precise three-dimensional mass distribution of a galaxy (hence its potential), thus leaving the outcomes of the latest computational experiments still unconstrained.

In this work I contribute to the study of the processes of bar formation and evolution, by means of state-of-the-art numerical simulations. In chapter 1, I introduce the subject of galactic bars, starting from the Hubble morphological classification and discussing both the main observational properties of bars and their known effects on the host environment. In chapter 2, I provide a brief analytical description of barred potentials in the epicycle approximation and define some fundamental quantities needed for the following analysis. In chapter 3, I outline the role of N-body simulations in modern-day investigations and the latest theories about the origin and the growth of bars. The set-ups of the cosmological simulations analysed are detailed in chapter 4, along with the architectures of the adopted codes. The study of the simulation outputs are presented in the following three chapers. In particular, in chapter 5 and chapter 6, I focus on the effects that tidal perturbations have, either on an axisymmetric galaxy, or on an already barred system, respectively. In chapter 7, I study the influence of different sub-grid prescriptions on large-scale bars and, finally, I draw my conclusions in chapter 8.

Chapter 1

Barred galaxies: morphology and observations

In this introductory chapter, I review the basic observed properties of bars and their hosts. In particular, in § 1.1, I introduce the morphology classification of galactic objects, which is necessary in order to discuss how the observative campaigns contribute to our understanding of barred systems (§ 1.2). Finally, in § 1.3, I summarise the main effects induced by bars on their galactic hosts.

1.1 Classification

The morphological classification, proposed by Hubble in 1926 (Hubble, 1926), completed in 1936 (Hubble, 1936) and then further developed (the final version is shown in Figure 1.1), divides regular galaxies into three main classes based on their visual appearance: ellipticals, lenticulars and spirals. There is also a

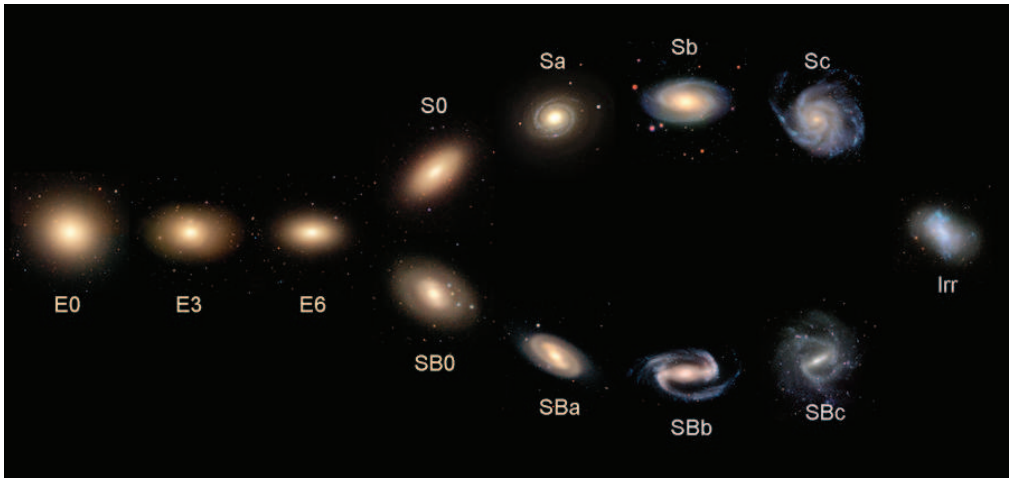

Figure 1.1: Enriched Hubble's classification scheme.

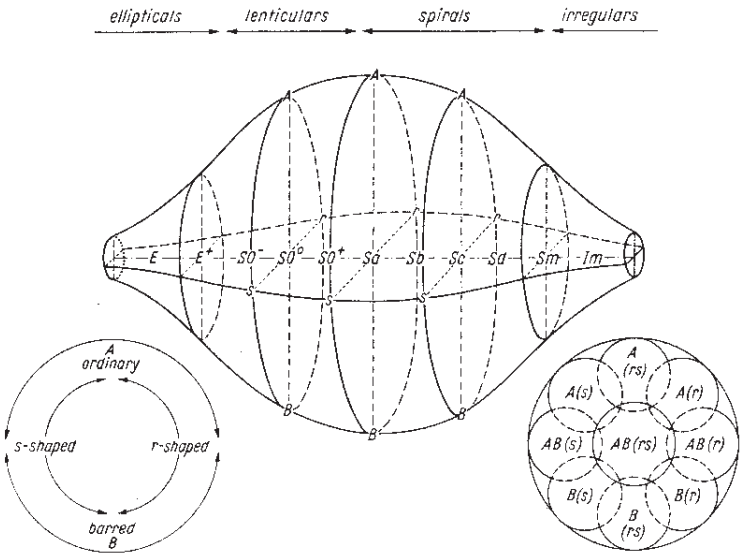

Figure 1.2: Three-dimensional scheme proposed by de Vacouleurs in 1959 for galaxy classification (de Vaucouleurs, 1959).

fourth class containing galaxies with an irregular shape. Ellipticals are marked with the letter E and separated among them with a number ranging from 0 to 7 to identify the ellipticity degree (E0 galaxies are almost spherical, while E7 are highly flattened). Lenticulars, named S0 and SB0, have a disc-like structure with a central spherical bulge and do not exhibit any spiral pattern. Each of these two types is further divided into three subclasses designated by the indices 1, 2, 3. The SB0s show a bar that crosses the nuclear region and their subclass is defined according to the prominence of this bar; for the S0s, subclassification is determined by the presence of gas and dust in the disk. Otherwise, spiral galaxies are marked with letter S and divided into two families: the barred spirals (SB) and the classic ones (S). Each of these classes is then characterized by a letter to indicate the arms aperture and the bulge importance (from 'a' to 'c' to mark an even increasing arms aperture and reduction of the bulge size). Elliptical and lenticular galaxies form the category of early type galaxies, while spirals belong to the late type galaxies. Although this nomenclature could suggest otherwise, Hubble was not intended to indicate any evolutionary scenario with his classification: this is still debated.

However, the great variety of morphological features found across all categories required the classification to be more precise and detailed. This is the case of the classification scheme introduced by Gérard de Vaucouleurs in 1959 (de Vaucouleurs, 1959) and widely used as an extension for the Hubble sequence. In this system de Vaucouleurs (Figure 1.2) adopted Hubble's main classification into elliptical galaxies, lenticulars, spirals and irregulars, but introduced a more elaborate organization for spiral galaxies based on three distinct morphological features, namely the presence (or absence) of the bar, rings-like structures and spiral arms. In the new description, though it remains still a subjective classification criterion, the morphological bin has been refined admitting the intermediate categories 'ab', 'bc' and 'cd' among the previous ones according to the tightness

of the spiral arms; the notation SA is introduced to indicate the classical spiral galaxies along with the barred ones (still identified by the Hubble's notation SB). It was also included an intermediate class (SAB) for slightly barred galaxies. Even Lenticular galaxies are separated between Barred (SB0) and classic (SA0) and notation S0 is exclusively reserved for those objects in which the presence of a bar could not be detected (this is often the case of an edge-on observed galaxy). Moreover, galaxies are also discriminated depending on the presence of rings-like structures (r), their absence (s) or the usual intermediate case (rs). The new classification includes different additional spiral classes (and their relative barred counterparts): the Sd galaxies (SBd), i.e. diffuse galaxies with clumpy arms and a very tenuous central bulge, the Sm[1] galaxies (SBm), irregular galaxies apparently without any evidence of a bulge and Im galaxies, or very irregular galaxies with no recognizable structures.

Figure 1.3: Typical disc galaxy NGC–2903, SB(s)d. Hubble Space Telescope image.

In this work I will focus on disc galaxies, that are spirals and lenticulars. These type of objects show sometimes a more or less pronounced bulge, mostly composed by older stars (Population II[2]), but their main component is a large rotating disc relatively thin, consisting of young stars, variable amounts of gas (mostly molecular and atomic hydrogen) and dust. All these peculiarities are evident in Figure 1.3. The distinctive feature of this kind of galaxies is definitely the fundamental role of the angular momentum, which gives the object its characteristic axisymmetric shape, separating it from the other morphological type, the ellipticals, whose mass distribution is determined by the isotropic motion of the stars. Discs and bulges are embedded within a dark halo which encompasses the vast majority of the galactic mass. It extends well beyond the edge of the visible galaxy and is connected to the neighbouring haloes through long dark matter (DM) threads.

The formation and growth of a flat astrophysical systems supported by rotation, like the galactic disc of Figure 1.3, are slow, adiabatic processes (Choi et al., 2006). They occurs through the dissipational collapse of a gas cloud which originally had a non-zero initial angular momentum and for which radiative cooling is very effective. Such a cloud will radiate away its binding energy and shrink, approaching its lowest-energy state. If the radiation field originated from cooling is roughly isotropic, it does not carry away much

[1]The The "m" stands for "magellanic" since the prototype of this type of galaxies is the Large Magellanic Cloud.

[2]Stellar population class is assigned through the analysis of the stars chemical composition. The Population II stars are very ancient objects that formed in the early Universe, when it contained only small fractions of elements other than hydrogen and helium.

angular momentum, causing the cloud to conserve it during the contraction. The final structure is a rotating disc, since in such configuration the angular momentum of each mass element points in the same direction (the angular momentum in the other directions has been cancelled out), whereas the density distribution is determined by the efficiency of the angular momentum transfer process (viscosity may play an important role in regulating this transfer; see, e.g. Mo, van den Bosch, and White 2010).

Many disc galaxies own a central bulge, i.e. a smooth ellipsoidal[3] concentration of stars, which stands out compared to the flatness of the disc. The formation of the bulge is not fully understood, but today it is largely accepted the difference between (i) classical bulges, resembling small elliptical galaxies and presumably formed in an analogous way,[4] and (ii) *pseudobulges* (see, e.g., Kormendy and Kennicutt, 2004), slowly formed through secular dynamical processes and strictly connected to the presence of a bar (see § 3.4.1).

Provided that the galaxy has enough time to evolve (without any violent encounter with other comparable-mass objects), inner disc dynamical processes could trigger a self-powered reaction which makes many stellar orbits precede together, giving rise to some periodic patterns, such as spiral arms, or galactic bars. From a structural perspective, bars can be viewed as a triaxial bulge, hence the distinction between these two stellar systems is very fleeting. Indeed, Hubble morphological definition depends basically on the view angle.

1.2 Observations

Since the first detections, it was therefore clear that self-gravitating discs were able to sustain long-lasting structures such as bars. Over the years, the development of observational techniques allowed to significantly improve our knowledge of these common objects.

1.2.1 Imaging

Mapping the light distribution of a galactic objects gives a lot more than a simple, albeit lovely, image, as those in Figures 1 or 1.3. Despite DM is an omnipresent component, which dominates the galaxy dynamics in its outer parts, the potential well remains effectively constrained by the visible matter in the central kpc, and this is a great advantage to study the structures forming in the inner disc.

Given the inherent asymmetry of a barred galaxy, some procedures, such as the extraction of a luminosity profile and the deprojection of the image are much harder for a strong barred object with respect to a completely axisymmetric system. In general, the inclination of the system is deduced from the galactic

[3] Bulges and elliptical galaxies are frequently addressed as spheroidal stellar systems, even though their shape is not necessarily close to mathematical spheroids.

[4] I.e. through violent events, as mergers between two progenitors of comparable mass (major mergers), when the release of orbital energy highly boosted the star formation (SF from now on) rate in the gas clouds of the progenitors.

axis ratio[5] in the outer regions, as far as possible from the bar influence range. This can be made since the bar major axis is always shorter than the diameter of the host galaxy, with a dependence on the morphological type (the earlier is the type of the galaxy, the higher is the ratio between the bar length and the host galaxy size; see, e.g. Athanassoula and Martinet, 1980; Elmegreen and Elmegreen, 1985).

For similar reasons, even the extraction of the information on the bar (e.g. the luminosity fraction of the stellar bar over the whole galaxy) within the host disc is a delicate operation and does depend on the model used for such the decomposition. Among the employed methods (e.g. Crane, 1975; Duval and Athanassoula, 1983; Blackman, 1983), the Fourier decomposition of the light distribution (that also corresponds to the main strategies applied in the numerical simulations discussed in this work; see § 3.2) is one of the most successful procedure (originally proposed by Elmegreen and Elmegreen, 1985), since it does not assume any particular shape for the components and it easily supplies some fundamental parameters of the non-axisymmetric structures investigated, such as the strength and the size.

As discussed in § 1.1, in (near) face-on projected galaxies, the bar is easily discernible and an analysis can be performed on the light distribution as a function of the distance from the centre of the system. On the contrary, in edge-on galaxies, even though the imaging would give fundamental information in order to study the otherwise unknown vertical profile of the structure, a bar would be unnoticed.
In this kind of objects, the central bulge (when this is present), is not always identified with a simple spheroidal or ellipsoidal component, but frequently appears to be more "boxy" or "peanut-shaped" (or even X-shaped in some cases). It was proposed by Combes and Sanders (1981) that these particular stellar overdensities are closely related to the presence of a bar when this is seen edge-on. It was later suggested that these so called "boxy/peanut" bulges are the direct result of a vertical instability, occurring within the bar itself (Athanassoula, 2008a, e.g.), which thickens the central part of the structure and decouples it from the disc (see also § 3.4.1.1).

1.2.2 Spectroscopy

The kinematics of galaxies is commonly investigated through spectroscopy by subtracting the cosmological redshift and measuring the Doppler shift due to the relative motions of emission (or absorption) lines from the gaseous and stellar constituents. Whereas the multitude of emitting components in the system (stars, dust and various molecules with different bound energy) allows to probe the motions at different galactic radii,[6] when the gas fraction is prominent in

[5] It is assumed the galaxy to be a perfect circle with a certain projection angle. Nonetheless, this is not always true, since the disc could be intrinsically elliptical or could bring the signs of some dynamical perturbation.

[6] For instance the HI line at 21 cm is emitted farther with respect to the galaxy optical radius and its observation is the techinique that permits to map the kinematics at the largest distance from the centre.

the galaxy (such as in a late-type galaxy), the kinematics is usually measured via the bright emission lines of the gaseous medium. On the other hand, the limited amount (if any) of gas in early-type galaxies forces to focus on the stellar motion and this is done by measuring the width of the typical absorption lines of stellar atmospheres such as the H, K lines or the Na, MgII or CaII triplet.

Spectroscopic measures are often necessary in order to discriminate between late and early-type galaxies. Although, it is clear that the former are rotationally supported systems, the classification of early-type galaxies has not been always straightforward because of the confusion among ellipticals and lenticulars. Unless clear disc features (e.g. spiral arms or bars), a face-on projected elliptical, supported by the random motion of its stars, would be indistinguishable from a rotating disc, if the kinematics data are not available.

The main difference in the velocity fields between barred and unbarred galaxies, is the presence, in the former systems, of significant non-circular streaming motions, especially in the region dominated by the bar (Kormendy, 1983). Even though these features are clearly difficult to detail, for the non-axisymmetric distribution of the mass (hence of the light), it is nowadays evident that a bar can exert a sufficiently strong torque in order to force the stars and the gas to flow on elongated orbits along the bar.

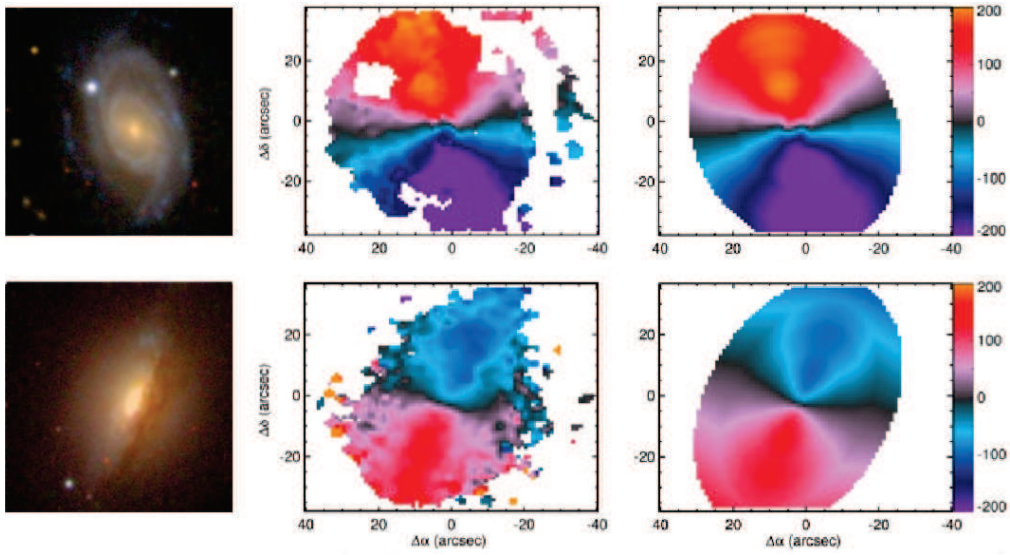

Figure 1.4: Comparison between NGC–7321, SBc galaxy (top row) and the axisymmetric NGC–1056, SAa galaxy (bottom row). From left to right: SDSS (igr) composite images with a side of 2 arcmin, H_α velocity fields from the CALIFA survey, and related two-dimensional fits. The complete figure is provided by Holmes et al. (2015). The bar of NGC–7321 clearly induces non-circular motions visible both in the H_α velocity map and in the corresponding fit with the 'S-shaped' feature along the minor axis in the central 20 arcsec.

The study of the kinematics of gas (rather than of stars, since gaseous emission lines are easier to measure with respect to the weaker and broader stellar absorption lines) produced in the years undisputed evidences of these

stream flows (see, e.g., Weiner, Sellwood, and Williams, 2001; Hernandez et al., 2005; Spekkens and Sellwood, 2007; Sellwood and Sánchez, 2010).

A notable case is provided by Holmes et al. (2015), where the authors adopt the software DISCFIT (Reese et al., 2007) in order to fit the H_α velocity maps of all the intermediate-inclination gas-rich CALIFA[7] DR1 galaxies (Husemann et al., 2013; Walcher et al., 2014).

The velocity maps (middle panels) of a barred (NGC–7321, top row) and an unbarred galaxy (NGC–1056, bottom row) are compared in Figure 1.4, next to their best fits (right-hand panels; see Holmes et al., 2015). In the non-axisymmetric case, the best fit is a bisymmetric model which takes into account the presence of non-circular flows along with the standard rotation of the disc. The manifest 'S-shaped' formation in the central region of NGC–7321, represents an unequivocal trace of the gas inflows caused by the bar.

The peculiar density distribution in a barred galaxies makes it non-trivial also the evaluation of the galaxy rotation curve. A common approximation is applied by azimuthally averaging tangential velocities, but the method brings important uncertainties both on the value of the rotation velocity and on the position of the bar resonances. As a consequence, even orbital resonances are hardly determined in barred galaxies.
In addition, a resonance expected according to the linear theory (when the bar can be considered as a small deviation from axisymmetry) could be absent in the case of a strong bar.

A fundamental step towards the characterization of a barred galaxy is the measure of the pattern speed. The measure is quite problematic in general, since only in a minority of cases it can be carried on directly. When this is not possible, the continuity equation can be used for the purpose, according to (Tremaine and Weinberg, 1984).
Although the procedure (that requires also a photometric light profile) works both in simulations and observations, it has a high margin of error, since the method depends, e.g., on the accuracy of the alignment and on the presence of bright spots and dust patches in the disc.

1.3 Bar effects

Bars are now well accepted to be the main driver of *secular evolution*, which is the slow evolution of a galactic system that does not suffer any collision with other objects of comparable mass (see, e.g., Binney and Merrifield, 1998; Elmegreen, 1998; Kormendy, 2013; Sellwood, 2014, for extensive discussions).

We have seen that, given their non-axisymmetric structure, bars can exert a torque over the gas (especially in late-type galaxies) and the stars orbiting in the disc (and also over the DM halo, as observed, e.g., by Athanassoula, 2005a; Athanassoula, 2007; Colín, Valenzuela, and Klypin, 2006). As a consequence,

[7]The Calar Alto Legacy Integral Field Spectroscopy Area (CALIFA) survey uses the PPaK mode of the Potsdam Multi Aperture Spectrophotometer (PMAS) IFU on the 3.5 m telescope at the Calar Alto observatory.

strong gaseous inflows are triggered toward the centre of the galaxy, with all the related effects on the potential.

The migration process is usually accompanied by the presence of dark narrow lanes, where the dust gets denser, as it is clear for NGC–1073 in the left panel of Figure 1.5. The bar produces shocks where it meets the interstellar medium, which orbits slower than the bar pattern (i.e. at shorter radii than the corotation radius, where the rotation curve of the whole galaxy equals the bar pattern speed; see § 2.4). There the density of the material increases to several times the normal value and produces strong emission (or absorption, in the case of dust).

As it is clear from the beautiful composite images in Figure 1.5, the distribution of blue, young stars and HII regions is not homogeneous, but it is concentrated near the galactic centre (e.g. Hummel et al., 1990) and at the terminal edges of the bar. Some recent works show that both the past and the current SF activity are higher in the central regions of barred galaxies with respect to unbarred systems (see, e.g., Ellison et al., 2011; Coelho and Gadotti, 2011). Molecular gas accumulates where the bar ends and reaches density levels high enough to trigger bursts of SF that rapidly depletes the remaining material, making the region inside the corotation gas-poor[8] (see, e.g. Krumholz and McKee, 2005; Krumholz, McKee, and Tumlinson, 2009; Daddi et al., 2010; Genzel et al., 2010). A typical feature of barred galaxies, noticeable in the right example of Figure 1.5, is the build-up of gaseous material in rings when the gas inflow stops before reaching the very central part of the disc. As long as new cold gas is brought in the area, these structures are active SF regions and have been proposed as proxy for the position of the Inner Lindblad Resonance[9], since this would define the inner end of the bar (Combes et al., 2014).

On a longer timescale, once the gaseous reservoirs have been depleted, the SF efficiency is locally quenched (Cheung et al., 2013; Gavazzi et al., 2015; Consolandi et al., 2017; Khoperskov et al., 2018, e.g.). The evolution of isolated galaxies[10] is regulated by an intricate interplay among the processes able to consume (or remove) their reservoir of gas. Bars are major actors in this scenario and are currently claimed to be a fundamental phase in the metamorphosis from a star-forming blue galaxy to a "red and dead" object with very little gas amounts.

The strong inflow of gas has also been proposed as possible a feeding mechanism of the central massive black hole (MBH) (see, e.g., Simkin, Su, and Schwarz, 1980; Noguchi, 1988; Shlosman, Begelman, and Frank, 1990; Combes, 2000; Jogee, 2006; Emsellem et al., 2015; Cisternas et al., 2015), but this idea is

[8] As it will be discussed in chapter 2, the corotation radius represents the outer edge of the bar.

[9] The Inner Lindblad resonance (ILR) is an orbital resonance occurring where the epicyclic frequency (the radial oscillations frequency of an element whose circular orbit has been perturbed) of an object embedded in the potential is equal to twice the difference between the angular speed, depending on the disc radius, and the fixed frequency of the bar. See § 2.4 for a deeper explanation.

[10] When a galaxy evolves in isolation, the effects of the environment, such as the ram pressure, due to the intergalactic medium, or various tidal perturbation, exerted by companion galaxies, are negligible with respect to the internal processes.

Figure 1.5: SB(rs)c galaxy NGC–1073 (left) and SB(r)0 galaxy NGC–6782 (right). Hubble Space Telescope images.

still a matter of debate (see, e.g., Alonso, Coldwell, and Lambas, 2013; Cheung et al., 2015; Goulding et al., 2017).

As previously discussed, when an ILR is present, the gas is likely to shock around its radius, producing the characteristic ring. However, if the inflows accumulate enough mass at the resonance radius, a possible newly formed nuclear bar can eventually bring the gas closer to the galactic centre in a cascade-like fashion (Shlosman, Frank, and Begelman, 1989; Maiolino et al., 2000).

Finally, one of the most relevant product of the bar-driven inflows toward the galactic centre and of the resulting SF bursts is the creation of a central mass concentration (hereafter CMC). Not only the funneled gas and the newly formed stars contribute to this CMC, but a considerable amount of old stars are driven inwards as well (Grosbøl, Patsis, and Pompei, 2004). Such dynamical system is often characterized by a thick disc-like shape, that rapidly rotates and is therefore different from the classical, pressure supported bulges. For this reason, it is called *pseudobulge* or *discy bulge*, given its resemblance to the progenitor disc from which it originates (Kormendy, 1993; Kormendy and Cornell, 2004; Kormendy and Kennicutt, 2004; Athanassoula, 2005b).

This structure should not be confused with the boxy/peanut-bulges that arise via the direct vertical instability of the bar (see § 3.4.1.1).

In conclusion, bar-drive gas inflows strongly affect the inner galactic environment. The process has been observed in both theoretical and observational works (see e.g. Combes and Gerin, 1985; Athanassoula, 1992; Sellwood and Wilkinson, 1993; Piner, Stone, and Teuben, 1995; Sakamoto et al., 1999; Rautiainen and Salo, 2000; Regan and Teuben, 2003; Athanassoula, 2005b; Sheth et al., 2005; Wozniak, 2007; Knapen, 2007; Kim et al., 2012; Cole et al., 2014; Fanali et al., 2015; Emsellem et al., 2015; Sormani, Binney, and Magorrian, 2015) and makes bars the main actors in secular evolution, which is expected to dominate the growth of a galaxy after the peak of SF, occurring around $z = 2$.

Chapter 2

Bar dynamics

In this chapter I describe some fundamental topics of the dynamics of stars embedded in barred potentials.

After a brief introduction on the n-body problem, I discuss the epicycle approximation in axisymmetric systems in § 2.2. In § 2.3, I review the dynamical case of bars in rotating potentials, defined as small deviations from axisymmetry. In § 2.4, I conclude by deriving, in the same simple case, the orbital resonances.

2.1 Introduction

The density of stars in galaxies is globally very low and, for this reason, the orbit of an individual particle is essentially not perturbed by the single stars, but is determined only by the large-scale gravitational potential of the whole system. A parameter is used to quantify the effect of the "granularity" of a system over the star orbit: the relaxation time is the time taken to change the velocity of a star, during an entire orbit, by an amount equal to the stellar velocity dispersion of the galaxy. In this context, the general motion of the star is determined by the main galactic potential, whereas the variation is due to the cumulative gravitational perturbations induced by the random distribution of the other single stars (Chandrasekhar, 1941). The relaxation time assumes an enormous value in typical disc galaxy environments, thus the distribution of stars can be well approximated by the Boltzmann collisionless fluid equation

$$\frac{\partial P}{\partial t} + \boldsymbol{v} \cdot \nabla P - \nabla \Phi \cdot \frac{\partial P}{\partial \boldsymbol{v}} = 0, \tag{2.1}$$

where ϕ is the gravitational potential and the distribution function $P(\boldsymbol{x}, \boldsymbol{v}, t)$ is the mass in a volume element of phase space $\boldsymbol{x}, \boldsymbol{v}$, divided by the element volume. The fluid approximation is valid by considering an arbitrarily large number of stars with arbitrarily low mass.

The connection between the potential Φ and the distribution function is obtained via the Poisson's equation

$$\nabla^2\Phi(\boldsymbol{x},t) = 4\pi G\rho(\boldsymbol{x},t), \tag{2.2}$$

with G, gravitational constant and ρ the volume density, which is the integral of P in the phase space over the velocities as in Equation

$$\rho(\boldsymbol{x},t) = \int_{-\infty}^{\infty} P(\boldsymbol{x},\boldsymbol{v},t)d^3\boldsymbol{v}. \tag{2.3}$$

These equations are impossible to solve analytically for realistic, rotating, non-axisymmetric potentials. For the related mass distributions, the stars do not possess a number of integrals equal to the number of spatial dimensions. As a consequence, bars can only be treated as near-integrable systems and the equations solved numerically.[1]

2.2 Epicycle frequency and epicycle approximation

It is possible to provide an analytical simplified description of the orbits in a barred potential for a weakly perturbed case (the following method is based on Binney and Tremaine, 2008). Even though the problem of a strong bar cannot be outlined within such a linear theory, the results do provide useful and fundamental insights that are still valid in the more realistic cases.

Those stars whose motion is confined to the equatorial plane of an axisymmetric potential (like a disc galaxy) experience a force directed toward the centre of the disc. The radial coordinate R of a star affected by this force oscillates between two extrema during its motion of revolution around the centre, and the orbit forms a rosette figure as the one in Figure 2.1.

Before proceeding further, it is fundamental to introduce a few concepts about the epicycle frequency.

A radially displaced object oscillates according to its epicyclic frequency while it revolves. In axisymmetric potentials many stars follow nearly circular orbits. For this reason, an approximate solution to their equations of motion is usually adopted and I will apply the result to further simplify the case in a rotating non-axisymmetric case (see § 2.3).

To derive the following relations it is convenient to neglect the motion of stars perpendicular to the galactic plane.[2]

According to the obvious cylindrical coordinate system (R,φ) in the plane, let Φ_{eff} be the standard effective potential defined as

$$\Phi_{\text{eff}} = \Phi(R,z) + \frac{{L_z}^2}{2R^2}; \tag{2.4}$$

[1] A notable, although simplified, exception could be found in an integrable rotating Stačkel model (see Contopoulos and Vandervoort, 1992, and references therein).

[2] The study of such orbits in axisymmetric galaxies can be reduced to a two-dimensional problem by exploiting the conservation of the z-component of angular momentum of any star.

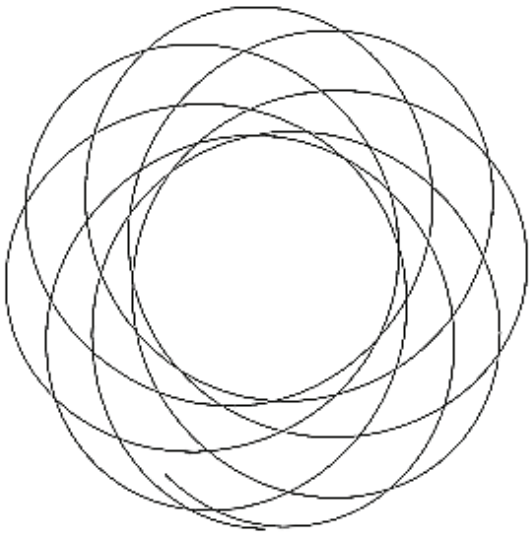

Figure 2.1: A general orbit in a spherical or axisymmetric potential forms a rosette figure.

where L_z is the only non-zero component of the angular momentum in the system.

The three-dimensional motion of a star in an axisymmetric potential $\Phi(R, z)$ can be reduced to the two-dimensional case on the (R, z) plane (called meridional plane) with the Hamiltonian

$$H_{\text{eff}} = \frac{1}{2}({p_R}^2 + {p_z}^2) + \Phi_{\text{eff}}(R, z), \tag{2.5}$$

where p_R and p_z are, respectively, the momenta on the radial and on the vertical directions.

If $R_g(L_z)$ is the guiding-centre radius for an orbit of angular momentum L_z, defined as the radius for which

$$\left(\frac{\partial \Phi}{\partial R}\right)_{(R_g,0)} = \frac{{L_z}^2}{{R_g}^3} = R_g \dot{\varphi}^2, \tag{2.6}$$

that is the condition for a circular orbit with angular speed $\dot{\varphi}$, a new variable can be introduced as the difference between the radial position of the star and its point of equilibrium:

$$x \equiv R - R_g. \tag{2.7}$$

Thus $(x, z) = (0, 0)$ are the coordinates in the meridional plane of the minimum for the potential of Equation 2.4 and, as a consequence, Φ_{eff} can be expanded in a Taylor series about this point:

$$\Phi_{\text{eff}} = \Phi_{\text{eff}}(R_g, 0) + \frac{1}{2}\left(\frac{\partial^2 \Phi_{\text{eff}}}{\partial R^2}\right)_{(R_g,0)} x^2 + \frac{1}{2}\left(\frac{\partial^2 \Phi_{\text{eff}}}{\partial z^2}\right)_{(R_g,0)} z^2 + O(xz^2). \tag{2.8}$$

In this expression the first derivatives are null because the point is a minimum of the potential, whereas the term proportional to xz goes to zero because the potential Φ_{eff} is assumed to be symmetric near $z = 0$.

The general equations of motion then become very simple if it is applied the epicycle approximation, i.e. an hypothesis that allows to neglect all terms of order xz^2 or higher in the expansion 2.8.

By defining the quantities

$$\kappa^2(R_g) \equiv \left(\frac{\partial^2 \Phi_{\text{eff}}}{\partial R^2}\right)_{(R_g,0)} \quad \text{and} \quad \nu^2(\mathrm{R_g}) \equiv \left(\frac{\partial^2 \Phi_{\text{eff}}}{\partial \mathrm{z}^2}\right)_{(\mathrm{R_g},0)}, \tag{2.9}$$

the equations of the motion are

$$\ddot{R} = -\frac{\partial \Phi_{\text{eff}}}{\partial R} \Rightarrow \ddot{x} = -\kappa^2 x \quad \text{and} \quad \ddot{\mathrm{z}} = -\frac{\partial \Phi_{\text{eff}}}{\partial \mathrm{z}} \Rightarrow \ddot{\mathrm{z}} = -\nu^2 \mathrm{z}. \tag{2.10}$$

x and z have, respectively, the shape of two harmonic oscillators with frequencies κ and ν. The frequency κ is called *epicycle* or *radial frequency*, while ν is the *vertical frequency*.

From Equation 2.4 it follows that

$$\left(\frac{\partial^2 \Phi_{\text{eff}}}{\partial R^2}\right) = \left(\frac{\partial^2 \Phi}{\partial R^2}\right) - \frac{3{L_z}^2}{R^4}$$

and

$$\left(\frac{\partial^2 \Phi_{\text{eff}}}{\partial z^2}\right) = \left(\frac{\partial^2 \Phi}{\partial z^2}\right),$$

as the derivative with respect to z of L_z is zero. In conclusion, the Equations 2.9 become

$$\kappa^2(R_g) = \left(\frac{\partial^2 \Phi}{\partial R^2}\right)_{(R_g,0)} + \frac{3{L_z}^2}{R^4} = \left(\frac{\partial^2 \Phi}{\partial R^2}\right)_{(R_g,0)} + \frac{3}{R_g}\left(\frac{\partial \Phi}{\partial R}\right)_{(R_g,0)}, \tag{2.11}$$

$$\nu^2(R_g) \equiv \left(\frac{\partial^2 \Phi}{\partial z^2}\right)_{(R_g,0)}. \tag{2.12}$$

Since the circular frequency is given by

$$\Omega^2(R) = \frac{1}{R}\left(\frac{\partial \Phi}{\partial R}\right)_{(R,0)} = \frac{{L_z}^2}{R^4} \tag{2.13}$$

and so

$$\left(\frac{\mathrm{d}\Omega^2}{\mathrm{dR}}\right)_{(R_g,0)} = -\frac{\Omega^2}{R} + \frac{1}{R}\left(\frac{\partial^2 \Phi}{\partial R^2}\right)_{(R_g,0)}, \tag{2.14}$$

the epicycle frequency assumes the short form of

$$\kappa^2(R_g) = \left(R\frac{\mathrm{d}\Omega^2}{\mathrm{dR}} + 4\Omega^2 \right)_{R_g}. \tag{2.15}$$

It is interesting to discuss a consequence of the just derived approximation.

When a star is orbiting in the equatorial plane of an axisymmetric galaxy, the orbital radius R is a periodic function of time and the period of its radial oscillations T_R is defined by

$$T_R = 2\int_{R_1}^{R_2} \frac{\mathrm{dR}}{\sqrt{2[E-\Phi(r)] - L^2/R^2}}, \tag{2.16}$$

where R_1 and R_2 are, respectively, the pericentre and the apocentre of the orbit, E is the energy per unit mass of the object that performs the orbit (i.e. the star), L is the module of the angular momentum per unit mass (which is constant because the motion is bound in a plane) and $\Phi(R)$ is the axisymmetric gravitational potential. T_R is the time required for the star to travel back and forth from apocentre to pericentre during its revolution.

In travelling from pericentre to apocentre and back, the azimuthal angle φ increase by an amount

$$\Delta\varphi = 2L\int_{R_1}^{R_2} \frac{\mathrm{dR}}{R^2\sqrt{2[E-\Phi(R)] - L^2/R^2}} \tag{2.17}$$

and the related oscillation frequencies are then

$$\omega_R = \frac{2\pi}{T_R} \quad \text{and} \quad \omega_\mathrm{a} = \frac{\Delta\varphi}{\mathrm{T_R}}, \tag{2.18}$$

because $\Delta\varphi$ is the displacement of the star during a whole radial oscillation.

The quantity $\Delta\varphi/2\pi$ is, generally, an irrational number and, for this reason, the orbit does not return to its starting point even after an infinite number of revolutions, drawing a rosette figure similar to the one shown in Figure 2.1.

If the frame is rotating with angular speed Ω_p, the azimuthal angle increases in one radial period by $\Delta\varphi_p$, i.e.

$$\Delta\varphi_p = \Delta\varphi - \Omega_p T_R. \tag{2.19}$$

At this point, it is clear that there are some values of Ω_p for which the orbit is closed. If $\Delta\varphi_p = 2\pi n/m$, with n and m integers, the orbit closes exactly after m radial oscillations each n revolution. Thus

$$\Omega_p = \frac{1}{T_R}[\Delta\varphi - \Delta\varphi_p] = \frac{\Delta\varphi}{T_R} - \frac{\Delta\varphi_p}{T_R} = \omega_a - \frac{n}{m}\frac{2\pi}{T_R} = \omega_a - \frac{n}{m}\omega_R. \tag{2.20}$$

In the result of the last equation ω_R and ω_a can be approximated by their values for nearly circular orbits. Therefore the azimuthal frequency becomes the

circular frequency Ω, while the radial frequency becomes the epicycle frequency κ, yielding

$$\Omega_p \simeq \Omega - \frac{n\kappa}{m}. \tag{2.21}$$

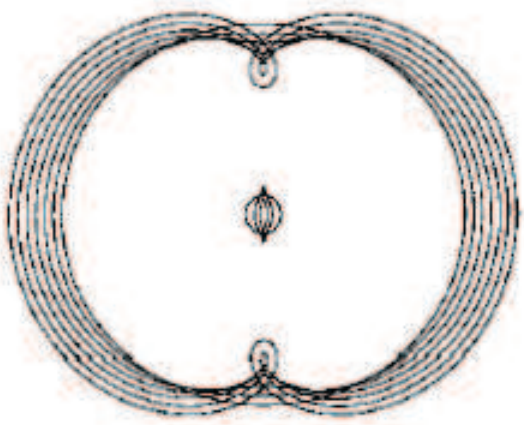

Figure 2.2: In a frame which rotates with angular speed $\Omega_p = \Omega - n\kappa/m$, the elliptical orbits assume the forms displayed (Sellwood and Wilkinson, 1993, see). The couple (n, m) represented are $(1, \pm 2)$.

In Figure 2.2 are presented some orbits for two different values of the couple (n, m): it is clear that, in the case $(n, m) = (1, 2)$ (dotted line), the star executes exactly two radial excursions while drifting forward with respect to the global pattern during one complete revolution around the center.

Stellar orbits obeying to Equation 2.21 would describe a two-fold non-axisymmetry following a bar-like structure, which rotates rigidly with the pattern speed Ω_p. The typical values assumed by this precession frequency along the galactic radius are provided in Figure 2.3 for our Galaxy.

If a potential has a particular shape in order to produce a plateau in the precession frequency curve for a significant radial range, then the stars which populate the nested orbits would precede together conserving their mutual position for each following revolution. According to the distribution of these orbits, the result can be the formation of a bar-like wave pattern, especially when the gravitational attraction starts to add other stars to the initial structure.

2.3 Bars as small perturbations in a rotating potential

Here I derive the equations of motion for a weak bar in the linear theory. In the study of a galactic disc, the frame of reference (x, y, z) is the one in which the potential Φ is static, i.e. a frame that rotates steadily at angular velocity $\boldsymbol{\Omega}_p = \Omega \hat{\boldsymbol{e}}_z$.

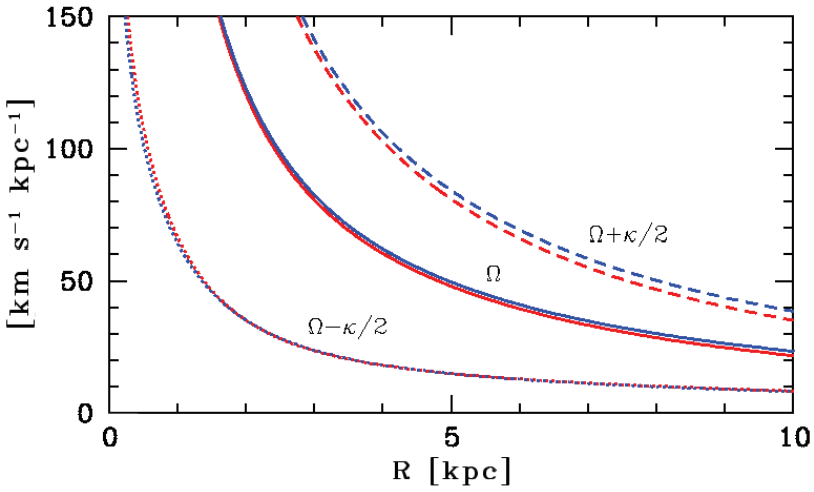

Figure 2.3: Curves $\Omega - \kappa/2$, Ω, and $\Omega + \kappa/2$, computed through a numerically modelled potential of the Milky-Way galaxy. The different colours refer to two slightly different sets of parameters (see Widrow and Dubinski, 2005).

A general loop orbit[3] can be represented as a superposition of the circular motion of a guiding center and small oscillations around it. For this reason the description of orbits in weak non-axisymmetric potentials is closely related to the epicycle theory of nearly circular orbits in an axisymmetric potential described above.

Considering the general three-dimensional case, if the velocity in the corotating frame is $\dot{\boldsymbol{x}}$, the corresponding velocity in an inertial frame is $\dot{\boldsymbol{x}} + \boldsymbol{\Omega}_p \times \boldsymbol{x}$. Therefore the Lagrangian is

$$\mathcal{L} = \frac{1}{2} \left| \dot{\boldsymbol{x}} + \boldsymbol{\Omega}_p \times \boldsymbol{x} \right|^2 - \Phi(\boldsymbol{x}). \tag{2.22}$$

As a consequence, the momentum $\boldsymbol{p}$ is

$$\boldsymbol{p} = \frac{\partial \mathcal{L}}{\partial \dot{\boldsymbol{x}}} = \dot{\boldsymbol{x}} + \boldsymbol{\Omega}_p \times \boldsymbol{x} \Rightarrow \dot{\boldsymbol{x}} = \boldsymbol{p} - \boldsymbol{\Omega}_p \times \boldsymbol{x}. \tag{2.23}$$

The associated Hamiltonian can be calculated through the Legendre transformation

$$\begin{aligned} H_J &= \boldsymbol{p} \cdot \dot{\boldsymbol{x}} - \mathcal{L} \\ &= \boldsymbol{p} \cdot [\boldsymbol{p} - \boldsymbol{\Omega}_p \times \boldsymbol{x}] - \frac{1}{2} p^2 + \Phi(\boldsymbol{x}) \\ &= p^2 - \boldsymbol{p} \cdot (\boldsymbol{\Omega}_p \times \boldsymbol{x}) - \frac{1}{2} p^2 + \Phi(\boldsymbol{x}) \\ &= \frac{1}{2} p^2 + \Phi(\boldsymbol{x}) - \boldsymbol{\Omega} \cdot (\boldsymbol{x} \times \boldsymbol{p}). \end{aligned} \tag{2.24}$$

[3] A loop orbit is the orbit of a star which circulates in a fixed sense about the center of the potential, while oscillating in radius.

Equation 2.24 requires a vectorial identity[4]. H_J is the Hamiltonian that governs the motion in the corotating frame, while $H = \frac{1}{2}p^2 + \Phi$, $\boldsymbol{L} = \boldsymbol{x} \times \boldsymbol{p}$ and $\boldsymbol{p}$ itself refer to the motion in a inertial frame. Consequently, it can be written

$$H_J = H - \boldsymbol{\Omega}_p \cdot \boldsymbol{L}. \tag{2.25}$$

Since $\Phi(\boldsymbol{x})$ is constant in the rotating frame, H_J does not depend on time explicitly, so $\frac{\mathrm{dH_J}}{\mathrm{dt}} = \frac{\partial H_J}{\partial t}$ vanishes[5]. As a result, H_J is an integral of motion and, although in a rotating non-axisymmetric potential neither H or $\boldsymbol{L}$ is conserved, this is the case for the combination $H - \boldsymbol{\Omega}_p \cdot \boldsymbol{L}$. From 2.24 it follows that the constant value of H_J could be written as

$$\begin{aligned} E_J &= \frac{1}{2}|\dot{\boldsymbol{x}}|^2 + \Phi - \frac{1}{2}|\boldsymbol{\Omega}_p \times \boldsymbol{x}|^2 \\ &= \frac{1}{2}|\dot{\boldsymbol{x}}|^2 + \Phi_{\mathrm{eff}}, \end{aligned} \tag{2.26}$$

where the effective potential has been defined as

$$\begin{aligned} \Phi_{\mathrm{eff}}(\boldsymbol{x}) &\equiv \Phi(\boldsymbol{x}) - \frac{1}{2}\left|\boldsymbol{\Omega}_p \times \boldsymbol{x}\right|^2 \\ &= \Phi(\boldsymbol{x}) - \frac{1}{2}[|\boldsymbol{\Omega}_p \times \boldsymbol{x}| \cdot |\boldsymbol{\Omega}_p \times \boldsymbol{x}|] \\ &= \Phi(\boldsymbol{x}) - \frac{1}{2}[|\boldsymbol{\Omega}_p \cdot \boldsymbol{\Omega}_p||\boldsymbol{x} \cdot \boldsymbol{x}| - |\boldsymbol{\Omega}_p \cdot \boldsymbol{x}||\boldsymbol{x} \cdot \boldsymbol{\Omega}_p|] \\ &= \Phi(\boldsymbol{x}) - \frac{1}{2}[|\boldsymbol{\Omega}_p|^2|\boldsymbol{x}|^2 - (\boldsymbol{\Omega}_p \cdot \boldsymbol{x})^2] \end{aligned} \tag{2.27}$$

through another vectorial identity[6]. Equation 2.27 shows without equivocation that the effective potential is composed by the sum of the gravitational potential and the repulsive centrifugal potential.

Since

$$\boldsymbol{\nabla}_{\boldsymbol{x}}[\boldsymbol{a} \cdot (\boldsymbol{x} \times \boldsymbol{b})] = \boldsymbol{\nabla}_{\boldsymbol{x}}[\boldsymbol{x} \cdot (\boldsymbol{b} \times \boldsymbol{a})] = \boldsymbol{b} \times \boldsymbol{a},$$

for $\boldsymbol{a}$ and $\boldsymbol{b}$ three-dimensional vectors, applying Hamilton's equation to Equation 2.24, the two quantities $\dot{\boldsymbol{p}}$ and $\dot{\boldsymbol{x}}$ can be calculated in the corotating frame:

$$\begin{aligned} \dot{\boldsymbol{p}} &= -\frac{\partial H_J}{\partial \boldsymbol{x}} = -\boldsymbol{\nabla}\Phi + \boldsymbol{p} \times \boldsymbol{\Omega}_p = -\boldsymbol{\nabla}\Phi - \boldsymbol{\Omega}_p \times \boldsymbol{p}, \\ \dot{\boldsymbol{x}} &= \frac{\partial H_J}{\partial \boldsymbol{p}} = \boldsymbol{p} - \frac{\partial}{\partial \boldsymbol{p}}[\boldsymbol{p} \cdot (\boldsymbol{\Omega}_p \times \boldsymbol{x})] = \boldsymbol{p} - \boldsymbol{\Omega}_p \times \boldsymbol{x}, \end{aligned} \tag{2.28}$$

where it can be recognized the same result of Equation 2.23.

Eliminating p between the two expressions in 2.28 and considering that Ω_p does not vary with time, it follows that

[4] $\boldsymbol{A} \cdot (\boldsymbol{B} \times \boldsymbol{C}) = \boldsymbol{C} \cdot (\boldsymbol{A} \times \boldsymbol{B}) = \boldsymbol{B} \cdot (\boldsymbol{C} \times \boldsymbol{A})$, with A, B and C arbitrary vectors.

[5] This comes directly from $\frac{\mathrm{dH}}{\mathrm{dt}} = \frac{\partial H}{\partial \boldsymbol{x}}\dot{\boldsymbol{x}} + \frac{\partial H}{\partial \boldsymbol{p}}\dot{\boldsymbol{p}} + \frac{\partial H}{\partial t} = \frac{\partial H}{\partial t}$.

[6] $(\boldsymbol{A} \times \boldsymbol{B}) \cdot (\boldsymbol{C} \times \boldsymbol{D}) = (\boldsymbol{A} \cdot \boldsymbol{C})(\boldsymbol{B} \cdot \boldsymbol{D}) - (\boldsymbol{A} \cdot \boldsymbol{D})(\boldsymbol{B} \cdot \boldsymbol{C})$, with A, B, C and D arbitrary vectors.

$$\begin{aligned}\ddot{\boldsymbol{x}} &= \dot{\boldsymbol{p}} - \frac{\partial}{\partial t}(\boldsymbol{\Omega}_p \times \boldsymbol{x}) \\ &= -\boldsymbol{\nabla}\boldsymbol{\Phi} - \boldsymbol{\Omega}_p \times \boldsymbol{p} - \boldsymbol{\Omega}_p \times \dot{\boldsymbol{x}} \\ &= -\boldsymbol{\nabla}\Phi - \boldsymbol{\Omega}_p \times (\dot{\boldsymbol{x}} + \boldsymbol{\Omega}_p \times \boldsymbol{x}) - \boldsymbol{\Omega}_p \times \dot{\boldsymbol{x}} \\ &= -\boldsymbol{\nabla}\Phi - 2\boldsymbol{\Omega}_p \times \dot{\boldsymbol{x}} - \boldsymbol{\Omega}_p \times (\boldsymbol{\Omega}_p \times \boldsymbol{x}) \\ &= -\boldsymbol{\nabla}\Phi - 2\boldsymbol{\Omega}_p \times \dot{\boldsymbol{x}} - (\boldsymbol{\Omega}_p \cdot \boldsymbol{x})\boldsymbol{\Omega}_p + (\boldsymbol{\Omega}_p \cdot \boldsymbol{\Omega}_p)\boldsymbol{x} \\ &= -\boldsymbol{\nabla}\Phi - 2\boldsymbol{\Omega}_p \times \dot{\boldsymbol{x}} + |\boldsymbol{\Omega}_p|^2 x - \boldsymbol{\Omega}_p(\boldsymbol{\Omega}_p \cdot \boldsymbol{x});\end{aligned} \tag{2.29}$$

in the last calculation it was used the relation

$$\boldsymbol{A} \times (\boldsymbol{B} \times \boldsymbol{C}) = (\boldsymbol{A} \cdot \boldsymbol{C})\boldsymbol{B} - (\boldsymbol{A} \cdot \boldsymbol{B})\boldsymbol{C}.$$

In Equation 2.29 the term $-2\boldsymbol{\Omega}_p \times \dot{\boldsymbol{x}}$ is the Coriolis force and $-\boldsymbol{\Omega}_p \times (\boldsymbol{\Omega}_p \times \boldsymbol{x})$ is the centrifugal force.

The gradient of the last line of Equation 2.27 is

$$\boldsymbol{\nabla}\Phi_{\text{eff}} = \boldsymbol{\nabla}\Phi - |\boldsymbol{\Omega}_p|^2 \boldsymbol{x} + \boldsymbol{\Omega}_p(\boldsymbol{\Omega}_p \cdot \boldsymbol{x}), \tag{2.30}$$

and Equation 2.29 could be rewritten as

$$\ddot{\boldsymbol{x}} = -\boldsymbol{\nabla}\Phi_{\text{eff}} - 2\boldsymbol{\Omega}_p \times \dot{\boldsymbol{x}}. \tag{2.31}$$

However, to describe the perturbation, it is useful considering a set of polar coordinates in the corotating frame as (R, φ), arranging the line $\varphi = 0$ to denote the long axis of the potential.

The Lagrangian is given by Equation 2.22. Hence, it is necessary to perform a coordinates transformation $(x_1, x_2, x_3) \to (R, \varphi)$:

$$\begin{aligned}\hat{\boldsymbol{e}}_R &= \cos\varphi \hat{\boldsymbol{x}}_1 + \sin\varphi \hat{\boldsymbol{x}}_2 + 0\,\hat{\boldsymbol{x}}_3, \\ \hat{\boldsymbol{e}}_\varphi &= -\sin\varphi \hat{\boldsymbol{x}}_1 + \cos\varphi \hat{\boldsymbol{x}}_2 + 0\,\hat{\boldsymbol{x}}_3,\end{aligned} \tag{2.32}$$

consequently,

$$\begin{aligned}\boldsymbol{x} &= R\cos\varphi \hat{\boldsymbol{x}}_1 + R\sin\varphi \hat{\boldsymbol{x}}_2 + 0\,\hat{\boldsymbol{x}}_3 \\ &= R\hat{\boldsymbol{e}}_R,\end{aligned} \tag{2.33}$$

Wilkinson

$$\begin{aligned}\dot{\boldsymbol{x}} &= (\dot{R}\cos\varphi - R\dot{\varphi}\sin\varphi)\hat{\boldsymbol{x}}_1 + (\dot{R}\sin\varphi + R\dot{\varphi}\cos\varphi)\hat{\boldsymbol{x}}_2 + 0\,\hat{\boldsymbol{x}}_3 \\ &= \dot{R}(\cos\varphi + \sin\varphi) + R\dot{\varphi}(\cos\varphi - \sin\varphi) \\ &= \dot{R}\hat{\boldsymbol{e}}_R + R\dot{\varphi}\hat{\boldsymbol{e}}_\varphi,\end{aligned} \tag{2.34}$$

considering that $\boldsymbol{\Omega}_p$ has only a non-zero component on the z-axis,

$$\boldsymbol{\Omega}_p = 0\,\hat{\boldsymbol{x}}_1 + 0\,\hat{\boldsymbol{x}}_2 + \Omega_p \hat{\boldsymbol{x}}_3, \tag{2.35}$$

thus

$$\boldsymbol{\Omega}_p \times \boldsymbol{x} = (-\Omega_p R\sin\varphi)\hat{\boldsymbol{x}}_1 + (\Omega_p R\cos\varphi)\hat{\boldsymbol{x}}_2 + 0\,\hat{\boldsymbol{x}}_3$$

$$\begin{aligned} &= \Omega_p R(\cos\varphi - \sin\varphi) \\ &= \Omega_p R\hat{\boldsymbol{e}}_\varphi. \end{aligned} \tag{2.36}$$

As a result,

$$\begin{aligned} \frac{1}{2}|\dot{\boldsymbol{x}} + \boldsymbol{\Omega}_p \times \boldsymbol{x}|^2 &= \frac{1}{2}|\dot{R}\hat{\boldsymbol{e}}_R + R\dot{\varphi}\hat{\boldsymbol{e}}_\varphi + \Omega_p R\hat{\boldsymbol{e}}_\varphi|^2 \\ &= \frac{1}{2}[\dot{R}^2 + R^2(\dot{\varphi} + \Omega_p)^2], \end{aligned} \tag{2.37}$$

and the Lagrangian $\mathcal{L}$ becomes

$$\mathcal{L} = \frac{1}{2}\dot{R}^2 + \frac{1}{2}[R(\dot{\varphi} + \Omega_p)]^2 - \Phi(R, \varphi). \tag{2.38}$$

Similarly, the equations of motion in a rotating two-dimensional potential is given by 2.29. Then, the same coordinates change leads to[7]

$$\begin{aligned} \ddot{\boldsymbol{x}} &= (\ddot{R}\cos\varphi - \dot{R}\dot{\varphi}\sin\varphi - \dot{R}\dot{\varphi}\sin\varphi - R\ddot{\varphi}\sin\varphi - R\dot{\varphi}^2\cos\varphi)\hat{\boldsymbol{x}}_1 + \\ &+ (\ddot{R}\sin\varphi + \dot{R}\dot{\varphi}\cos\varphi + \dot{R}\dot{\varphi}\cos\varphi + R\ddot{\varphi}\cos\varphi - R\dot{\varphi}^2\sin\varphi)\hat{\boldsymbol{x}}_2 + \\ &+ 0\,\hat{\boldsymbol{x}}_3 \\ &= (\ddot{R} - R\dot{\varphi}^2)(\sin\varphi + \cos\varphi) + (2\dot{R}\dot{\varphi} + R\ddot{\varphi})(\cos\varphi - \sin\varphi) \\ &= (\ddot{R} - R\dot{\varphi}^2)\hat{\boldsymbol{e}}_R + (2\dot{R}\dot{\varphi} + R\ddot{\varphi})\hat{\boldsymbol{e}}_\varphi, \end{aligned} \tag{2.39}$$

$$\begin{aligned} \boldsymbol{\Omega}_p \times \dot{\boldsymbol{x}} &= [0 - \Omega_p(\dot{R}\sin\varphi + R\dot{\varphi}\cos\varphi)]\hat{\boldsymbol{x}}_1 + [\Omega_p(\dot{R}\cos\varphi - R\dot{\varphi}\sin\varphi) - 0]\hat{\boldsymbol{x}}_2 + 0\,\hat{\boldsymbol{x}}_3 \\ &= \Omega_p\dot{R}(\cos\varphi - \sin\varphi) - \Omega_p R\dot{\varphi}(\cos\varphi + \sin\varphi) \\ &= \Omega_p\dot{R}\hat{\boldsymbol{e}}_\varphi - \Omega_p R\dot{\varphi}\hat{\boldsymbol{e}}_R. \end{aligned} \tag{2.40}$$

In this way, Equation 2.31 becomes

$$(\ddot{R} - R\dot{\varphi}^2)\hat{\boldsymbol{e}}_R + (2\dot{R}\dot{\varphi} + R\ddot{\varphi})\hat{\boldsymbol{e}}_\varphi = 2\Omega_p R\dot{\varphi}\hat{\boldsymbol{e}}_R - 2\Omega_p\dot{R}\hat{\boldsymbol{e}}_\varphi - \boldsymbol{\nabla}\Phi_{\text{eff}}, \tag{2.41}$$

but Φ_{eff} is defined in the first line of Equation 2.27 and, since Equation 2.36 is valid,

$$|\boldsymbol{\Omega}_p \times \boldsymbol{x}|^2 = {\Omega_p}^2 R^2, \tag{2.42}$$

thus

$$\begin{aligned} &(\ddot{R} - R\dot{\varphi}^2)\hat{\boldsymbol{e}}_R + (2\dot{R}\dot{\varphi} + R\ddot{\varphi})\hat{\boldsymbol{e}}_\varphi \\ &= 2\Omega_p R\dot{\varphi}\hat{\boldsymbol{e}}_R - 2\Omega_p\dot{R}\hat{\boldsymbol{e}}_\varphi - \boldsymbol{\nabla}\Phi + \tfrac{1}{2}\boldsymbol{\nabla}({\Omega_p}^2 R^2). \end{aligned} \tag{2.43}$$

To derive the equations of motion in the polar frame, every component must be considered separately. Hence, with regard to the $\hat{\boldsymbol{e}}_R$ component, it follows that

$$\ddot{R} - R\dot{\varphi}^2 = 2\Omega_p R\dot{\varphi} - \tfrac{\partial\Phi}{\partial R} + \tfrac{1}{2}\tfrac{\partial}{\partial R}({\Omega_p}^2 R^2) = 2\Omega_p R\dot{\varphi} + {\Omega_p}^2 R - \tfrac{\partial\Phi}{\partial R}$$

[7] The coordinates transformation for $\dot{\boldsymbol{x}}$ has been already performed in Equation 2.34.

$$\Rightarrow \ddot{R} = R(\dot{\varphi}^2 + 2\Omega_p\dot{\varphi} + {\Omega_p}^2) - \frac{\partial\Phi}{\partial R}, \tag{2.44}$$

and for the $\hat{e}_\varphi$ component the equation is

$$\begin{aligned} 2\dot{R}\dot{\varphi} + R\ddot{\varphi} &= -2\Omega_p\dot{R} - \tfrac{1}{R}\tfrac{\partial\Phi}{\partial\varphi} + \tfrac{1}{2R}\tfrac{\partial}{\partial\varphi}({\Omega_p}^2R^2) \\ 2R\dot{R}(\dot{\varphi} + \Omega_p) + R^2\ddot{\varphi} &= -\tfrac{\partial\Phi}{\partial\varphi}, \end{aligned} \tag{2.45}$$

in obtaining both Equations 2.44 and 2.45 it was used the gradient in polar coordinates[8].

Finally, the equations of motion in a two-dimensional rotating potential, described using a set of polar coordinates, are

$$\ddot{R} = R(\dot{\varphi} + \Omega_p)^2 - \frac{\partial\Phi}{\partial R} \tag{2.46}$$

and

$$\frac{\mathrm{d}}{\mathrm{dt}}[R^2(\dot{\varphi} + \Omega_p)] = -\frac{\partial\Phi}{\partial\varphi}. \tag{2.47}$$

Assuming the bar as a weak perturbation, the potential $\Phi(R,\varphi)$ can be expanded as the sum of a principal component depending only on the radius, and a perturbing non-axisymmetric part

$$\Phi(R,\varphi) = \Phi_0(R) + \Phi_1(R,\varphi), \tag{2.48}$$

with $|\Phi_1/\Phi_0| \ll 1$. Hence, also R and φ could be expanded in zeroth and first order

$$R(t) = R_0 + R_1(t) \quad ; \quad \varphi(t) = \varphi_0(t) + \varphi_1(t), \tag{2.49}$$

with the assumption that the term R_0 is constant with time[9]. Substituting these expressions into Equations 2.46 and 2.47, it yields

$$\begin{aligned} \ddot{R}_1 = {} & (R_0 + R_1)(\dot{\varphi}_0 + \dot{\varphi}_1 + \Omega_p)^2 \\ & - \left(\frac{\partial\Phi_0}{\partial R}\right)_{R_0} - \left(\frac{\partial^2\Phi_0}{\partial R^2}\right)_{R_0} R_1 - \left(\frac{\partial\Phi_1}{\partial R}\right)_{R_0} - \left(\frac{\partial^2\Phi_1}{\partial R^2}\right)_{R_0} R_1, \end{aligned} \tag{2.50}$$

and to

$$\frac{\mathrm{d}}{\mathrm{dt}}[(R_0 + R_1)^2(\dot{\varphi}_0 + \dot{\varphi}_1 + \Omega_p)] = -\left(\frac{\partial\Phi_1}{\partial\varphi}\right)_{\varphi_0(R_0)} - \left(\frac{\partial^2\Phi_1}{\partial\varphi^2}\right)_{\varphi_0(R_0)} \varphi_1, \tag{2.51}$$

remembering that Φ_0 does not depend on the coordinate φ and that the expansion is about the radius R_0.

If the sum of the zeroth-order terms is set to zero, it follows that

$$R_0(\dot{\varphi}_0 + \Omega_p)^2 = \left(\frac{\partial\Phi_0}{\partial R}\right)_{R_0}, \tag{2.52}$$

[8]The gradient in polar coordinates is given by $\boldsymbol{\nabla} f(R,\varphi) = \frac{\partial f}{\partial R}\hat{\boldsymbol{e}}_R + \frac{1}{R}\frac{\partial f}{\partial\varphi}\hat{\boldsymbol{e}}_\varphi$.

[9]In a almost circular orbits, the star oscillates about a fixed radius.

and to

$$\frac{\mathrm{d}}{\mathrm{dt}}[R_0^2\dot{\varphi}_0 + \Omega_p] = 0 \quad \Rightarrow \quad \dot{\varphi}_0 = const. \tag{2.53}$$

The last is the equation for the centrifugal equilibrium at R_0. Henceforth it could be used the definition

$$\Omega_0 \equiv \Omega(R_0), \tag{2.54}$$

to rewrite the angular speed equation of the guiding center (R_0, φ_0), where

$$\Omega(R) \equiv \pm\sqrt{\frac{1}{R}\frac{\partial\Phi_0}{\partial R}} \tag{2.55}$$

is the circular frequency at R in the potential Φ_0, identical to Equation 2.13. Indeed, Equation 2.52 becomes

$$\begin{aligned}(\dot{\varphi}_0 + \Omega_p) = \sqrt{\tfrac{1}{R_0}\left(\tfrac{\partial\Phi_0}{\partial R}\right)_{R_0}} = \Omega(R_0) \equiv \Omega_0 \\ \Rightarrow \quad \dot{\varphi}_0 = \Omega_0 - \Omega_p,\end{aligned} \tag{2.56}$$

where, if $\Omega > 0$ the orbits are prograde and retrograde for $\Omega < 0$.

Setting the initial condition such that

$$\varphi_0(t) = (\Omega_0 - \Omega_p)t, \tag{2.57}$$

conserving only the first-order terms and remembering the constraints 2.52 and 2.53, the Equations 2.50 and 2.51 become respectively

$$\begin{aligned}\ddot{R}_1 &\simeq (R_0 + R_1)(\Omega_0 + \dot{\varphi}_1)^2 - \left(\frac{\partial^2\Phi_0}{\partial R^2}\right)_{R_0} R_1 - \left(\frac{\partial\Phi_1}{\partial r}\right)_{R_0} \\ &\simeq (R_0 + R_1)({\Omega_0}^2 + 2\Omega_0\dot{\varphi}_1 + \dot{\varphi}_1^2) - \left(\frac{\partial^2\Phi_0}{\partial R^2}\right)_{R_0} R_1 - \left(\frac{\partial\Phi_1}{\partial r}\right)_{R_0} \\ &\simeq R_1{\Omega_0}^2 + 2R_0\Omega_0\dot{\varphi}_1 - \left(\frac{\partial^2\Phi_0}{\partial R^2}\right)_{R_0} R_1 - \left(\frac{\partial\Phi_1}{\partial r}\right)_{R_0},\end{aligned}$$

$$\begin{aligned}\ddot{R}_1 + \left(\frac{\partial^2\Phi_0}{\partial R^2}\right)_{R_0} R_1 - R_1\Omega^2(R_0) - 2R_0\Omega_0\dot{\varphi}_1 &= -\left(\frac{\partial\Phi_1}{\partial R}\right)_{R_0} \\ \Rightarrow \ddot{R}_1 + \left(\frac{\partial^2\Phi_0}{\partial R^2} - \Omega^2\right)_{R_0} R_1 - 2R_0\Omega_0\dot{\varphi}_1 &= -\left(\frac{\partial\Phi_1}{\partial R}\right)_{R_0},\end{aligned} \tag{2.58}$$

and

$$\begin{aligned}\frac{\mathrm{d}}{\mathrm{dt}}[(R_0 + R_1)^2(\Omega_0 + \dot{\varphi}_1)] &\simeq -\left(\frac{\partial\Phi_1}{\partial\varphi}\right)_{\varphi_0(R_0)} \\ \frac{\mathrm{d}}{\mathrm{dt}}[({R_0}^2 + 2R_0R_1 + {R_1}^2)(\Omega_0 + \dot{\varphi}_1)] &\simeq -\left(\frac{\partial\Phi_1}{\partial\varphi}\right)_{\varphi_0(R_0)} \\ \frac{\mathrm{d}}{\mathrm{dt}}[{R_0}^2\dot{\varphi}_1 + 2\Omega_0R_0R_1] &\simeq -\left(\frac{\partial\Phi_1}{\partial\varphi}\right)_{\varphi_0(R_0)},\end{aligned}$$

reminding that R_0 and Ω_0 do not change with time,

$$\begin{aligned} {R_0}^2\ddot{\varphi}_1 + 2\Omega_0 R_0 \dot{R}_1 &= -\left(\frac{\partial\Phi_1}{\partial\varphi}\right)_{\varphi_0(R_0)} \\ \Rightarrow \quad \ddot{\varphi}_1 + 2\Omega_0\frac{\dot{R}_1}{R_0} &= -\frac{1}{{R_0}^2}\left(\frac{\partial\Phi_1}{\partial\varphi}\right)_{\varphi_0(R_0)}. \end{aligned} \tag{2.59}$$

Let the perturbative, non-axisymmetric potential Φ_1 has the analytical form

$$\Phi_1(R,\varphi) = \Phi_p(R)\cos(m\varphi), \tag{2.60}$$

with m, positive integer. This expression is very general since any potential that is an even function of φ can be expanded as a sum of terms of this form[10]. In particular if $m = 2$, the same potential acts in the same way every half revolution and it can be interpreted as a bar-like potential.

Operating the further approximation[11] $\varphi_1 \ll 1$, then $(\Omega_0 - \Omega_p)t \sim \varphi(t)$. This hypothesis permits to substitute φ with φ_0 in Equations 2.58 and 2.59:

$$\ddot{R}_1 + \left(\frac{\partial^2\Phi_0}{\partial R^2} - \Omega^2\right)_{R_0} R_1 - 2R_0\Omega_0\dot{\varphi}_1 = -\left(\frac{\partial\Phi_p}{\partial R}\right)_{R_0}\cos[m(\Omega_0 - \Omega_p)t] \tag{2.61}$$

and

$$\ddot{\varphi}_1 + 2\Omega_0\frac{\dot{R}_1}{R_0} = \frac{\Phi_p(R_0)}{{R_0}^2} m\sin[m(\Omega_0 - \Omega_p)t]. \tag{2.62}$$

Integrating Equation 2.62, it yields

$$\begin{aligned} \int \frac{\mathrm{d}\dot{\varphi}_1}{\mathrm{dt}}\,\mathrm{dt} &= -2\frac{\Omega_0}{\mathrm{R_0}}\int \frac{\mathrm{dR_1}}{\mathrm{dt}}\,\mathrm{dt} + \frac{\mathrm{m}\Phi_\mathrm{p}(\mathrm{R_0})}{{\mathrm{R_0}}^2}\int \sin[\mathrm{m}(\Omega_0 - \Omega_\mathrm{p})\mathrm{t}]\,\mathrm{dt} \\ \Rightarrow \quad \dot{\varphi}_1 &= -2\Omega_0\frac{R_1}{R_0} - \frac{\Phi_p(R_0)}{{R_0}^2(\Omega_0 - \Omega_p)}\cos[m(\Omega_0 - \Omega_p)t] + const. \end{aligned} \tag{2.63}$$

Thanks to this last result, $\dot{\varphi}_1$ can be eliminated in 2.61,

$$\begin{aligned} \ddot{R}_1 + \left(\frac{\partial^2\Phi_0}{\partial R^2} - \Omega^2\right)_{R_0} R_1 + 4R_1{\Omega_0}^2 + 2\frac{\Omega_0}{R_0}\frac{\Phi_p(R_0)}{(\Omega_0 - \Omega_p)}\cos[m(\Omega_0 - \Omega_p)t] + const \\ = -\left(\frac{\partial\Phi_p}{\partial R}\right)_{R_0}\cos[m(\Omega_0 - \Omega_p)t] \\ \Rightarrow \quad \ddot{R}_1 + \left(\frac{\partial^2\Phi_0}{\partial R^2} + 3\Omega^2\right)_{R_0} R_1 + const \\ = -2\frac{\Omega_0\Phi_p(R_0)}{R_0(\Omega_0 - \Omega_p)}\cos[m(\Omega_0 - \Omega_p)t] - \left(\frac{\partial\Phi_p}{\partial R}\right)_{R_0}\cos[m(\Omega_0 - \Omega_p)t]. \end{aligned} \tag{2.64}$$

[10] Any more complicated potential can be thought as superposition of these potential with different Ω_p.

[11] This means that the bar potential does not deviate too much from the main potential. So far the assumption was that only the angular velocity $\dot{\varphi}_1$ was small, not that φ_1 was itself small. However, allowing for large excursions in φ_1 is important in considering the resonances.

According to 2.15, the second term of the the first member of Equation 2.65 can be interpreted as the epicycle frequency of the star with radius R_0. From Equation 2.55

$$\frac{\partial}{\partial R}\left(\frac{\partial \Phi_0}{\partial R}\right) = \frac{\partial}{\partial R}(R\Omega^2) = \Omega^2 + R\frac{\mathrm{d}\Omega^2}{\mathrm{dR}}, \tag{2.65}$$

and therefore

$$\left(\frac{\partial^2 \Phi_0}{\partial R^2} + 3\Omega^2\right)_{R_0} = \left(R\frac{\mathrm{d}\Omega^2}{\mathrm{dR}} + 4\Omega^2\right)_{R_0} \equiv {\kappa_0}^2. \tag{2.66}$$

At this point Equation 2.65 becomes

$$\ddot{R}_1 = -{\kappa_0}^2 R_1 - \left[\frac{\mathrm{d}\Phi_\mathrm{p}}{\mathrm{dR}} + \frac{2\Omega\Phi_p}{R(\Omega - \Omega_p)}\right]_{R_0} \cos[m(\Omega_0 - \Omega_p)t] + const. \tag{2.67}$$

This is the equation of motion of a harmonic oscillator of natural frequency κ_0 that is driven at frequency $m(\Omega_0 - \Omega_p)$. The $const$ could be not considered because it represents only a shift from R_1 to $R_1 + const$.

The solution of Equation 2.67 is then easily found because the harmonic oscillator is a standard dynamical system:

$$R_1(t) = K_1 \cos(\kappa_0 t + \zeta) - \left[\frac{\mathrm{d}\Phi_\mathrm{p}}{\mathrm{dR}} + \frac{2\Omega\Phi_p}{R(\Omega - \Omega_p)}\right]_{R_0} \frac{\cos[m(\Omega_0 - \Omega_p)t]}{\Delta}, \tag{2.68}$$

where K_1 and ζ are arbitrary constants, and

$$\Delta \equiv {\kappa_0}^2 - m^2(\Omega_0 - \Omega_p)^2. \tag{2.69}$$

Since Equation 2.57 is valid, $t = \frac{\varphi_0}{\Omega_0 - \Omega_p}$, so

$$R_1(\varphi_0) = K_1 \cos\left(\frac{\kappa_0 \varphi_0}{\Omega_0 - \Omega_p} + \zeta\right) + K_2 \cos(m\varphi_0), \tag{2.70}$$

where

$$K_2 \equiv -\frac{1}{\Delta}\left[\frac{\mathrm{d}\Phi_\mathrm{p}}{\mathrm{dR}} + \frac{2\Omega\Phi_p}{R(\Omega - \Omega_p)}\right]_{R_0}. \tag{2.71}$$

$K_1 = 0$ implies that $R_1(\varphi_0)$ is a periodical function of φ_0 with period $2\pi/m$. Hence the related orbit is a closed loop orbit. The orbits with $K_1 \neq 0$ are the non-closed orbits parented by the one with $K_1 = 0$.

2.4 Resonances

The natural resonant frequencies of the stellar orbits represent an important topic which is meaningful also to understand strong barred systems. In general, if the gravitational field generated by a bar-like structure perturbs a stellar orbit near one of its resonant frequencies, then the response of the orbit will be way larger than the perturbing force.

In detail, the closest loop orbit can be studied by setting $K_1 = 0$ in the Equation 2.70:

$$R_1(\varphi_0) = K_2 \cos(m\varphi_0) = -\left[\frac{\mathrm{d}\Phi_\mathrm{p}}{\mathrm{dR}} + \frac{2\Omega\Phi_p}{R(\Omega-\Omega_p)}\right]_{R_0} \frac{cos[m(\Omega_0-\Omega_p)t]}{{\kappa_0}^2 - m^2(\Omega_0-\Omega_p)^2}, \tag{2.72}$$

and it is clear that it has singularities for some values of R_0. These are:

- *Corotation resonance* (CR).
  If
  $$\Omega_0 = \Omega_p, \tag{2.73}$$
  $\dot{\varphi_0} = 0$ and the guiding centre rotates at the same angular speed of the potential. In a barred galaxy this corresponds to the radius where the orbiting stars in the disc have the same angular velocity of the pattern. CR is the most important resonance in the galaxy, because the mean position of the star with respect to the global pattern never changes as long as Ω_p is fixed.

- *Inner Lindblad*[12] *resonance* (ILR).
  If
  $$\Omega_p - \Omega_0 = +\frac{\kappa_0}{m}, \tag{2.74}$$
  the star overtakes the potential and encounters its crests at the resonant frequency κ_0. Since the star has always the same phase in its radial oscillation, when it has the same position with respect to the global pattern, it interacts more strongly with the pattern near ILR than it does at other radii in the disc.

- *Outer Lindblad resonance* (OLR).
  If
  $$\Omega_p - \Omega_0 = -\frac{\kappa_0}{m}, \tag{2.75}$$
  the peaks of the potential evolve faster with respect to the star which does two radial oscillations for every revolution backward around the centre.

A circular orbit has two natural frequencies: (i) if the star is displaced radially, it oscillates at the epicycle frequency κ_0; differently, (ii) if the stars is displaced azimuthally, in such a way that it is still on a circular orbit (neglecting the radial shift), then it will continue on a circular orbit displaced from the original one. It follows that the star is naturally stable to this kind of displacements, i.e. its natural azimuthal frequency is zero (the star does not oscillate azimuthally). These resonances arise when the forcing frequency which drives the star, $m(\Omega_0 - \Omega_p)$, becomes equal to one of the natural frequencies $\pm\kappa$ or 0.

Choosing $m = 2$ for a bar-like non-axisymmetry in Equation 2.70, it leads to

$$R_1(\varphi_0) = K_1 \cos\left(\frac{\kappa_0\varphi_0}{\Omega_0-\Omega_p} + \zeta\right) + K_2\cos(2\varphi_0). \tag{2.76}$$

[12]The resonances are named after the Swedish galactic astronomer Bertil Lindblad.

R_1 is the radius of the small oscillation about the mean radius R_0; it can be inferred that the close loop orbit of a star is aligned with the bar pattern if $K_2 > 0$, while it is perpendicularly arranged when $K_2 < 0$. When R_0 crosses a resonance the sign of K_2 changes, therefore also the orientation of the close loop orbit changes.

If $K_1 = 0$, Equation 2.76 describes nearly circular orbits in a weakly barred potential.

When R_0 approaches the radius of either a Lindblad resonance or the CR, weak perturbation can produce a strong response, hence the value of R_1 becomes too large and the approximation of small perturbation is no longer valid. However, it is possible to modify the treatment to study the resonances (Goldreich and Tremaine, 1981).

Given the destructive effect of the resonances on the orbit families that are aligned with the bar structure (named x_1), their radii seem to represent a critical spatial limit for the extension of bars structure in disc galaxies (see, e.g., Contopoulos, 1980; Elmegreen and Elmegreen, 1990). In particular, orbital analysis (Contopoulos and Papayannopoulos, 1980; Athanassoula et al., 1983; Contopoulos and Grosbol, 1989) of simple galactic models shows that, approaching the ILR toward the galactic centre, the favoured orbits become counter-aligned with respect to the bar (named x_2), undermining its structural integrity (e.g. Norman and Hasan, 1990). For these reasons, to a first approximation, the ILR and the CR respectively correlate to the inner and outer ends of the bar overdensity, as they are inferred from observations.

Chapter 3

Bar formation and evolution

After an overall discussion about the currently adopted methods to numerically investigate barred systems (§ 3.1), and an introduction to some instruments I employ in this work to analyse the simulatios (§ 3.2), I describe the fundaments of the complex processes of bar formation (§ 3.3) and evolution (§ 3.4).

3.1 N-body simulations

As discussed in chapter 2, the complexity of barred systems cannot be addressed through analytical strategies.

Notwithstanding the coarse set-ups of the first times,[1] the advent of N-body simulations immediately appeared to be essential in order to tackle this problem (see, e.g. Miller, Prendergast, and Quirk, 1970; Hohl, 1971; Ostriker and Peebles, 1973; Sellwood, 1980; Sellwood, 1981; Athanassoula and Sellwood, 1986; Combes et al., 1990; Pfenniger and Friedli, 1991). Nowadays, the evolution of softwares and the development of modern calculators have promoted a rapid progress in investigating complex dynamical topics, such as the formation and the evolution of galactic bars, and the trend continues uninterrupted.

N-body simulations[2] could be mainly classified into *isolated* (or *dynamical*) runs, and *cosmological* runs. The former ignore the formation process of the galaxy, since all the components are already in place and in equilibrium. These kind of simulations allow to reach higher spatial and mass resolution, since they reduce the problem to the minimum amount of particles to adequately describe the analysed system. The computational burden is then significantly diminished in a non-cosmological case and the same dynamical problem can be approached

[1] The first numerical simulations had obvious limitations due to the emerging technology, such as the crude resolution or the two-dimensional geometry.

[2] The rationale of N-body simulations is the representation of a dynamical system through an ensemble of interacting mass elements. The total gravitational force is then calculated either directly, or through some approximation, in order to reduce the huge computational load.

multiple times with relatively small computer resources. For instance, isolated runs allow to study in detail the influence of a single parameter (e.g. the halo mass, the system triaxiality, the velocity distribution, etc), by producing suites of simulations of the same system, each with a different implementation of the investigated property in a idealized model.

On the other hand, cosmological simulations describe a system of cosmological size, starting from the primordial DM fluctuations whose collapse results in the formation of the structures. These runs have the great quality of providing realistic boundary conditions for the analysed galaxies, and the properties of the objects are, at any time, physically motivated according to the set of cosmological parameters used. Unfortunately, the necessity to simulate a far larger volume for a sufficient amount of time, while retaining the needed minimum resolution to investigate the particular dynamical problem, represents an enormous obstacle to the use of these techniques.

Cosmological *zoom-in* runs can mitigate this problem by selecting a region of interest, such as a DM halo, and simulating it to a high precision, whereas the neighbourhood of that region is left at a coarser resolution. The low resolution neighbourhood provides a realistic tidal field for the highly resolved region of interest. Thanks to this expedient, a single halo can be studied in great detail analogously to isolated runs, and sub-grid recipes can be more localized and physically motivated.
Although, zoom-in cosmological simulations are not without any opposition[3], they are the best and most efficient numerical models to study individual galaxies and halos (see, e.g., Romano-Díaz et al., 2008; Guedes et al., 2011; Scannapieco and Athanassoula, 2012; Kraljic, Bournaud, and Martig, 2012).

Hydrodynamical zoom-in simulations, where the baryonic components (gas and stars) are evolved along with the DM, are the cornerstones of my work and are detailed in chapter 4. The numerical applications employed, GASOLINE (Stadel, 2001; Wadsley, Stadel, and Quinn, 2004) and CHANGA (Menon et al., 2015; Jetley et al., 2008; Jetley et al., 2010), solve the Euler equations via a Smoothed Particle Hydrodynamics (SPH) approach, where the fluids are represented by means of a mesh-free particle distribution and their properties are evaluated in each point by averaging the properties of a number of nearby particles (see § 4.1.2, for the description of the SPH techniques implemented in GASOLINE and CHANGA).

Simulating barred galaxies in a fully cosmological context has started only recently, following the first zoom-in simulations that produced realistic late-type galaxies. Indeed, both the combination of high resolution and effective stellar-feedback prescriptions are required in order to prevent the accumulation of central low angular momentum gas, allowing for the build-up of cold discs with flat rotation curves, comparable with observations (Navarro and Benz, 1991).

The majority of these recent works merely acknowledges the presence of a stellar bar within the galactic disc, since such structure does not represent the

[3]For instance, some criticisms are made about the number and distribution of galactic satellites, the inner halo radial density profile, or on the formation of bulge-less galaxies (e.g. Silk and Mamon, 2012, and references therein).

main subject of their analysis (see, e.g. Robertson et al., 2004; Scannapieco et al., 2009; Feldmann et al., 2010; Brooks et al., 2011; Bonoli et al., 2016; Sokołowska et al., 2017). However, there are also some studies specifically aimed to the analysis of the evolving non-axisymmetry (e.g. Romano-Díaz et al., 2008; Kraljic, Bournaud, and Martig, 2012; Scannapieco and Athanassoula, 2012; Goz et al., 2015; Okamoto, Isoe, and Habe, 2015; Spinoso et al., 2017; Zana et al., 2018c; Zana et al., 2018a). Mass and spatial resolution significantly improved over the years and this allowed to follow the investigated bar properties in ever greater detail. An alternative approach has been offered by Algorry et al. (2017) and Peschken and Łokas (2018), who perform statistical studies taking advantage of the large-volume cosmological simulations EAGLE (Crain et al., 2015; Schaye et al., 2015) and Illustris (Vogelsberger et al., 2014), respectively. Nonetheless, the large sample of galaxies in these simulations has been achieved by implementing lower mass and time resolution, consequently hindering the study on sub-galactic scales.

A special mention has to be reserved for Governato et al. (2007), with a view to chapter 7, where the authors implement different sub-grid prescriptions to simulate three galaxy-sized haloes in hydro-cosmological runs with remarkable resolution – a gravitational softening ranging from 0.3 to 1 kpc – but still not optimal in order to properly characterise the evolving features of a sub-galactic structure. Even though the focus of their work was essentially the study of the formed galactic systems, the authors were the first to point out a direct effect of the supernova (SN) feedback over the development of a stellar bar, finding that the main effect of SN energy injection was to make the disc more stable against bar formation, by contributing to the formation of a lighter stellar disc which builds up more slowly over time.

The Eris-suite simulations (see § 4.2) provide an advantageous laboratory to investigate this kind of systems in reasonable detail.

3.2 Bar analysis

Before discussing the birth and evolution of bars, it is convenient to define some of the essential tools used in the next chapters to study the simulated systems. Bar intensity and extent are estimated through a Fourier decomposition of the stellar surface density when the host galaxy is projected face-on.

3.2.1 Bar strength

In the following work, the measure of the bar intensity is given by the ratio between the second term of the expansion, which captures the strength of two-fold structure, and the zeroth (axisymmetric) term through the relation

$$A_2(R) \equiv \frac{\left|\sum_j m_j e^{2i\theta_j}\right|}{\sum_j m_j}, \tag{3.1}$$

where m_j is the mass of the j-th particle and θ_j the azimuthal angle of its projection over the disc plane. The summation can be carried either over all

particles enclosed within a cylinder of radius R, coaxial with the galaxy, and of fixed height (see, e.g., Spinoso et al., 2017), or just over the particles within a single shell around the cylindrical radius R (after the division of the disc into annuli of equal width; see, e.g., Athanassoula and Misiriotis 2002; Valenzuela and Klypin 2003). I indicate the first, "cumulative" case with the nomenclature $A_2(<R)$, whereas $A_2(R)$ refers to the second "differential" case.

Both the approaches can provide an effective way to determine the strength of a non-axisymmetry, albeit with some differences. $A_2(<R)$ is usually evaluated over a higher number of particles, thus, the signal-to-noise ratio is higher and the profile is smoother with respect to its differential counterpart. The particular shape of its profile, which increases as far as the stellar distribution is decisively non-axisymmetric, decreasing gradually farther out, allows also to obtain an estimate for the bar length (see § 3.2.2). Unfortunately, $A_2(<R)$ depends on the galactic CMC and can assumes different values depending, e.g., on the growing rate of the central stellar system. Figures 5.2 and 7.4 provide two excellent examples of how well the quantities $A_2(<R)$ and $A_2(R)$ trace the presence of a bar-like overdensity in disc galaxies. As long as the bar grows, a more evident peak in the $A_2(<R)$ profile is visible (the galaxies in Figures 5.2 and 7.4 are evolving from left to right). At a sightly smaller radius, an analogous feature is present in $A_2(R)$ thus, when the contribute of the $m = 2$ mode starts decreasing with respect to the $m = 0$ mode, a fading non-axisymmetric structure can be identified.

Both the estimates are useful in order to select the correct overdensities (for instance, in the first panel of Figure 5.2, the $A_2(R)$ profile shows some crests for $R > 4$ kpc which do not belong to the bar; see also the method adopted in § 7.2 to find the correct bar structures). For these reasons, the maxima of the two profiles $A_2(R)$ and $A_2(<R)$, $A_{2,\max}R$ and $A_{2,\max}(<R)$ are estimates for the strength of the bar, at any point of its evolution. However, since the value of $A_{2,\max}(<R)$ relies on the assembled central stellar mass within the radius R, making it less precise than its differential counterpart, in the following chapters $A_{2,\max}(R)$ is used as the main estimator to characterize the bars.

3.2.2 Bar length

A very important part in the study of galactic bars is the evaluation of their length. This is a very debated subject, since the body of the bar has no perfectly defined boundaries. Moreover, it is extremely difficult to match numerical results with observations, especially because many approaches used to evaluate such property cannot be adopted in both these two fields of study (for further details, see e.g. Debattista and Sellwood, 2000; Athanassoula and Misiriotis, 2002).

In the present works, I utilize a method to measure the bar length described in Athanassoula and Misiriotis (2002).

A by-product of the Fourier decomposition is represented by the phase of the $A_2(R)$ component, defined as:

$$\Phi(R) \equiv \frac{1}{2} \arctan \left[\frac{\sum_j m_j \sin(2\theta_j)}{\sum_j m_j \cos(2\theta_j)} \right], \tag{3.2}$$

where the summation is performed along each annulus of radius R, as before. Since this phase is nearly constant in the range of the bar overdensity[4] and is randomly oriented outside, the length of the bar can be defined as the radius R_Φ of the outmost annulus with phase constant and equal to the phase of the bar $\Phi_{\rm bar}$. After this point, the phase $\Phi(R)$ starts varying with the radius (this is effectively exemplified by the middle row of Figure 7.4 on page 91). Practically, this is managed by means of a tolerance parameter $\Delta\phi$, within which the variation of $\Phi(R)$ is considered negligible.

When a galaxy evolves in isolation, the major contribution to the phase of the second Fourier component in the disc density is the bar itself, and beyond its range the phase is usually averaged out. However, in the cosmological simulations described in chapter 4, the initial disc instabilities, the formation of a sporadic spiral arms, and the passage of some perturbers across the disc plane have, occasionally, the effect of significantly altering the total phase of the disc. In order to account for these issues, and guide the analysis to the correct result, I do not compare $\Phi(R)$ with the phase of the whole disc (as performed in Athanassoula and Misiriotis, 2002), but I substitute the total disc phase with the phase $\Phi(R_{\rm max})$ as benchmark-phase, where $R_{\rm max}$ is the radius where $A_{2,\rm max}(<R)$ occurs (see § 3.2.1).

Although, in the following works, I use R_Φ as the main bar length estimator, $R_{\rm max}$ traces remarkably well the total extent of the stellar bar (see, for instance, Figure 5.4). As a matter of fact, every annulus whose phase is coherent with $\Phi_{\rm bar}$ contributes to the increase of the cumulative function $A_2(<R)$. This results in the monotonic growth of $A_2(<R)$, which starts near the centre of the galaxy and ends as soon as this contribution is averaged out in the outer part of the disc and is no longer important (as it is exemplified in Figure 5.2).

The connection between R_Φ and $R_{\rm max}$ is further investigated in § 5.1.1.2, through a Monte Carlo method. The results demonstrate how both the methods agree in the evaluation of the size of a non-axisymmetric overdensity.

3.3 Bar formation

If a galactic potential produces a particular shape in the rotational velocity curve, such that the precession frequency $\Omega - \kappa/2$ does not vary appreciably over a certain radial range, there the elongated orbits, in which a star would execute two radial excursions for every revolution around the centre, would be almost closed in a frame rotating with a certain angular speed $\Omega_{\rm bar}$, and it would be possible for the galaxy to support a nested set of these orbits with the same phase, as long as the potential is not significantly perturbed. This is a necessary condition for a potential to grow a bar. If the potential is bar-unstable,

[4]The possible fluctuations may depend on the mass resolution of the numerical simulation.

an initial instability may trigger a self-sustaining gravitational process which adds more and more stars to the growing bar.

However, other methods are commonly used to describe how a galaxy would respond to a triggering fluctuation. Two parameters are considered (see, e.g. Ostriker and Peebles, 1973; Combes and Sanders, 1981; Sellwood, 1981) for stellar discs, the Q parameter (Toomre, 1964), defined as

$$Q(R) \equiv \frac{\sigma_{\rm R}(R)\kappa(R)}{3.36G\Sigma_\star(R)}, \tag{3.3}$$

where $\sigma_{\rm R}$ is the radial velocity dispersion and κ the epicycle frequency defined in Equation 2.15, and the swing amplification parameter for an $m = 2$ perturbation X (Goldreich and Tremaine, 1978; Goldreich and Tremaine, 1979), defined as

$$X(R) \equiv \frac{k_{\rm crit}(R)R}{2} = \frac{\kappa^2(R)R}{4\pi G\Sigma_\star(R)}, \tag{3.4}$$

where $\lambda_{\rm crit}$ is the longest unstable wavelength (Binney and Tremaine, 2008) and is defined by

$$\lambda_{\rm crit} = 2\pi/k_{\rm crit} = 4\pi^2 G\Sigma_\star\kappa^{-2}. \tag{3.5}$$

Although a precise threshold to discriminate between stable and unstable systems is not available[5], it can be said that larger values of these parameters imply that the disc is more stable against local (Q) and global (X) instabilities. The perturbations are immediately dumped when the random motion of stars is high enough. Indeed, Athanassoula and Sellwood (1986) showed that an embryonic bar in a dynamically hot disc (i.e. with high σ_R, hence with large Q) can have an insignificant growth rate. Differently, the swing amplification parameter gives an estimate of the disc self-gravity, which is necessary in order to drive a bar instability (Efstathiou, Lake, and Negroponte, 1982; Christodoulou, Shlosman, and Tohline, 1995; Sellwood, 2013).
Unfortunately, the growth of the initial instability is a very complex topic and the link between the parameters Q and X and some of the resulting bar properties, like the strength or the length, is not a linear relation. Indeed, the parameters are only valid in the tight-winding approximation (that is when the perturbation has a radial wavelength much shorter than the galactic radius; see WKB approximation in Binney and Tremaine 2008) and do not consider in the computation every dynamical property of the disc, such as the vertical velocity dispersion (Klypin et al., 2009), or the mass resolution (see Sellwood, 2013);

Another criterion introduced to measure sensitivity of discs to the growth of non-axisymmetries is the parameter

$$\epsilon_{\rm ELN} = \frac{V_{\rm max}R_{\rm d}}{GM_{\rm d}}, \tag{3.6}$$

proposed by Efstathiou, Lake, and Negroponte (1982), where $V_{\rm max}$ is the peak in rotation curve and R_d and $M_{\rm d}$ are the disc scale radius and the disc total

[5] Various threshold have been proposed in different numerical studies (e.g. Toomre, 1964; Toomre, 1981; Goldreich and Tremaine, 1978; Goldreich and Tremaine, 1979; Bauer and Widrow, 2018).

mass, respectively. According to Efstathiou, Lake, and Negroponte (1982), the disc is prone to instability when $\epsilon_{\rm ELN} \lesssim 1$ (Efstathiou, Lake, and Negroponte, 1982; Mayer and Wadsley, 2004; Governato et al., 2007). The criterion represents another way to evaluate the self gravity of the system related to the stellar components, but also to the DM halo through $V_{\rm max}$. The criticisms of $\epsilon_{\rm ELN}$ are similar to those expressed for the Q and X parameters. In particular, Athanassoula (2008b) shows that, the velocity dispersion of the disc appears to as important as the $\epsilon_{\rm ELN}$ parameter, regarding the bar formation process. In Appendix C, I provide the time evolution of Equation 3.6 for the simulations ErisBH and Eris2k. The results do not disagree with the previous study of the parameters Q and X (see § 7.4), however they do not help in determining the formation time of the related structures.

All the described criteria asses the ability of a particular galactic potential to enhance an original fluctuation. However, there is not a full agreement on the source of that seeding instability, starting the feedback loop, and several processes have been proposed in order to explain its nature.
In general, the trigger could be found either in the small perturbations (some simulations of isolated galaxies blame the shot noise; see, e.g., Efstathiou, Lake, and Negroponte 1982) which naturally arises within the host galaxy (e.g. Hohl, 1971; Ostriker and Peebles, 1973; Sellwood, 2014), or outside the system, in the tidal interactions with external perturbers, such as galaxies in mergers and close flybys[6] encounters (Byrd et al., 1986; Mayer and Wadsley, 2004; Curir, Mazzei, and Murante, 2006; Gauthier, Dubinski, and Widrow, 2006; Romano-Díaz et al., 2008; Martinez-Valpuesta, Aguerri, and González-García, 2016; Peschken and Łokas, 2018, e.g.) and galaxy clusters (Byrd and Valtonen, 1990; Łokas et al., 2016).

Nonetheless, recent observational investigations reached contrasting results regarding the role of environment in the bar formation process. Some studies indeed found an excess of barred systems in dense galactic environments (Skibba et al., 2012, e.g.), whereas other works support the idea that dynamical perturbations have the primary effect of suppressing the formation of a bar (Li et al., 2009; Lin et al., 2014).

The dichotomy has been also investigated through numerical simulations, since they have become the primary tools to model these particular dynamical problems: in a simulation the whole three-dimensional distribution of matter is completely characterized at any needed time and it is, in principle, possible to study the effect of every single interaction on every galaxy undergoing bar instability (e.g. Moetazedian et al., 2017; Pettitt and Wadsley, 2018). However, only recently (see § 3.1) the approach has been successfully extended to the cosmological context, thanks to the modern technologies and computational strategies.[7] When studying the effect of a gravitational interaction on a target

[6] A gravitational interaction between two galactic objects is defined as a flyby when, differently from what happens in a merger, the interacting systems are still separated after the encounter.
[7] When the previous studies were not focussed on the formation of grand design spirals arms, they were about idealized system already built in equilibrium (e.g. Gerin, Combes, and Athanassoula, 1990), or even limited to the two-dimensional case (see, for instance, Noguchi, 1987).

galaxy, it is not trivial to produce suitable initial conditions or physically-motivated orbital parameters for the companion objects, and this represents one of the key factors in favour of the cosmological approach.

Unfortunately, the number of works that focus on the study of bars in a fully cosmological perspective, including the growth of the host galaxy through a sequence of mergers as well as accretion of diffuse gas, is still limited, as they require high spatial resolution < 100 pc, in order to properly resolve the stellar dynamics (within the bar region) while evolving a large cosmological box (e.g. Romano-Díaz et al., 2008; Kraljic, Bournaud, and Martig, 2012; Scannapieco and Athanassoula, 2012; Kraljic, Bournaud, and Martig, 2012; Goz et al., 2015; Okamoto, Isoe, and Habe, 2015; Spinoso et al., 2017; Algorry et al., 2017; Sokołowska et al., 2017).

In chapter 5, I take advantage of one of these state-of-the-art cosmological simulations, the ErisBH simulation (Bonoli et al., 2016) in order to constrain the actual effect of various types of tidal interactions on the bar formation process. Then, in chapter 7, I will discuss how this process is affected by the stellar feedback in another modern cosmological run, the Eris2k simulation (Sokołowska et al., 2017).

Although the encounters taking place in a cosmological simulation are more realistic with respect to the isolated runs, it is immensely difficult to modify the orbital parameters of the undergoing flybys in order to explore, for instance, a particular region of the parameter space. This partially explains the small number of high resolved cosmological simulation adopted to investigate such a complex phenomenon, as the formation of a bar.

A different approach is provided by Peschken and Łokas (2018), on the barred galaxies of the Illustris-1 simulation (Vogelsberger et al., 2014). Given the numerous objects evolved in the simulated volume, the authors focus on the statistical importance of dynamical encounters. Obviously, the large sample of galaxies in the Illustris run is paid by with suboptimal mass and time resolution, which limits the validity of a study on sub-galactic scale structures (see § 6.1.1, for further details).

3.4 Bar evolution

Bars are transient objects: they form, evolve, dissolve and, possibly, form again (see, e.g., Friedli, 1999). The evolution of the two-fold non-axisymmetric structure can be (generally) outlined only in isolated galaxy, since in more populated environments external perturbers could play a dominant role on the bar life and death (see chapter 5 and 6).

3.4.1 Isolated galaxy

When a galaxy evolution is dominated by secular processes occurring within its boundaries, bars growth is mainly determined by angular momentum transfer. In particular, in a barred galaxy, the angular momentum is emitted from the inner parts of the disc towards the regions outside the CR. The process is

maximised in the neighbourhood of the resonances (mainly the ILR in the disc), because, in those regions, the bar potential perturbs the orbiting material in a coherent way during every consecutive revolution (see § 2.4). Analogously, in the outer disc, the resonant material represents the most efficient absorber too (the OLR is the main actor in this case, as well as all the other resonances outside the CR radius and the CR itself). A fundamental role is played by the DM halo, since it provides an immense reservoir of absorbing material. Athanassoula (2002) showed that one of the most limiting feature in isolated simulations is the absence of a live DM halo (i.e. an halo able to actively interact with the other simulation elements, differently from a mere analytic potential) since it cannot receive the angular momentum flowing from the inner galactic disc, thus artificially reducing the growth of the bar. Within the DM halo the absorption process again dominates at resonances, but the contribution per unit mass is smaller with respect to the disc material, due to its higher velocity dispersion. Indeed, the hotter is the absorbing or emitting material, the lesser is the transfer efficiency (see Lynden-Bell and Kalnajs, 1972; Tremaine and Weinberg, 1984).

As long as the angular momentum is removed from the bar and is brought to the outskirts of the galaxy, the bar keeps growing both in length and in strength. This is because the bar, being located within the CR, has a negative total angular momentum value and, thus, the further outflow of angular momentum enlarges the bar-unstable zone and increases the distance of the CR radius from the centre.[8]

In general, the angular momentum loss has a threefold effect on the evolution of a bar-like structure: a bar can (i) simply reduces its pattern frequency, or increases its extent and strength (ii) because some of its orbits become more elongated and move outward their apocentres, or (iii) because some nearly-circular orbits, that originally were not part of the bar, lose angular momentum and increase their eccentricity, thus being incorporated in the bar. In an isolated galaxy a combination of these effects takes place depending on the local properties of the disc and the DM halo (Athanassoula, 2003). As previously pointed out, since the velocity dispersion controls the efficiency of the momentum transfer and, in turn, this determines the evolution of the bar parameters (such as the length or the strength), it is evident that a higher velocity dispersion in the gaseous or stellar component results in a weaker bar which also grows slower.

3.4.1.1 Bar death: buckling instability

Before discussing the general effects that tidal interactions have on already formed bars (see § 3.4.2), it is important to examine the possible fate of a bar when it is exposed only to its self gravity and to the host potential.

Bars are not eternal. Many numerical simulations reveal that, if bars have enough time to evolve, at a certain point, either they lose their structural integrity or evolve to something more similar to a bulge. Then, it's not a question of if, it's a question of when.

[8]This, in turn, increases the region in which the bar can extend (see § 2.4 and Contopoulos

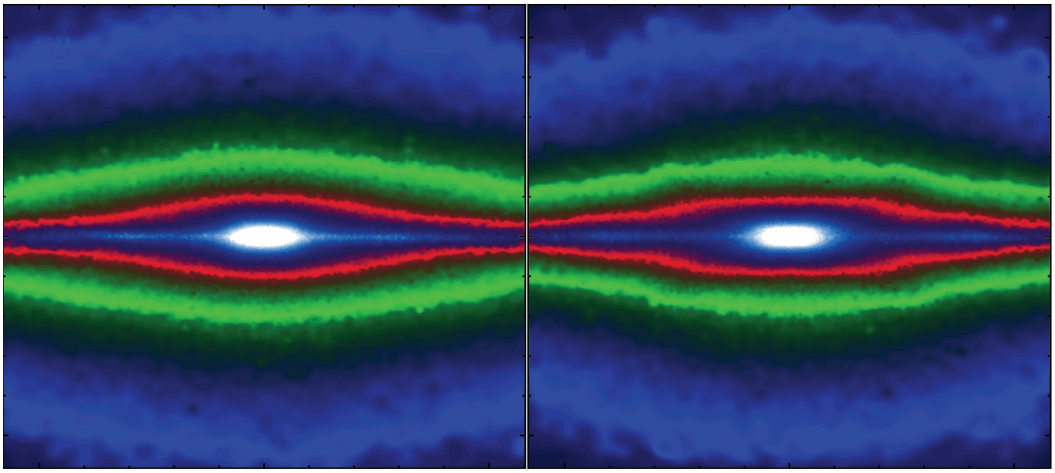

Figure 3.1: Stellar density maps of two very similar simulated barred galaxies seen side-on and pictured with high-contrast colour map. The right panel shows a more advanced stage in bar evolution, where vertical instabilities are leading to the formation of a peanut-shaped bulge. The feature is absent in the left panel.

After its formation, a bar starts evolving not only on the disc plane, but also on the normal axis, via vertical instabilities. Soon it dismisses its original density profile, inherited from the disc and buckles. The process, called *bucking instability*, is characterised by the quick development of a progressive asymmetry with respect to the galactic plane, which then results in the formation of a thicker structure whose edge-on projection resembles the shape of a box, a peanut, or a X (see, e.g. Combes et al., 1990; Raha et al., 1991).
Combes and Sanders (1981) were the first to point out that simulated bars seems peanut bulges when seen side-on and boxy bulges if observed end-on,[9] as it is clear from Figure 3.1. The X pattern is assumed to just traces the maxima of emission of the peanut-shaped bulge. Successively, a joint analysis of numerical simulations, photometrical and kinematical observations, has confirmed the strong connection between these particularly shaped bulges and bars (e.g. Kuijken and Merrifield, 1995; Lütticke, Dettmar, and Pohlen, 2000; Bureau and Athanassoula, 2005; Bureau et al., 2006). These qualitatively different profiles of edge-on disc galaxies arises from the same family of instabilities which force the stars to orbit outside the galactic plane (see, e.g., Patsis and Katsanikas, 2014). In particular, Patsis, Skokos, and Athanassoula (2003) show that, various members of the x_1 family (see chapter 2), once destabilized, emerge and bifurcate on the vertical axis. The boxy/peanut structure forms when stars populate the trapped orbits around those members.

A possible mechanism proposed as trigger for this orbital evolution is the "fire-hose" effect, that happens when the radial velocity dispersion becomes significantly larger than its vertical counterpart, compromising the stability of

1980).

[9] When an edge-on galaxy is observed with the line of sight aligned with the bar minor axis, it is called side-on, on the other hand, when the line of sight is perpendicular to the bar minor axis, it is called end-on.

the structure (Raha et al., 1991). This mechanism was originally applied by (Toomre, 1966) as a destabilizing process in a non-rotating, infinite sheet model, but was later put aside since axisymmetric galaxy was known to reach the threshold values of radial velocity dispersion. The situation is quite different for barred systems: the radial and vertical oscillations are generally decoupled, and the induced stream motions along the bar major axis make the horizontal motions assume higher values, the more evolved is the bar stage.

The asymmetric phase which leads to the formation of these structure is accompanied by a serious decrease in the bar strength (Combes et al., 1990; Raha et al., 1991; Debattista et al., 2004; Debattista et al., 2006; Martinez-Valpuesta and Shlosman, 2004; Martinez-Valpuesta, Shlosman, and Heller, 2006; Athanassoula, 2008a). It is quite controversial if this weakening produces an actual destruction of the bar. However, I will consider it a realistic outcome of the buckling process, given the strict requirements I use to define a strong bar (see, e.g., chapter 7).

In § 7.3, I outline three different methods to estimate the buckling process of the bar. They stem from either the analysis of the side-on projection of the stellar density or from the study of the velocity dispersion within the bar structure.

3.4.1.2 Bar death: bar suicide

Another possible demise for a stellar bar is reached simply when the conditions of the gravitational potential are no longer suitable to sustain a rigid pattern with a fixed precession frequency. As discussed in § 1.3, the gradual inflow of interstellar medium builds a CMC in the centre of the disc. This newly formed mass sensibly perturbs the central potential, scattering the stars whose orbits are aligned with the bar. As long as the CMC grows, the x_2 orbits cover an increasingly large phase-space volume at the expense of the x_1 orbits. Since the bar itself provides the means that drive the formation of the CMC, this process is commonly called *bar suicide*, and it is observed both in numerical simulations and in orbital analysis (e.g. Hasan and Norman, 1990; Friedli and Benz, 1993; Hasan, Pfenniger, and Norman, 1993; Combes, 1994; Norman, Sellwood, and Hasan, 1996; Berentzen et al., 1998). Also for the bar dissolution via CMC, the mass thresholds are widely debated. The reasons lies in the enormous type of galaxy profile available and in the complexity level required for the numerical simulations. Some works try to estimate a critical value for the CMC in percentage of the total disc mass (Norman, Sellwood, and Hasan 1996, $5-7$ percent; Berentzen et al. 1998 2 percent; Combes 2004, $1-5$ pecent) needed to destroy the bar.

According to (Shen and Sellwood, 2004), a bar can even tolerate a soft central mass of 10 percent, and it would be only weakened. In general, if a galaxy shows in its central part a concentrated bulge, or even a supermassive black hole (Hozumi and Hernquist, 1999), it is hard for the potential to sustain a system of stars, preceding coherently, as a rigid body for a sufficient amount of time (in order to make it grow). When these components form or grow in already barred systems, the hosted two-fold structures are profoundly perturbed and their stellar orbits are shuffled. Although it is not absolutely certain if the death of the bar is a necessary epilogue of the process, since this depends also on how

and how fast these components are assembled, the dissolution remains a highly probable scenario and I will present a relevant case in chapter 7.

Finally, it is important to remark that the gaseous inflows triggered by the bar torques are themselves a source of weakening for the bar intensity. The gas, coming from the outer part of the galaxy, transfers its angular momentum to the structure, which then reduces its length and strength (Bournaud and Combes, 2004). This zeroth-order effect can enhance the destructive influence of other mechanisms and contribute to the complete extinction of the bar overdensity.

3.4.2 Tidal interactions

Since galaxies are never completely isolated in the Universe, it is wise to ask what is the effect of the interaction with external objects on an already formed bar, in analogy to what has been considered in § 3.3.

In this case as well, only the analysis of a simulation allows to trace the motions of every galactic component during the entire evolution of the system. For this reason, numerical simulations are a necessary tool to connect observations to analytical works.

Some studies have been carried out in isolated runs with idealized boundary conditions and geometries (Gerin, Combes, and Athanassoula, 1990; Sundin and Sundelius, 1991; Sundin, Donner, and Sundelius, 1993) and, recently, even on a large sample of simulated galaxies, taking advantage of larger cosmological simulations (e.g. Peschken and Łokas, 2018).
In detail, Gerin, Combes, and Athanassoula (1990) described the change in bar strength and pattern speed of a strongly barred galaxy after a close encounter between a barred galaxy and a satellite in isolated three-dimensional models. They found that the interaction with a flyby induces a transient increase (decrease) of the bar strength and a corresponding decrease (increase) of the pattern speed, depending on the angle ψ, defined by

$$\psi \equiv \phi_{\rm bar} - \phi_{\rm sat}, \tag{3.7}$$

where $\phi_{\rm bar}$ is the phase of the bar and $\phi_{\rm sat}$ is the angle of the perturber at the moment of its pericentre, in the reference frame of the centre of mass of the main galaxy.[10] The following works by Sundin and Sundelius (1991) and Sundin, Donner, and Sundelius (1993), argued that the orbital angular momentum of the satellite is not the only variable to consider when studying the variation of the bar properties. The authors performed some numerical tests in a two-dimensional geometry and concluded that, despite the fact that the bar always varies its angular momentum in the encounter, it may either gain or lose mass depending on the position angle of the satellite pericentre. Thus, the cumulative effect on the bar angular speed is a combination of the transfer both of mass and angular momentum, which are triggered in different amounts depending on the orbital parameters of the encounter. All these works produced interesting results

[10] When ψ is positive (negative), the perturber is behind (ahead of) the bar; when $\psi = \pm 90°$, the effect of the satellite is null, due to symmetry reasons.

in the field of tidal interaction of barred system, however they are constrained by obsolete technology to very simple models with huge approximations.

Diversely, Peschken and Łokas (2018) analysed a sample of 121 massive galaxies in the Illustris-1 cosmological simulation (Vogelsberger et al., 2014), which underwent a close encounter during their evolutionary history and found a trace of that interaction in the evolution of the bar strength parameter. They suggested that the effect of the perturbation on the structure would depend both on the orbital angle (i.e. whether the approaching satellite is on a prograde or retrograde orbit) and on the strength of the perturbation, quantified through the Elmegreen parameter S (Elmegreen et al., 1991), i.e.

$$S = \frac{M_{\rm sat}}{M_{\rm gal}} \left(\frac{R_{\rm gal}}{R_{\rm peri}} \right)^3 \frac{\Delta T}{T}, \tag{3.8}$$

where $M_{\rm sat}$ and $M_{\rm gal}$ are the total masses of the perturber and of the main galaxy, respectively, whereas $R_{\rm peri}$ is the distance of the perturbing satellite at its pericentre and $R_{\rm gal}$ the barred galaxy size. The value of ΔT is given by the time taken by the satellite to travel one radian around the galaxy centre of mass near the pericentre. The rotation period in the outer part of the main galaxy T is, instead, defined by

$$T = \left(\frac{R_{\rm gal}^3}{G M_{\rm gal}} \right)^{1/2}, \tag{3.9}$$

On average, the overall effect of a weak tidal interaction in their sample is to reduce the strength of the bar, whereas more intense perturbations result in either an increase of the strength if the satellite orbit is prograde, or in a decrease, when the orbit is retrograde.

However, it is important to stress that works based on cosmological volumes are very valuable to study the demographics and general properties of barred galaxies, but the much higher resolution (of order 0.1 kpc), possible with cosmological zoom-in simulations of individual galaxies, is necessary to analyse in detail the internal dynamics of bars and their resulting evolution.

3.4.2.1 Bar death: apparent

From § 3.4.2 it is clear that a sufficiently strong perturbation can, in principle, lead a bar to its complete decay. A major merger would, most likely, be able to significantly change the potential well of the galaxy making it bar-stable (this kind of collisions significantly modifies the disc geometry, building an elliptical galaxy; see § 1.1). However, an event of such violence is not necessarily needed in order to shuffle the stellar orbits which make up the bars. A far minor merger, in fact, or even a close unequal-mass could be enough to destabilize the fragile equilibrium that holds the stars together. However, in this last case, the galactic potential would not be excessively perturbed and eventually the bar could reform with the same features it had before the encounter. For this reason I refer to this event as *apparent death*, to differentiate it from an actual bar destruction, when the gravitational potential is heavily affected (see § 3.4.1.1

and § 3.4.1.2). Since the defaillance of the bar strength parameter could last for a significant amount of time in the galaxy evolutionary history and low-mass flybs are common events even at low redshift, a galaxy with a strongly bar-unstable potential could be observed as an unbarred system with non-negligible probability. It is important to study if the number of theses objects is relevant and if the dependence from the environment has therefore to be consider when evaluating the bar fraction over a galaxy population.

In chapter 5 and 6, I discuss my contribution to the study of the effect of external interactions on to bars, by focussing on the impact of cosmologically motivated flybys on the central galaxy of the ErisBH and Eris2k zoom-in simulation volumes. In particular, I will describe an overall destructive effect for the tidal encounters on these strongly barred galaxies, including a case of bar apparent death.

Chapter 4

The simulations

The interplay among the fundamental physical processes cannot be reduced to simple analytical forms. We saw in § 3.1 that, for this reason, numerical methods have become ever more important in astrophysics and indispensable when investigating complex dynamical problems, such as bar formation and evolution.

In the following, I discuss the numerical set-ups of the cosmological simulations analysed in my works. In particular, after a brief introduction on the codes adopted in § 4.1, in § 4.2 I describe the two main simulations, ErisBH and Eris2k, sharing the same initial condition files, but implementing different prescriptions of sub-grid physics. In § 4.3, I characterize another suite of cosmological zoom-in simulations, produced using a snapshot of ErisBH as initial condition.

4.1 The codes

In this section, I outline the code ChaNGa (Menon et al., 2015), which I use to perform the simulations described in § 4.3 and its precursor gasoline (Wadsley, Stadel, and Quinn, 2004), adopted to evolve the runs in the Eris suite (see § 4.2).

ChaNGa (Charm N-body GrAvity solver) is a program for cosmological simulations derived from the tree-SPH code gasoline.

Both these codes compute gravitational forces through a hierarchical tree algorithm (Barnes and Hut, 1986), and hydrodynamical forces using SPH (Gingold and Monaghan, 1977; Lucy, 1977). The main difference between the two codes lies in the parallelization approach which, in the case of ChaNGa, is implemented via the high level parallel libraries Charm++, that allow to reach extraordinary scalability performances on various computer architectures.

4.1.1 Gravity

Gravity is the fundamental driving force in the majority of astrophysical systems.

In numerical simulations the mass density ρ is represented by means of a discrete distribution of matter. In order to solve Poisson's equation 2.2 for the gravitational potential Φ, it is usually computed the acceleration on a single body $\boldsymbol{a_i} = \nabla\Phi$ given by the cumulative attraction of all other bodies:

$$\boldsymbol{a}_i = G \sum_{i \neq j}^{N} \frac{m_j}{|\boldsymbol{r}_i - \boldsymbol{r}_j|^2} \tag{4.1}$$

where m_j and r_j are the mass and position of the j-th body, respectively, and N is the total number of particles in the system. In collisionless systems, these Equations are the characteristics of the collisionless Boltzmann equation.

Obviously, for large systems, the direct $\mathcal{O}(N^2)$ summation on each body would be impractical and a different approach has to be implemented, in order to reduce the computational cost.

ChaNGa and its predecessor gasoline evaluate gravity through a modified version of the Barnes-Hut algorithm (Barnes and Hut, 1986). Both the codes are based on a spatial binary tree, where the particles are arranged in a hierarchy of groups. In computing the acceleration on a certain particle, the force exerted by distant groups is approximated by a multipole expansion of the entire groups. In this way, the computational cost for a complete force evaluation can be reduced to order $\mathcal{O}(N \log N)$ (Appel, 1985).

Operatively, the computational domain is recursively subdivided into a sequence of nodes or cells, bisecting the longest axis of each cell in order to keep their axis ratio close to one. The tree is constructed such that the root node represents the entire simulation space and the children represent sub-regions. The leaf nodes of the tree are buckets containing only a small amounts of particles.

After the domain decomposition, which is stopped when n_{bucket} or fewer particles remain in a leaf, the codes calculate the force exerted by the node onto each particle using the multipole expansion of the gravitational potential produced by the particles within the node itself. This process is then iterated for each node.

In particular, if $\boldsymbol{r}_{\mathrm{CM}}$ is the centre of mass of the node, Equation 4.1 can be written as

$$\boldsymbol{a}_i = G \sum_{i \neq j}^{N} \frac{m_j}{|\boldsymbol{r}_i - \boldsymbol{r}_{\mathrm{CM}} + \boldsymbol{r}_{\mathrm{CM}} - \boldsymbol{r}_j|^2}, \tag{4.2}$$

and the Newtonian potential becomes

$$\Phi(\boldsymbol{r}_i) = -G \sum_{i \neq j}^{N} \frac{m_j}{|\boldsymbol{r}_i - \boldsymbol{r}_{\mathrm{CM}} + \boldsymbol{r}_{\mathrm{CM}} - \boldsymbol{r}_j|}. \tag{4.3}$$

Assuming that the position of each particle in the node is sufficiently close to the node centre of mass, so that the position $\boldsymbol{r}_i$ satisfies the condition $|\boldsymbol{x}| = |\boldsymbol{r}_i - \boldsymbol{r}_{\rm CM}| \gg |\boldsymbol{r}_j - \boldsymbol{r}_{\rm CM}|$, the denominator of Equation 4.3 can be Taylor expanded. For instance, the first two expansion terms are

$$\frac{1}{|\boldsymbol{x} + \boldsymbol{r}_{\rm CM} - \boldsymbol{r}_j|} = \frac{1}{|\boldsymbol{x}|} + \frac{1}{2}\frac{\boldsymbol{x}^T\left[3(\boldsymbol{r}_{\rm CM} - \boldsymbol{r}_j)(\boldsymbol{r}_{\rm CM} - \boldsymbol{r}_j)^T - (\boldsymbol{r}_{\rm CM} - \boldsymbol{r}_j)^2\right]\boldsymbol{x}}{|\boldsymbol{x}|^5} + \dots \tag{4.4}$$

The first term is the monopole moment and the second one is the quadrupole moment.[1]
ChaNGa and gasoline use the fourth (hexadecapole) order multipole moments to represent the mass distribution in cells at each level of the tree.

Since the particle ensemble is treated as a collisionless system, the codes adopt a sphere around each particle where the particle mass is smoothed. The radius of this spheres is the *gravitational softening*, ϵ, and the smoothing for a particle of mass m_j is defined by

$$\rho(r) = m_j w(q), \tag{4.5}$$

where, in this case, $q = r/\epsilon$, and the smoothing kernel, from Monaghan (1992), is a spline of the form

$$w(q) = \frac{K_D}{h^D}\begin{cases} 1 - \frac{3}{2}q^2 + \frac{3}{4}q^3, & 0 \le q \le 1, \\ \frac{1}{4}(2-q)^3, & 1 < q \le 2, \\ 0, & q > 2, \end{cases} \tag{4.6}$$

with D, number of dimensions, and K_D, normalization constant assuming the values $\frac{2}{3}$, $\frac{10}{7\pi}$, and $\frac{1}{\pi}$ in one, two, and three dimensions, respectively. It is clear that the convergence with Newtonian gravity is obtained at two softening lengths.
In both the codes the same spline is also applied for SPH (see § 4.1.2).

The codes compute the gravitational force that acts on to each particle by walking the tree structure and summing up the proper contribution from each node. To do so, each cell is marked with an *opening radius* $r_{\rm open}$, defined as

$$r_{\rm open} = \frac{2B_{\rm max}}{\sqrt{3}\theta}, \tag{4.7}$$

where $B_{\rm max}$ is the maximum distance of a particle within the node, and θ is the *opening angle* (see Figure 4.1).

When the codes walk the tree, they open only the cells whose opening radius intersects the distance B_i, for each bucket B_i. If a cell is opened, the criterion is tested again for the cell sub-regions. Otherwise the contribution of the cell to the bucket B_i is computed as a whole. Figure 4.1 exemplifies this opening criterion.

An important feature provided by both the codes, in order to accurately simulate a fraction of an infinite universe, is the possibility of performing

[1] The dipole vanishes when the expansion is relative to the group centre of mass.

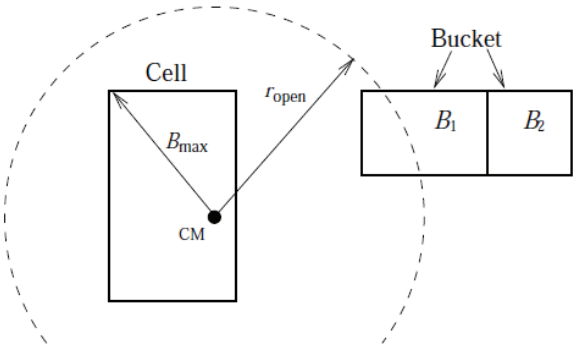

Figure 4.1: Schematic representation of the opening criterion for the codes GASOLINE and CHANGA. Here the opening radius of the cell intersects the bucket B_1, but not the bucket B_2. (Figure from Wadsley, Stadel, and Quinn 2004).

the gravity calculation with periodic boundary conditions. The convergence is rapidly obtained through Ewald summation (Ewald, 1921), implemented similarly to Ding, Karasawa, and Goddard (1992).

4.1.2 Hydrodynamics

The use of SPH (Gingold and Monaghan, 1977; Lucy, 1977) is a natural extension for particle-based gravity codes. Indeed, among the Lagrangian approaches to evaluate the hydrodynamic force, also this technique approximates the fluid through a set of tracer particles.

CHANGA implements the same method of GASOLINE to solve the Euler equations. The computation has two stages. In a first moment (i), for each gaseous particle i, a *hydrodynamical smoothing length* h_i is determined and the neighbouring particles inside its smoothing radius are found. By varying the smoothing length h_i of each particle, this number of neighbours is kept either fixed or, at least, roughly constant. Thus h_i, adjusts to the local particle density adaptively, leading to a constant mass resolution, independent on the density of the flow. The procedure to find the neighbour particles, needed for the SPH kernel sums, takes advantage of the already-built tree structure used for the Barnes-Hut algorithm.

In the second phase, (ii) the hydrodynamical properties of the gas (i.e. the density, the internal energy, and the pressure) and of the hydrodynamical forces are evaluated.

A typical smoothed value for a certain quantity f at particle i, due to the particles j at positions $\boldsymbol{r}_j$ is given by

$$f_{i,\text{smoothed}} = \sum_{j=1}^{n} f_j W_{ij}(|\boldsymbol{r}_i - \boldsymbol{r}_j|, h_i, h_j), \tag{4.8}$$

where W_{ij} is a kernel function symmetric for the conservation of energy and momentum. ChaNGa and gasoline employ the kernel-average proposed by Hernquist and Katz (1989):

$$W_{ij} = \frac{1}{2} w\left(\frac{|\boldsymbol{r}_i - \boldsymbol{r}_j|}{h_i}\right) + \frac{1}{2} w\left(\frac{|\boldsymbol{r}_i - \boldsymbol{r}_j|}{h_j}\right). \tag{4.9}$$

Here, w is the same spline of Equation 4.6, with $q = \frac{|\boldsymbol{r}_i - \boldsymbol{r}_j|}{h}$.

Once the hydrodynamical smoothing lengths and the list of neighbours have been found for each SPH particle, the codes are able to evaluate the density at the fluid particle i, given particles j:

$$\rho_i = \sum_{j=1}^{N} m_j W_{ij}. \tag{4.10}$$

The evaluation of the hydrodynamical force for the gaseous particles is performed through the Euler equation

$$\boldsymbol{a}_i^{gas} = -\left(\frac{\nabla P}{\rho}\right)_i + \boldsymbol{a}_i^{\text{visc}}, \tag{4.11}$$

where $-\left(\frac{\nabla P}{\rho}\right)_i$ is a term related to the gas pressure and $\boldsymbol{a}_i^{\text{visc}}$ is the viscous component of the hydrodynamical acceleration.

The codes assume ideal gasses, with equation of state

$$P_i = (\gamma - 1)\rho_i u_i, \tag{4.12}$$

where u_i is the internal energy per unit of mass, and γ is the polytrophic index. Given the expression of the pressure, the force onto each SPH particle is evaluated as follows:

$$\boldsymbol{a}_i^{\text{gas}} = \frac{\mathrm{d}\boldsymbol{v}_i}{\mathrm{d}t} = -\sum_j m_j \left(\frac{P_i}{\rho_i^2} + \frac{P_j}{\rho_j^2} + \Pi_{ij}\right) \nabla_i W_{ij}, \tag{4.13}$$

where $\boldsymbol{v}_i$ is the velocity, P is the pressure, and Π_{ij} contains the information about the viscous component. This term is defined by

$$\Pi_{ij} = \begin{cases} \frac{\left[-\alpha\frac{1}{2}(c_i + c_j)\mu_{ij} + \beta\mu_{ij}^2\right]}{\frac{1}{2}\rho_i + \rho_j} & \text{if } \boldsymbol{v}_{ij} \cdot \boldsymbol{r}_{ij} < 0 \\ 0 & \text{otherwise} \end{cases}. \tag{4.14}$$

Here, μ_{ij} is given by the relation

$$\mu_{ij} = \frac{(h_i + h_j)(\boldsymbol{v}_{ij} \cdot \boldsymbol{r}_{ij})}{\boldsymbol{r}_{ij}^2 + 0.01(h_i + h_j)^2}, \tag{4.15}$$

where $\boldsymbol{r}_{ij} = \boldsymbol{r}_i - \boldsymbol{r}_j$, $\boldsymbol{v}_{ij} = \boldsymbol{v}_i - \boldsymbol{v}_j$, and c_i (c_j) is the sound speed. $\alpha = 1$ and $\beta = 2$ are parameters used to represent shear and Von Neumann-Richtmyer viscosities, respectively.

For highly rotating systems, the Balsara (1995) b_i switch is added as a multiplicative term, in order to suppress the viscosity in non-shocking, shearing environments:

$$b_i = \frac{|(\nabla \cdot \boldsymbol{v}_i)|}{|(\nabla \cdot \boldsymbol{v}_i)| + |(\nabla \times \boldsymbol{v}_i)|} \tag{4.16}$$

The pressure averaged internal energy is set, for each gas particle, at the beginning of the simulation and is evolved as follows (Evrard, 1988; Benz, 1989):

$$\frac{\mathrm{d}u_i}{\mathrm{d}t} \frac{P_i}{\rho_i^2} \sum_{j=1}^{n} m_j \boldsymbol{v}_{ij} \cdot \nabla_i W_{ij}. \tag{4.17}$$

4.1.3 Parallelization approach

The major improvement brought by ChaNGa lies in the use of a new extensive and innovative parallelization procedure, thanks to the parallel programming system Charm++. The introduction of Charm++ allows to write extremely complex parallel applications, independently of the machine architecture.

Cosmological simulations are challenging not only because of the vast number of particles, but also because of the way they assemble. Indeed, the evolution of a dense system would require a shorter time-step in order to reduce the error on the force evaluation, and this would contribute to enhance the computational burden. In this context, ChaNGa proved to be very versatile in evolving significantly clustered datasets of particles, being able to investigate an immense dynamical range and a great density contrast thanks to its algorithms of load balancing. The computational load is more frequently subdivided among the processors to optimize the resources and lower the number of idle processors.

During the tree building process, various decomposition techniques allow to overlap the communication with the computation and the load balancing features, thus greatly reducing the latency in the processes.
Charm++ runtime system is also able to efficiently overlap the communication latencies of SPH with the gravity calculations.

Another interesting upgrade is the introduction of the *Cache Manager*, a software able to speed up and optimize the communication among the processors, when they share interacting particles in the tree.

ChaNGa showed strong scaling results for uniform datasets on up to 512K cores, and good performance on up to 128K cores for strongly clustered systems. The notable efficiency of the code is well documented in Menon et al. (2015), Jetley et al. (2008), and Jetley et al. (2010).

4.2 The Eris suite

The Eris-suite simulations (Eris, Guedes et al. 2011; ErisLE, Bird et al. 2013; ErisBH, Bonoli et al. 2016; and Eris2k, Sokołowska et al. 2016; Sokołowska et al. 2017) succeeded in reproducing a set of realistic Milky Way (MW)-sized spiral galaxies in zoom-in cosmological volumes, thanks to a smart management of

the feedback receipts, and provide a fruitful laboratory to explore numerous physical processes in a cosmological context.

My work is based on the analysis of two simulations of the Eris suite, Eris2k and ErisBH, both run with the N-body, smoothed particle hydrodynamics code GASOLINE (Stadel, 2001; Wadsley, Stadel, and Quinn, 2004).

All simulations in the suite share the same cosmological parameters (from the Wilkinson Microwave Anisotropy Probe three-yr data: $\Omega_{\rm M} = 0.24$, $\Omega_\Lambda = 1 - \Omega_{\rm M}$, $\Omega_{\rm b} = 0.042$, $h = 0.73$, $n = 0.96$, and $\sigma_8 = 0.76$; Spergel et al. 2007) and the same cosmological box of (90 comoving Mpc)^3, within which a low-resolution DM-only simulation with 300^3 DM particles is run from redshift $z = 90$ down to[2] $z = 0$. After a target halo (with mass similar to that of the MW halo and a quiet late merging history, i.e. with no major mergers – above a mass ratio of 0.1 – after $z = 3$) is chosen, a zoom-in hydrodynamical simulation is performed with 1.3×10^7 DM particles and 1.3×10^7 gas particles within a Lagrangian sub-volume of (1 comoving Mpc)^3 around such a halo. The mass and spatial resolution in the high-resolution region are given by the mass of DM ($m_{\rm DM} = 9.8 \times 10^4$ M$_\odot$) and gas ($m_{\rm gas} = 2 \times 10^4$ M$_\odot$) particles, and by the gravitational softening of all particle species: $\epsilon = 1.2/(1+z)$ physical[3] kpc for $90 \geq z > 9$ and 0.12 kpc for $z \leq 9$.

4.2.1 ErisBH: the parent run

ErisBH is similar to its predecessor Eris, by including Compton and atomic cooling of primordial gas, heating from a UV background (UVB; Haardt and Madau 1996, hereafter HM96), and metallicity-dependent radiative cooling at low ($< 10^4$K) gas temperatures (see Guedes et al. 2011 for more details). Gas particles belonging to a converging flow that cross the star-formation temperature ($T_{\rm SF} = 3 \times 10^4$ K) and density ($n_{\rm SF} = 5$ atoms cm^{-3}) thresholds can form stars of initial mass $m_* = 6 \times 10^3$ M$_\odot$, each representing a stellar population described by a Kroupa, Tout, and Gilmore (1993) – hereafter K93 – initial stellar mass function (IMF). Each SN exploding releases 8×10^{50} erg to the neighbouring gas particles following the blastwave prescription in Stinson et al. (2006), hereafter S06.

However, ErisBH differs from Eris by including prescriptions for the formation and growth of MBHs and the feedback that these can exert on to the galactic medium during accretion events (Bellovary et al., 2010; Bonoli et al., 2016). In particular, a MBH can be seeded in a halo only when: (i) the halo does not host any other MBH, (ii) the halo is properly resolved (by at least 100k particles), and (iii) it hosts a dense gas structure with more than 10 particles exceeding a density of 100 atoms cm^{-3}. Every MBH can accrete mass from the surrounding medium following the Bondi–Hoyle–Lyttleton prescription (Hoyle and Lyttleton, 1939; Bondi and Hoyle, 1944; Bondi, 1952):

[2] The Eris2k simulation has been halted at $z \approx 0.3$. See also § 4.2.2 and § 4.2.3.

[3] In the rest of this work, unless otherwise specified, I always report the physical lengths.

$$\dot{M}_{\rm Bondi} = \frac{4\pi G^2 M_{\rm BH}^2 \rho}{(c_{\rm s}^2 + v^2)^{3/2}}, \tag{4.18}$$

where $M_{\rm BH}$ is the mass of the MBH, and ρ, $c_{\rm s}$, and v are the gas density, sound speed, and relative velocity with respect to the MBH, evaluated over the closest 32 SPH particles, respectively. The maximum accretion rate is capped at the Eddington limit (Eddington, 1916),

$$\dot{M}_{\rm Edd} = \frac{4\pi G M_{\rm BH} m_{\rm p}}{\eta \sigma_{\rm T} c}, \tag{4.19}$$

that is computed assuming a radiative efficiency of $\eta = 0.1$. Here, $m_{\rm p}$ is the proton mass, $\sigma_{\rm T}$ the Thomson cross section, and c the speed of light in vacuum. The same efficiency is assumed when computing the radiated luminosity, a fraction $\epsilon_f = 0.05$ of which is coupled to the 32 gas neighbours as a thermal energy injection (see Bellovary et al. 2010 for a detailed description of the implementation of the MBH physics).

The MBH feedback has an impact on to the ErisBH galaxy at early times ($z \gtrsim 2$), in preventing the formation of a central baryonic overdensity, so that at lower redshifts the galactic potential can sustain a central bar (contrary to the Eris case, as discussed in Spinoso et al. 2017; see also Rodionov, Athanassoula, and Peschken 2017). However, the effect of MBH growth at lower redshifts is essentially negligible, as the central object grows at very low rates, for a total accreted mass of only 14 per cent of its final value since $z \approx 1.2$. For these reasons, in the investigations of chapter 5, I turned off accretion and feedback from the central MBH.

As detailed in Spinoso et al. (2017), a strong bar is clearly observable in the centre of the ErisBH disc galaxy at $z = 0$. The bar starts manifestly growing by $z \lesssim 1$ and it is unclear whether the trigger of its growth could be associated to a minor merger occurring at $z \approx 1.2$ (*last minor merger*, or LMM hereon), that indeed imprints a clear non-axisymmetric perturbation in the (already bar-unstable) central region of the galaxy. The merging satellite has a stellar mass of $M_* \approx 1.2 \times 10^9$ $\mathrm{M}_\odot$ and a dark component mass of $M_{\rm DM} \approx 1.5 \times 10^{10}$ $\mathrm{M}_\odot$, to be compared to the dominant galaxy which has $M_* \approx 2.0 \times 10^{10}$ $\mathrm{M}_\odot$ and $M_{\rm DM} \approx 1.1 \times 10^{11}$ $\mathrm{M}_\odot$ within a 20 kpc radius from the centre.[4] Other minor perturbations are present at lower redshifts, the most significant being multiple flybys of a relatively massive satellite at $z \approx 0.65$, 0.35, and 0.15. The stellar mass of such satellite is $M_* \approx 2.1 \times 10^8$ $\mathrm{M}_\odot$, whereas that of its DM component is $M_{\rm DM} \approx 1.4 \times 10^9$ $\mathrm{M}_\odot$. These values are computed shortly before the first closest-approach point, at about 48.1 kpc from the main galaxy.

The ErisBH simulation provides a formidable laboratory in order to investigate the influence of these satellites of cosmic origin and, thus, is the basis for the *"siblings" runs* described in § 4.3.

[4] The reported figures are estimated at $z \approx 1.7$, hence significantly before the merger.

4.2.2 Eris2k

In Eris2k, it is assumed a uniform extragalactic UVB (Haardt and Madau 2012, hereafter HM12) and calculated the cooling rates either in non-equilibrium (in the case of H and He) or in photoionization equilibrium (for the first 30 elements in the periodic table), using pre-computed tables made with CLOUDY (Ferland et al., 1998) and following the model of Shen, Wadsley, and Stinson (2010) and Shen et al. (2013).

Gas particles are allowed to form stellar particles when the gas density $\rho_{\rm gas} > 10^2\, m_{\rm H}$ cm^{-3} (where $m_{\rm H}$ is the hydrogen mass), $T_{\rm gas} < 10^4$ K, and the local gas overdensity is greater than 2.63. When such requirements are met, gas particles are stochastically selected such that $\mathrm{d}M_*/\mathrm{d}t = \epsilon_* M_{\rm gas}/t_{\rm dyn}$, where M_* and $M_{\rm gas}$ are the mass of stars and gas involved, respectively $\epsilon_* = 0.1$ is the SF efficiency, $t_{\rm dyn} = (4\pi {\rm G}\rho_{\rm gas})^{-1/2}$ is the local dynamical time (S06). At each SF event, the newly formed stellar particle (of mass $\sim 6 \times 10^3$ M$_\odot$) represents a stellar population which covers the entire IMF by Kroupa (2001), hereafter K01. Metals and thermal energy are (turbulently) diffused according to the model described in Wadsley, Veeravalli, and Couchman (2008) and Shen, Wadsley, and Stinson (2010).

When a massive star (of mass between 8 and 40 M$_\odot$) explodes as a SN, mass, iron, and oxygen are injected into the surrounding gas, together with $E_{\rm SN} = 10^{51}$ erg, which is deposited as thermal energy, according to the "blastwave model" of S06. In the case of SNae type II, radiative cooling is disabled for twice the survival time of the hot low-density shell of the SN (McKee and Ostriker, 1977).

The simulation results in the formation of a strongly barred disc galaxy which, at $z \approx 0.3$ (when the run has been stopped), has a gaseous, a DM, and a stellar component of 1.7×10^{10}, 1.2×10^{11}, and 3.8×10^{10} M$_\odot$, respectively (evaluated inside a sphere of radius 20 kpc and centred in the centre of mass of the galaxy). The Kron (1980) radius[5] of the system at the same redshift is equal to 3.3 kpc.

4.2.3 ErisBH vs Eris2k

The following is a discussion about the main differences between ErisBH and Eris2k with the aim of providing the necessary context needed by chapter 7.

In the previous sections, one can infer that the original differences between the ErisBH (run down to $z_{\rm end} = 0$) and Eris2k ($z_{\rm end} \approx 0.3$) simulations lie in how (i) gas cooling, (ii) stellar models (including SF and feedback from SNae), and (iii) black hole physics are implemented. Indeed, both simulations include Compton cooling and primordial atomic non-equilibrium cooling in the presence of a redshift-dependent cosmic ionizing background, (HM12 in Eris2k and HM96 in ErisBH). The modelling of metal cooling varies amongst simulations. In ErisBH, cold gas ($T_{\rm gas} < 10^4$ K) can cool from the de-excitation of fine structure and metastable lines (C, N, O, Fe, S, and Si), and is maintained in ionization

[5]The Kron radius is a mass-averaged galaxy radius, which I adopted in order to determine the size of the disc in the main system of Eris2k. See § 7.1, for a formal definition.

equilibrium by a local cosmic ray flux (Bromm et al., 2001; Mashchenko, Wadsley, and Couchman, 2008). In Eris2k, a look-up table is used, in which the cooling rates for the first 30 elements in the periodic table are pre-computed as a function of gas temperature ($10 \leq T_{\rm gas} \leq 10^9$ K), density ($10^{-9} \leq n_{\rm H} \leq 10^4$ cm^{-3}, where $n_{\rm H}$ is the hydrogen number density), and redshift ($0 \leq z \leq 15.1$), using the software CLOUDY and assuming photo-ionization equilibrium (PIE) with the cosmic ionizing background. Cooling is stronger in Eris2k at all temperatures: for $T_{\rm gas} > 10^4$ K, the presence of metals can increase cooling rates even by orders of magnitude (Shen, Wadsley, and Stinson, 2010); for $T_{\rm gas} < 10^4$ K, it was shown that PIE cooling is enhanced with respect to collisional ionization equilibrium cooling (used in ErisBH, assuming that cosmic rays are unimportant), mostly because PIE tables are computed under the assumption of an optically thin gas and therefore overestimate the true metal cooling rates of low-temperature gas (Bovino et al., 2016; Capelo et al., 2018).

As already specified, particles denser than $\rho_{\rm SF}$, colder than $T_{\rm SF}$, and with a local gas overdensity > 2.63 are allowed to form stars, i.e. stochastically converted into star particles according to S06. In particular, stars form in a denser ($\rho_{\rm SF} = 10^2\, m_{\rm H}$ versus $5\, m_{\rm H}$cm^{-3}) and colder ($T_{\rm SF} = 10^4$ versus 3×10^4 K) gas environment in Eris2k than in ErisBH.

At each SF event, the new stellar particles (each of mass $\sim 6 \times 10^3$ M$_\odot$) are a proxy for a stellar population with a given IMF. The different IMF implemented (K01 in Eris2k and K93 in ErisBH) translates into about three times more stars in the mass range 8–40 M$_\odot$ in Eris2k than in ErisBH, for a fixed stellar particle mass (Shen et al., 2013; Sokołowska et al., 2016). Such difference is relevant because stars with mass within that range can explode as SNae, injecting mass, metals, and thermal energy into the surrounding gas, according to the blastwave model of S06. The energy from SNae ($E_{\rm SN} \equiv \epsilon_{\rm SN} \times 10^{51}$ erg per SN, with $\epsilon_{\rm SN} = 0.8$ and $\epsilon_{\rm SN} = 1$ for ErisBH and Eris2k, respectively) heats the surrounding gas particles, which are then allowed to cool radiatively, but only after a cooling shut-off time equal to the survival time of the hot low-density shell of the SN (McKee and Ostriker 1977; in ErisBH) or twice that (in Eris2k), in order to prevent the gas from quickly radiating away the SN energy because of the limited resolution.

In Eris2k, thermal energy and metals are turbulently diffused (Wadsley, Veeravalli, and Couchman, 2008; Shen, Wadsley, and Stinson, 2010), whereas in ErisBH this applies to the thermal energy only. When such mechanism is implemented, the metallicity distribution in the interstellar medium, as a function of the density, becomes smoother: both the formation of low-density zones with high metallicity is prevented, and the total amount of metals inside the galactic halo rises. The major consequence is that the cooling rate is further increased in the galaxy disc, and the SF process is then (slightly) favoured (see Shen, Wadsley, and Stinson 2010 for further details).

Lastly, differently from Eris2k (and from all other simulations in the Eris suite), ErisBH includes additional prescriptions, in the form of seeding, accretion, feedback, and merging of MBHs (see § 4.2.1).

Within this comparison and thoroughly in chapter 7, for different feedback I do not refer only to the SN efficiency parameter $\epsilon_{\rm SN}$, but rather to the "effective feedback" given by the cumulative effect of all sub-grid parameters. On one

Table 4.1: Differences between the ErisBH and the Eris2k runs.

Feature	ErisBH	Eris2k
MBH feedback	Yes	No
UVB	HM96	HM12
$n_{\rm SF}$	5	100
IMF	K93	K01
Shutdown cooling	S06	2×S06
Metal cooling	Low T	All T
Metal & energy diffusion	Not supported	Turbulent

hand, the combined unresolved-physics prescriptions and parameters in Eris2k with respect to ErisBH (enhanced cooling, larger SF density threshold, different IMF, increased SN energy, and longer cooling shut-off time) lead to a globally increased stellar effective feedback in the former simulation (Sokołowska et al., 2016; Sokołowska et al., 2017). On the other hand, the implementation of MBHs in ErisBH leads to a potentially boosted feedback effect in the central regions of the galaxy, although this strongly depends on the mass of the MBH, which in ErisBH reaches $\sim 2.6 \times 10^6$ M$_\odot$ at $z = 0$ (see § 4.2.1).

Both the runs result in the formation of a barred MW-sized disc galaxy of stellar mass $\gtrsim 10^{10}$ M$_\odot$, showing no "classical" bulge component (see § 1.1). The total virial mass of ErisBH (at $z = 0$) is 8.2×10^{11} M$_\odot$ within a virial radius of 265 kpc, whereas the main galaxy in Eris2k (at $z = 0.31$) has a virial total mass and radius of 7.5×10^{11} M$_\odot$ and 211 kpc, respectively.

The stellar surface density[6] Σ_* and its decomposition into sub-components are shown for the final snapshots of the two runs in Figure 4.2. The details of the global properties of the galaxies, of their sub-structures and their dependencies on the different baryonic-physics prescriptions will be the focus of § 7.1 and § 7.2.

[6] Σ_* has been calculated by integrating the mass density in cylindrical bin of height 8 kpc, to ensure that the entire galactic structure is included, minimizing at the same time the contamination by other systems.

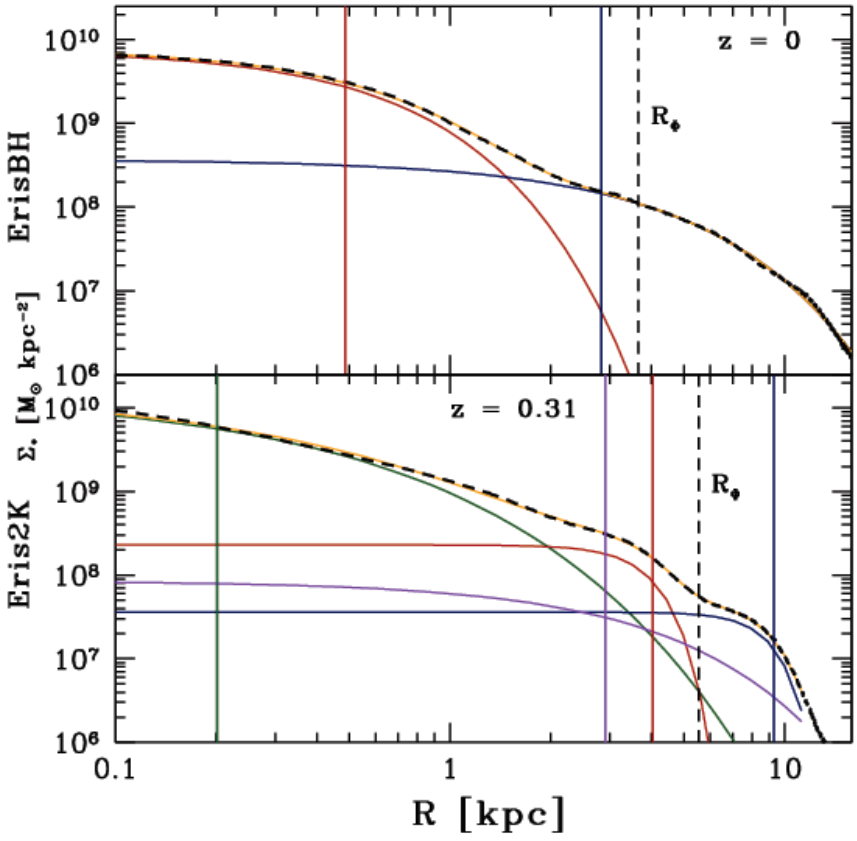

Figure 4.2: Profile decomposition of the stellar surface density Σ_* for the ErisBH (upper panel) and Eris2k (lower panel) runs at their last snapshot. The black lines mark the profiles of Σ_* measured from the snapshots, whereas the yellow lines refer to the best fits obtained with two Sérsic (1963) and Sérsic (1968) components for ErisBH and 3 Sérsic components and an exponential profile for Eris2k. Both galaxies require a stellar disc component (blue curve) and a less extended component (red curve) associated with the stellar bar or, possibly, to its central part inflated into a boxy-peanut bulge in the case of ErisBH (see § 7.3). These two stellar systems are easily recognizable in the closeups of Figure 7.6. Eris2k shows a third, central, component associated to a recent burst of SF fuelled by bar-driven gas inflows (green curve; see § 7.3) and a fourth component (magenta curve) to fit the background. The vertical solid lines mark the position of the scale radii of the corresponding fits with the same colour code, whereas the black dashed lines show the bar length (R_Φ) defined in § 3.2.2. See Appendix A for a description of the fitting method.

4.3 The siblings

In this section I discuss the initial conditions produced from the ErisBH simulation (parent run) and adopted to investigate the effect of tidal interactions on the formation and evolution of its hosted bar.

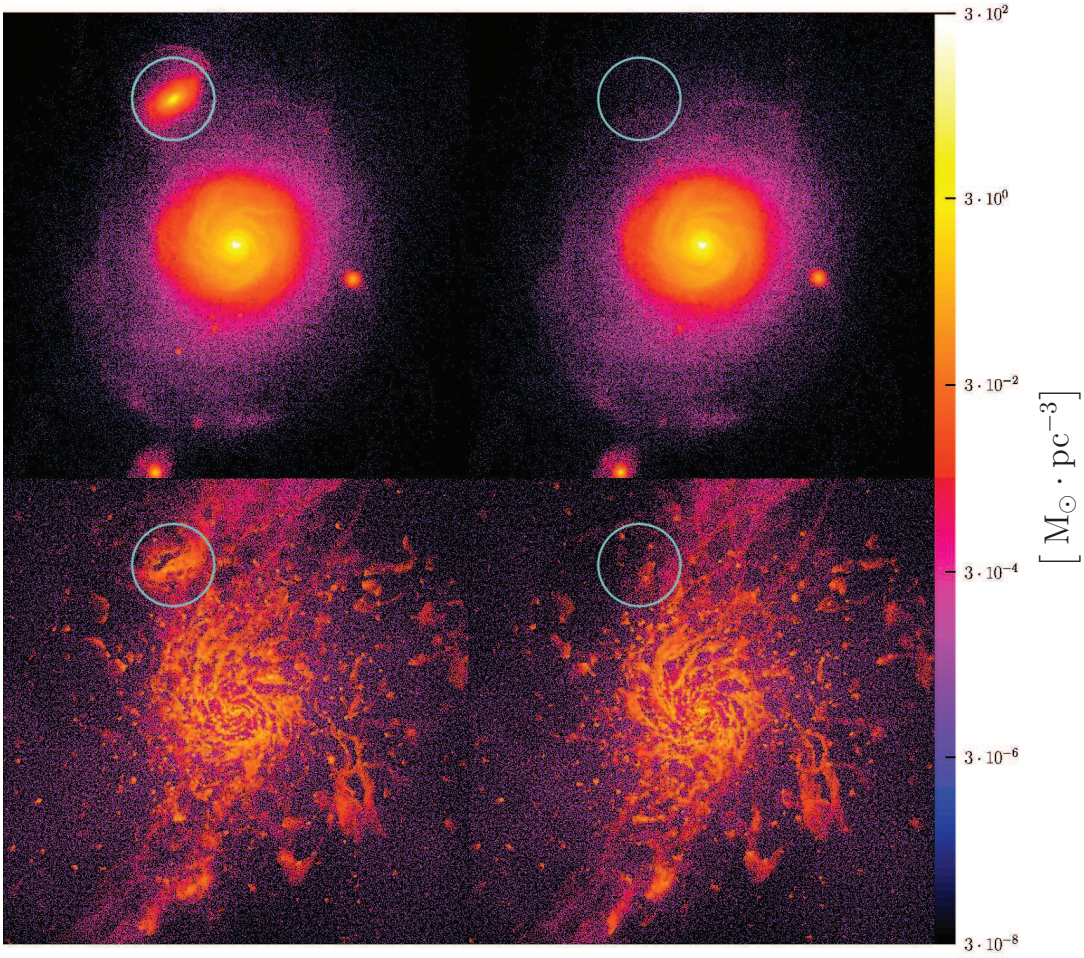

Figure 4.3: Upper panels: stellar density map of the central 50 kpc region for the WM (left panel) and NM (right panel) runs at $z \approx 1.7$. The colour scale is logarithmic spaced with minimum value 3×10^{-8} $\mathrm{M}_{\odot}\mathrm{pc}^{-3}$ and maximum value 300 $\mathrm{M}_{\odot}\mathrm{pc}^{-3}$. Lower panels: same as the upper panels, for the gas distribution. The original location of the companion that merges at $z \approx 1.2$ in the WM run is highlighted in each panel with a circle of radius ~ 5 kpc.

Taking full advantage of the ErisBH run (see § 4.2.1), in order to isolate the influence of various dynamical events over bar formation and evolution processes, I produced five slightly different initial-condition files, starting from a snapshot at $z \approx 1.8$ in the evolutionary history of the original simulation.

All five runs share a number of differences with respect to ErisBH. In particular, (i) I evolved a smaller number of particles (the system is cut at 4500 comoving kpc from the centre of mass of the dominant galaxy), (ii) the MBH

accretion has been switched off to further simplify the setup, and (iii) I could not retrieve whether the gas particles were recently subject to SN feedback.

Since these peculiarities may prevent an accurate comparison between ErisBH and its modified replicas, one of the five runs evolved is a twin simulation of ErisBH (hereon *run WM*), though with the differences noted above. This run allows to check how the aforementioned differences bias the evolution of the system compared to ErisBH.
Chapter 5 is focussed on the comparison between the siblings described below and run WM rather than ErisBH itself, as in this manner the variations introduced at restart can be cancelled out.

The other four runs were re-initialized modifying the initial conditions at $z \approx 1.8$, when the galaxy is already prone to bar instability but no central asymmetries are evident (see Figure 3 in Spinoso et al., 2017), as follows.
In *run NM*, I removed only the satellite which merges at $z \approx 1.2$ in run WM. In order to prevent numerical effects and to maintain the self-consistency of the simulation, I removed the object when it was 40.1 kpc away from the galaxy at $z \approx 1.8$. Figure 4.3 shows a comparison between the stellar and gas density maps for the runs WM and NM in the vicinity of the primary galaxy, at $z \approx 1.7$.
The second largest perturbation to the primary galaxy consists of a flyby, i.e. an object which in the WM run performs three close passages near the central galaxy at $z \lesssim 0.7$. The position of this satellite at $z \approx 1.7$ is highlighted in the left panel (density map of the gas component) of Figure 4.4, whereas a zoom-in and its trajectory during the first pericentre are shown in the right panel of the same figure (stellar density map). *Run NF* is a copy of run NM, except that I also removed the flyby, forcing a dynamical evolution with no significant events after $z \approx 1.2$.

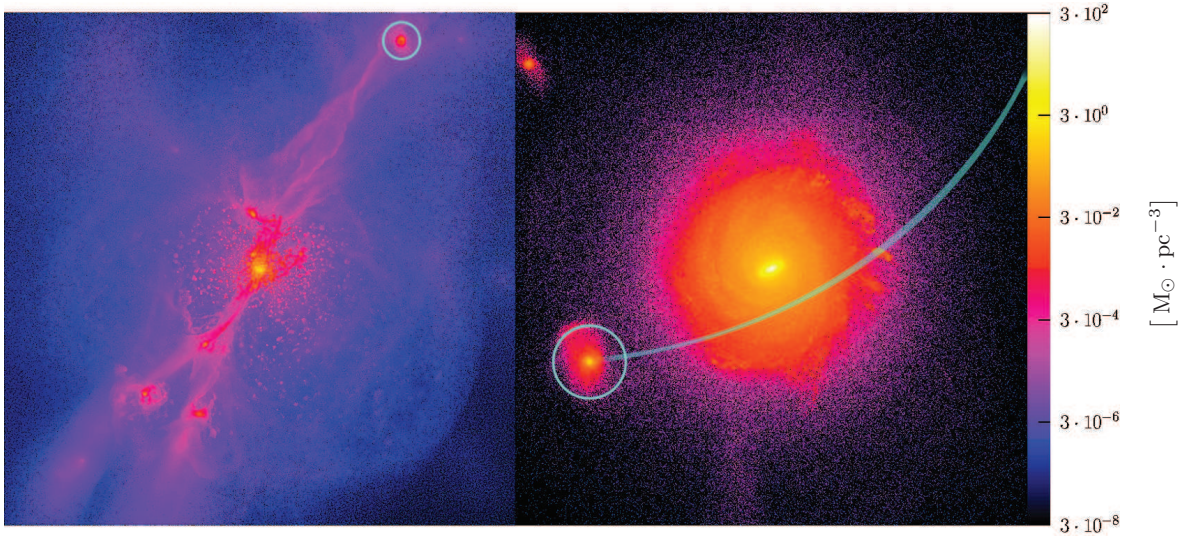

Figure 4.4: Left panel: gas density map for the WM run at $z \approx 1.7$ in a box of side 554 kpc. Right panel: stellar density map of the central 55 kpc from the same run, immediately after the first pericentric passage of the flyby ($z \approx 0.65$). The colour scale is the same applied in Figure 4.3. The position of the flyby location and its trajectory during the closest approach are marked in cyan.

Table 4.2: Summary of the siblings runs.

Run	Extended Name	Details
WM	With Merger	control run
NM	No Merger	no LMM
NF	No Flyby	no LMM & no flyby
PF	Pushed Flyby	no LMM & flyby pushed
HF	Heavy Flyby	no LMM & heavier flyby

In *run PF*, I allowed the formation of the flyby satellite, but I provided it with a velocity radial component in order to push the object away from the central galaxy. This method makes the flyby satellite reach a distance from the main galaxy as large as ≈ 500 kpc at $z \approx 0.5$, thus reducing its influence over the main system.
Finally, in *run HF*, the orbital parameters of the flyby were kept as in run NM, but I doubled the mass of its DM component. The main characteristics of these five runs are summarised in Table 4.2.

The described initial conditions were evolved for a total of approximately 1.0 million CPU hours via the tree-SPH code ChaNGa (Menon et al., 2015), a program for cosmological simulations built on the tree-SPH code gasoline and implemented with the parallel programming system Charm++ (for further details, see § 4.1).

I investigated a temporal window from $z \approx 1.8$ down to $z = 0$, using the same cosmological parameters adopted for the Eris suite. The selected volumes host a total number of particles of about 3×10^7, subdivided in 1.2×10^7 SPH, 1.3×10^7 DM, and 4×10^6 star particles.

In order to preserve continuity with the parent run, both Compton and atomic hydrogen cooling have been included in the adopted code. Moreover, the energetic state of the gas takes into account the same UVB considered in ErisBH (HM96). The process of SF and SN feedback follows again the method described in S06 (efficiencies and other parameters remained unchanged. However, no prescription for MBH accretion and feedback was implemented. The gravitational softening in my suite was kept fixed to 120 comoving pc, implying that the physical softening decreases for increasing redshift.

Chapter 5

The effects of tidal interactions on bar formation

This chapter is addressed to the study of the effect that external perturbations have over the debated process of bar formation (see § 3.3) in MW-like galaxies, by means of state-of-the-art cosmological zoom-in simulations, including the physics of gas dissipation, star formation, and supernova feedback. The target is to characterise the actual trigger of the non-axisymmetric perturbation that leads to the strong bar observable in the ErisBH simulation at $z = 0$, discriminating between an internal/secular versus an external/tidal origin.

In particular, the work focusses on the analysis of several replicas of the ErisBH simulation (Bonoli et al. 2016; see § 4.2.1 for a description of the simulation), a cosmological zoom-in run that led to the formation of a realistic MW-like galaxy hosting a bar in its central few kpc. The properties of the bar and its effect on to the host galaxy and its gas and stellar component have been detailed in Spinoso et al. (2017). Interestingly, the gravitational potential of the main galaxy becomes prone to bar instability in its central region before the last significant merger (with a mass ratio $\gtrsim 0.05$), but develops an observable bar only at later stages (Spinoso et al., 2017). The susceptibility to bar formation was convincingly inferred via the combination of the Toomre Q and swing amplification X parameters for the $m = 2$ mode. As discussed in § 3.3, in collisionless systems, which cannot dissipate energy, these two criteria combined are known to express a necessary condition for bar formation. The aim of this investigation is to identify the actual trigger of the bar formation, in particular whether or not the disc's own self-gravity and structure are responsible for it, or if is instead crucial the role of external perturbations (e.g. infalling satellites).

In order to do so, I analysed the growth history of ErisBH most massive galaxy by identifying the most relevant mergers and flybys. Then I ran a suite of ad-hoc simulations, either removing these interacting galaxies or changing their parameters (orbital or structural, as explained in § 4.3), checked whether a bar would form and, if so, I studied the details of its growth. The rationale

behind “engineering" the simulations by changing a targeted aspect of the initial conditions is similar to the approach followed by Pontzen et al. (2017), who applied small changes in the initial conditions of zoom-in simulations in order to produce different accretion histories leading to the same final mass and environmental properties.

I find that the main effect of a late minor merger and of a close flyby is to delay the time of bar formation and those two dynamical events *are not* directly responsible for the development of the bar and do not alter significantly its global properties (e.g. its final extension). In conclusion, once the disc has grown to a mass large enough to sustain global non-axisymmetric modes, then bar formation is inevitable.

The results of this chapter have been published in Zana et al. (2018c).

5.1 Analysis and results of the simulations

The main goal of this analysis is to assess the actual trigger of the bar instability in the simulation suite described in § 4.3. Hence, I start by checking whether significant differences amongst the five runs, other than the properties of the satellites, actually exist. Since in four out of five runs I removed the LMM, experienced by the central galaxy of ErisBH at $z \approx 1.2$, the mass of the primary galaxy is not exactly the same in all simulations. Figure 5.1 quantifies the redshift evolution of the primary galaxy mass in the different runs considered. Small mass variations are indeed present, still the maximum relative difference in stellar mass is $\lesssim 7$ per cent at both small and large scales, with the largest difference observable in correspondence of the minor merger (the stellar mass of the removed satellite represents $\simeq 6$ per cent of the main galaxy stellar component at $z \approx 1.7$; this value drops to $\simeq 0.9$ per cent by $z = 0$). The gas mass within 20 kpc shows larger variations (about 10 per cent between the different runs).[1] However, the gas mass never exceeds 40 per cent (5 per cent) of the stellar mass within 20 (2) kpc. Star formation from gas infalling through large-scale cold streams (clearly observable in the left panel of Figure 4.4 on page 54) is responsible for the galaxy mass growth during the last ≈ 9.7 Gyr, while mergers with smaller structures are a second-order perturbation to the mass content of the galaxy for $z \lesssim 1.5$. The only notable difference with respect to ErisBH (cyan line in Figure 5.1) is represented by the initially larger gas mass within 2 kpc. The effect can be explained by considering that the new simulations start without gas cooling shut-off by previously exploded SNae, so that the resulting higher star formation rate leads to a rapid consumption of the gas reservoirs.[2]

[1] The gas mass within 2 kpc shows even larger variations at late times. Differences at such small scales are not related to gas-replenishment episodes driven by mergers/flybys, nor to different properties of the large-scale gas streams fuelling the primary; rather, they stem from the difference in the formation time of the bar. See the effect of bars on the interstellar medium in § 1.3.

[2] Although, I often show direct comparisons of my results with ErisBH, it is more meaningful to compare them to run WM, given the actual differences discussed in § 4.3 between these two simulations.

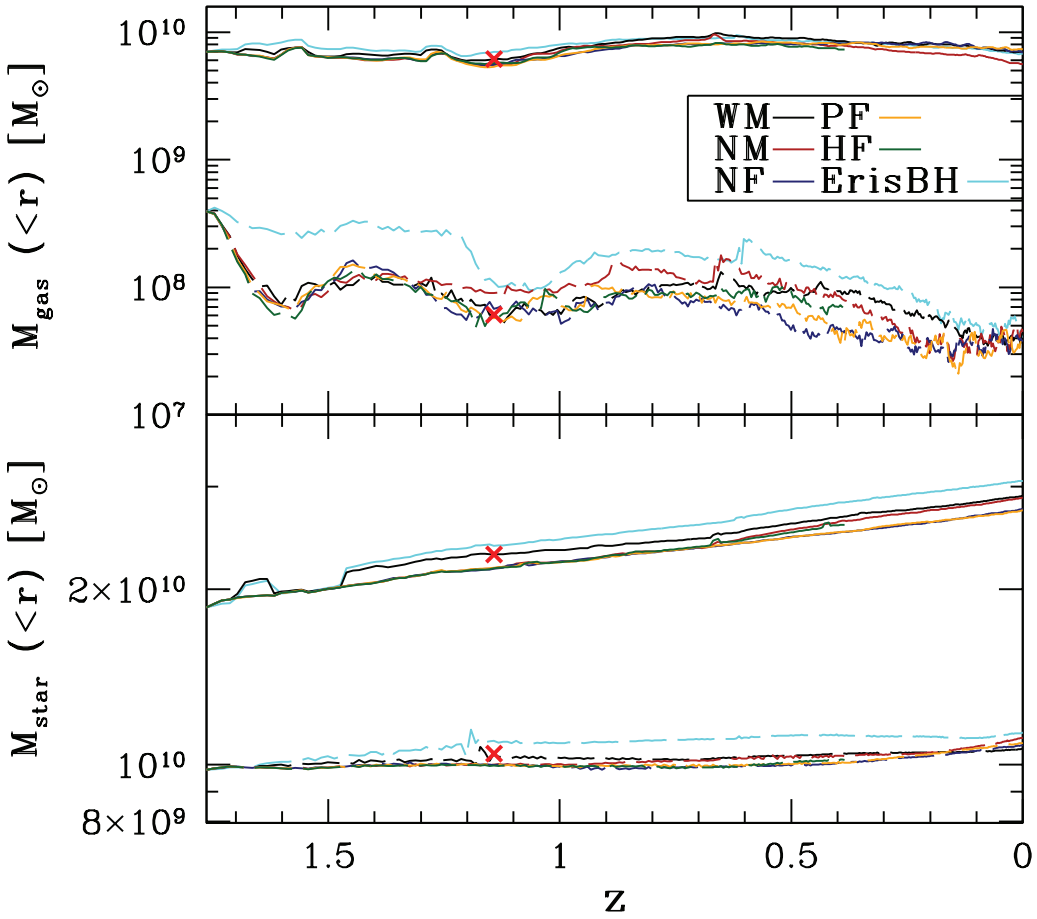

Figure 5.1: Gas (upper panel) and stellar (lower panel) mass enclosed within spheres of 20 (solid lines) and 2 (dashed lines) kpc radii. The comparison with the ErisBH original run is provided by the cyan line. The effect of the LMM in the ErisBH twin run (run WM; black line) can be observed in the sudden stellar mass growth observable at $z \approx 1.5$, when the satellite crosses the 10 kpc boundary. The completion of the merger occurs at $z \approx 1.2$ (this last event is marked with the red cross).

5.1.1 Fourier analysis

Once checked that all the main galaxies share a similar mass evolution, I assess whether different sequences of interactions with the satellites would result in different morphologies of the primary galaxy.

5.1.1.1 Bar strength

The presence (or absence) and the intensity of a central bar have been quantified by performing the Fourier decomposition of the stellar surface density field detailed in § 3.2.1.

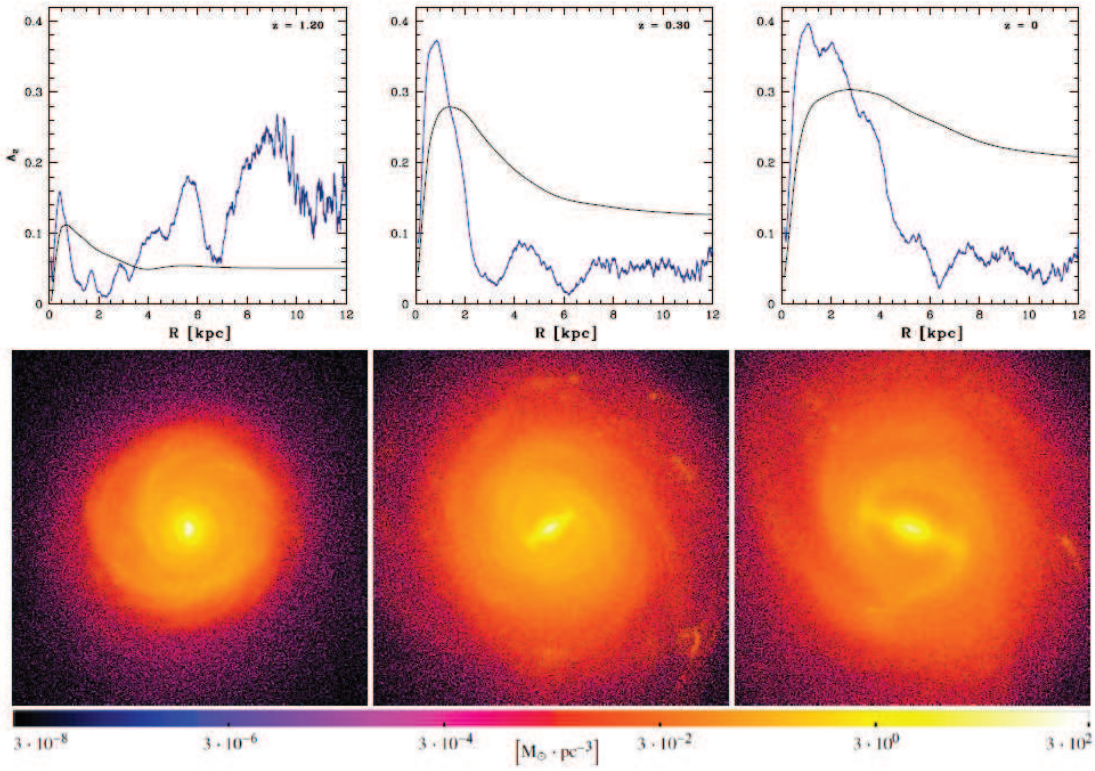

Figure 5.2: The evolution of the $A_2(R)$ profile (blue line) and its cumulative counterpart $A_2(< R)$ (black line) of the primary galaxy in run NM at three different redshifts (upper panels) is reflected in the corresponding stellar density maps (lower panels) of the central 25 kpc, with the same colour coding as in Figures 4.3 and 4.4 (logarithmic colour scale ranging from 3×10^{-8} $\mathrm{M}_\odot \mathrm{pc}^{-3}$ to 300 $\mathrm{M}_\odot \mathrm{pc}^{-3}$.). The major peak of $A_2(R)$ at $R \sim 9$ kpc at $z = 1.2$ is due to the lower density of the outskirts of the galactic disc.

Even though, the bar strength appears to be well represented by the trend of the A_2 cumulative profile (see Figure 5.2), it is worth noting that its value could depend on the CMC of the galaxy. For this reason, it is important to provide the result of the differential Fourier analysis $A_2(R)$ as primary estimator for the intensity of the two-fold non-axisymmetric structure. Both the values are calculated according to Equation 3.1 on page 29, considering only stars within a 1 kpc height.

Figure 5.2 shows for the NM run, at three different redshifts, the $A_2(R)$ profile (blue line) and its cumulative equivalent (black line) as a function of the cylindrical radius R. Each plot is accompanied by the corresponding face-on stellar density map. The plot shows the non-axisymmetric nature of the galaxy disc at three different epochs along the galaxy evolution. It is clear how a two-fold overdensity is evolving, gaining both amplitude and radial extent as the galaxy approaches $z = 0$. This evolution is evident in both lines even if it is also visible that the central density slightly biases the trend of $A_2(< R)$ at larger radii. Nevertheless, it is worth noting that the region of interested is located in the innermost kpc of the galactic disc, where the bar actually forms, and here both the local maxima of $A_2(< R)$ and $A_2(R)$, $A_{2,\max}(< R)$ and $A_{2,\max}(R)$, respectively, provide a reliable estimate of the current strength of the growing non-axisymmetry. The values of $A_2(R)$ have been computed over a much smaller number of particles (each annulus is just a fraction of the total disc volume), thus even a slight variation in symmetry is highlighted in the final result. As a consequence, the differential function fluctuates considerably more than the cumulative one.

The evolution of $A_{2,\max}(R)$ and $A_{2,\max}(< R)$ is shown in Figure 5.3 for all runs, as well as for ErisBH.

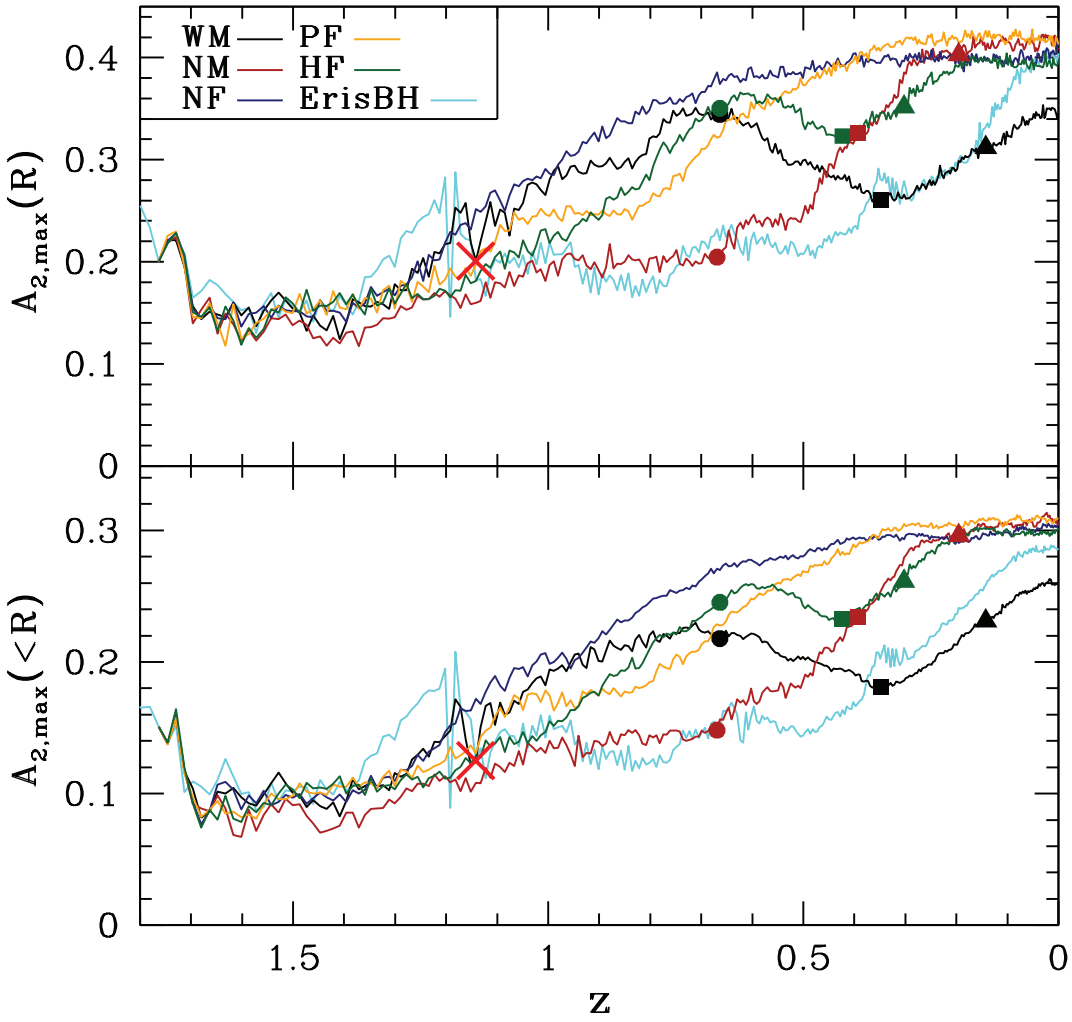

Figure 5.3: Redshift evolution of the bar intensity for the five modified runs, compared with the ErisBH original simulation. The quantities $A_{2,\max}(R)$ (upper panel) and $A_{2,\max}(<R)$ (lower panel) show almost the same trend, proving that the study of the bar growth is not biased by the central mass concentration. The time at which the minor merger occurs in run WM is highlighted with a red cross, whereas the times of the first, second, and third pericentre passages of the flyby are marked as circles, squares, and triangles, respectively.

5.1.1.2 Bar length

The measure of the length of a bar is indispensable for an accurate study of its evolution. Here I apply to every cosmological runs both the methods examined in § 3.2.1, with the technical solution of using $\Phi(R_{\rm max})$ as bar phase. The geometrical boundaries are the same adopted for the computation of the strength (see § 5.1.1.1), whereas the phase ΦR, evaluated through Equation 3.2, is considered constant if its variation is $\Delta\Phi \leq \arcsin(0.15)$.

The results of the two criteria are plotted in Figure 5.4 (R_Φ on the top and $R_{\rm max}$ on the bottom) adopting the same colour code used in Figure 5.3. The values of R_Φ at $z = 0$ are collected in Table 5.1. In the plots, the black lines

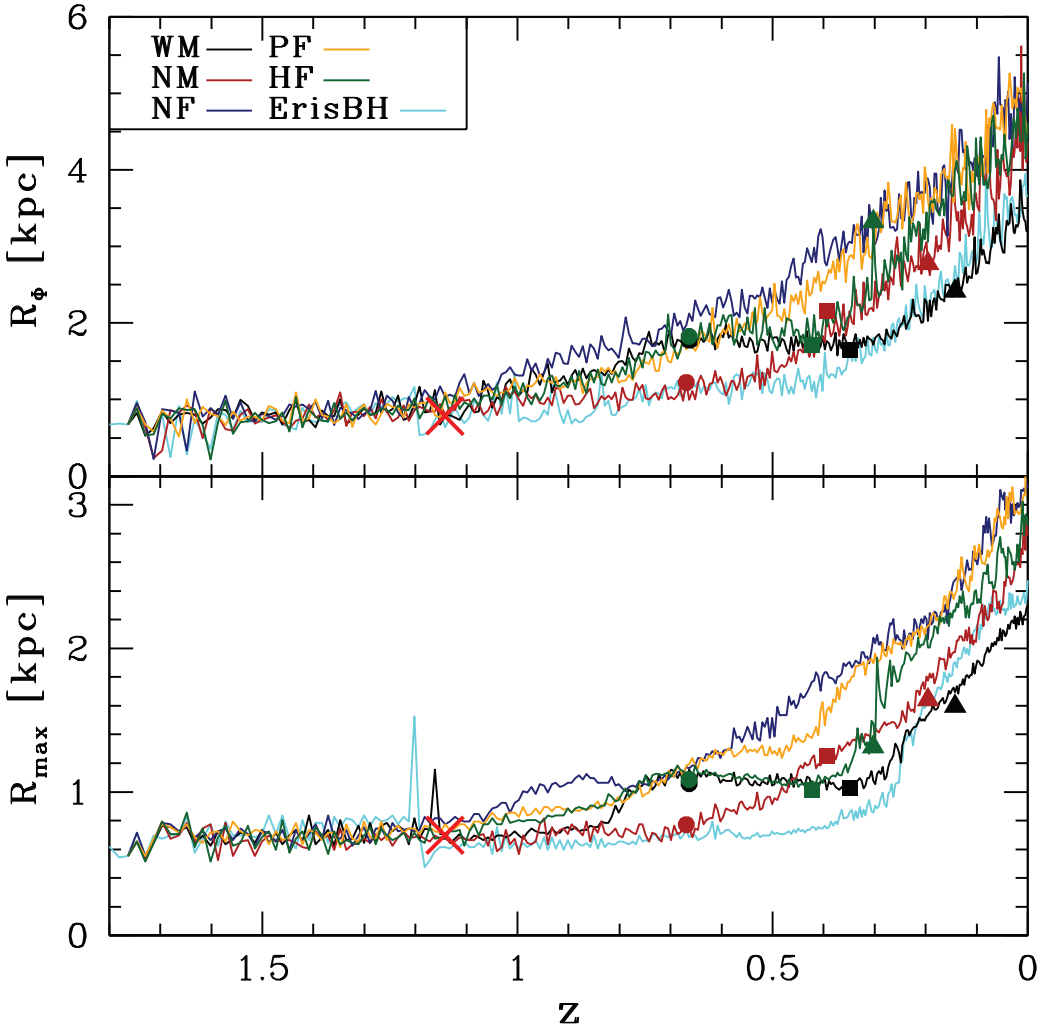

Figure 5.4: Bar extent as a function of redshift: the upper panel shows the evolution of R_Φ, whereas $R_{\rm max}$ is shown in the lower panel. The colour code and the symbol legend are the same adopted in Figure 5.3. The agreement between the trend of the two methods is excellent, though R_Φ is higher at all redshifts.

show the evolution of the inner non-axisymmetric component in run WM. They keep the same qualitative features of ErisBH (cyan) discussed in Spinoso et al. (2017).[3] The single peak of $R_{\rm max}$ at $z \approx 1.2$ is a tracer of the undergoing merger, since, in this method, the approaching satellite determines the position of the maximum asymmetry. This fluctuation is completely absent in the R_Φ-method. Aside from this small difference, both strategies agree with the general growth rate of the bar in all simulations. At this point, I quantitatively analyse the link between the two methods. In particular, for each run, I evaluate the parameter α, in order to maximize the agreement between the function $\alpha R_{\rm max}(z)$ and $R_\Phi(z)$. The results (for $z \lesssim 1$, where a clear bar is present) show that the parameters computed for the different simulation are very close to each other and their mean is equal to $<\alpha>= 1.61 \pm 0.17$. As an example, the functions $R_{\rm max}(z)$ (solid red line), $R_\Phi(z)$ (solid blue line), and $\alpha R_{\rm max}(z)$ (red dashed line) for the run WM are plotted in Figure 5.5.

It should be noted that the agreement factor α does (slightly) depend on the tolerance parameter $\Delta\Phi$. The chosen value for $\Delta\Phi$ is motivated by a number of tests in which I tried to select only the real body of the bars, whilst avoiding phase fluctuations. The low standard deviation, proving that the constant α does not depend on redshift and on the specific run, demonstrates the affinity between the methods.

A transient period of bar weakening in run WM for $0.4 \lesssim z \lesssim 0.7$ is observed both in Figures 5.3 and 5.4, and is possibly linked to the first pericentre of the flyby. Such behaviour is consistent with a scenario in which minor mergers trigger the formation of the bar, whose growth, however, may be delayed by the flyby-induced perturbation. To test such conclusion, I analyse the other runs, where the minor merger is absent. In such runs, despite the lack of the LMM, the main galaxy develops a strong bar anyway, whose final length varies from $\gtrsim 4.3$ kpc (run NM) to $\gtrsim 5.1$ kpc (run NF). These parameters are summarised in Table 5.1. Figure 5.6 offers a qualitative comparison amongst the fully developed structures in each run at $z = 0$ (note that the stellar density map of the run NM at $z = 0$ is provided in Figure 5.2 with the same colour code and scale). It is clear how the bar formation process does not depend on the different dynamical histories of the host galaxy.

The flyby seems not to have any major impact on to the primary galaxy, either. While the first flyby pericentre could be possibly associated to the onset of the bar growth ($z \approx 0.7$ in run NM), a strong bar is nevertheless already in place at the same redshift in the PF run, where the flyby is still too far (~ 700 kpc) to significantly perturb the galaxy. A similar evolution is observable in the HF run, in which the bar starts developing well before the first close passage. The flyby effect here is only a possible delay of the growth of the bar, when the latter is already well formed.

[3] The differences with respect to the analysis performed by Spinoso et al. (2017) are due to the differences between ErisBH and run WM, as mentioned in § 4.3.

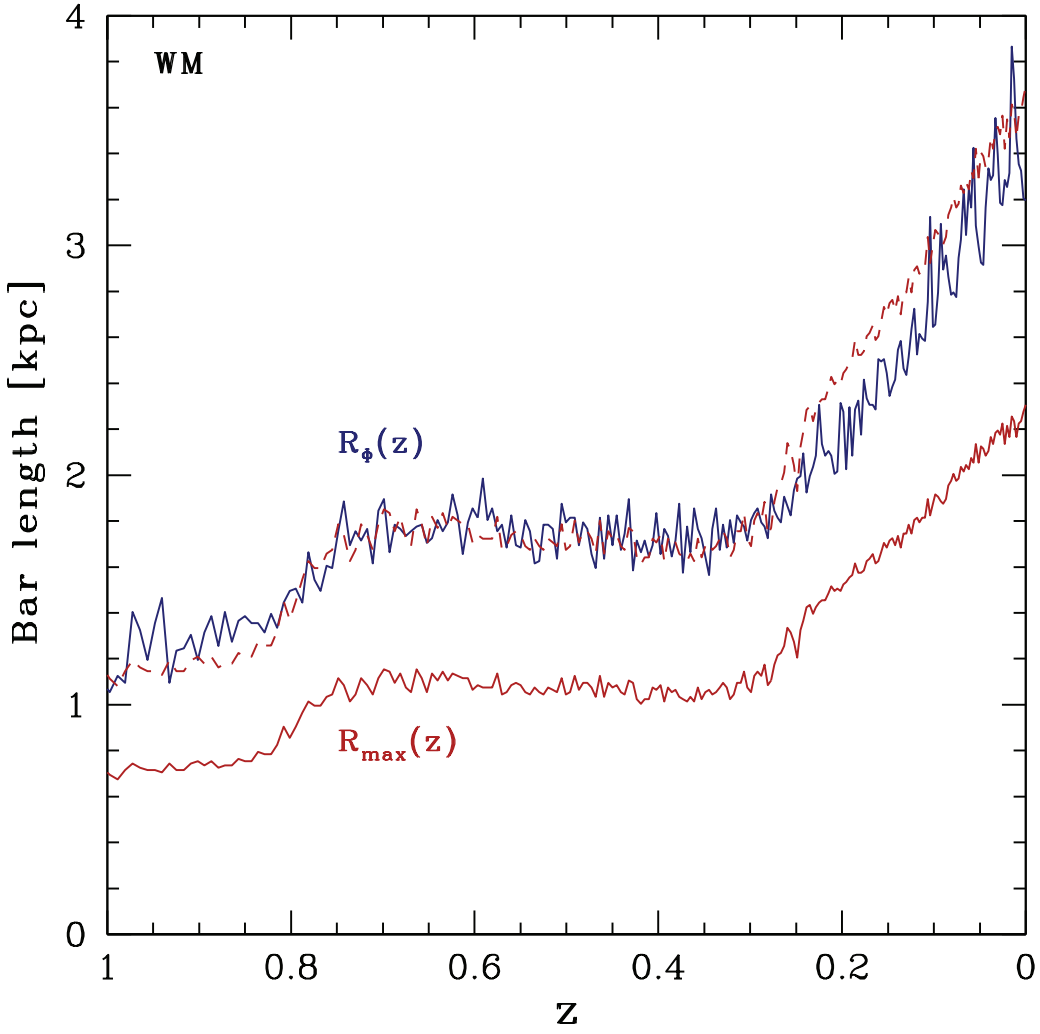

Figure 5.5: Extent estimators as a function of redshift: $R_{\max}(z)$ (red solid line), $\alpha R_{\max}(z)$ (red dashed line), and $R_\Phi(z)$ (blue line). The constant factor $\alpha = 1.58$ (run WM) provides a remarkable agreement for $z < 1$, i.e. the redshift range where a bar is clearly detectable [$A_{2,\max}(<R) \gtrsim 0.1$].

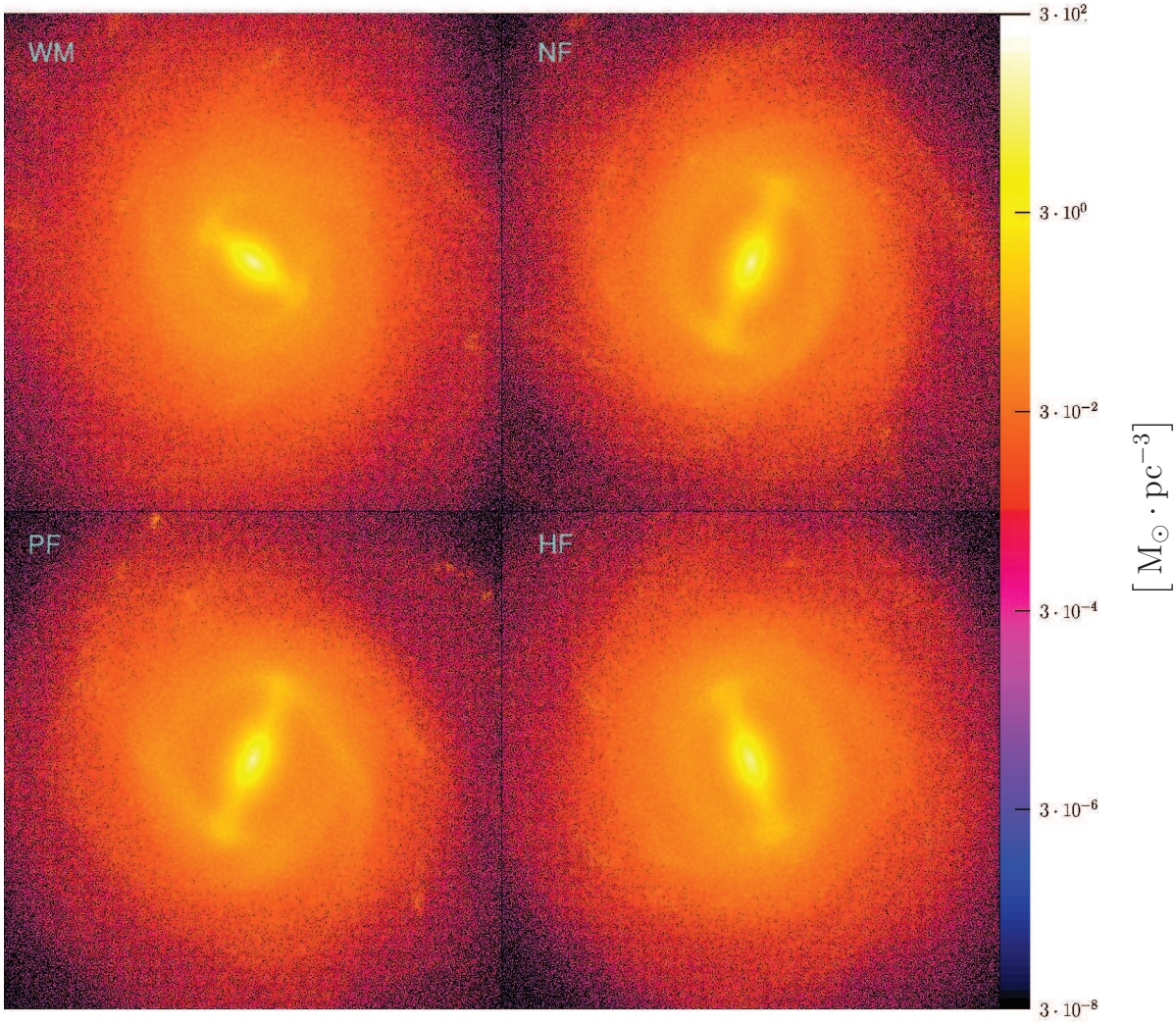

Figure 5.6: Starting from the upper-left panel, face-on stellar density maps of runs WM, NF, PF, and HF at $z = 0$. The colour code is the same used in Figure 5.2, where also the map of run NM is provided.

5.1.2 Properties of the evolved disc

5.1.2.1 Stellar density profile

To check whether the bar evolution produces appreciable changes in the disc profile, here I fit the stellar surface density maps of every galaxy at $z = 0$ using a superposition of two Sérsic profiles (Sérsic, 1963). The indices of the profile (listed in Table 5.1) result close to unity for all the cases, typical for barred discs.

Figure 5.7 shows the stellar surface distribution (black dashed line) as a function of the radius for the runs WM and NF which host two bars at different times of their development (bar growth in run NF has met fewer hurdles and appears to be stronger and longer). The yellow lines, which are the sum of the two Sérsic profiles, show notable agreement with the surface density profile, whereas the red and blue lines follow the distribution of the inner and outer disc components, respectively. The vertical solid lines show the positions of the computed scale radii (red lines refer to the inner disc; blue lines to the outer

disc). The black dashed lines mark the position of R_Φ at $z = 0$, to provide a useful basis for comparison. It is not possible to state that there is an evident correlation between the evolution stage of the bar (assessed by means of the strength and length estimators) and the positions of the scale radii just by assuming the five cases here analysed. In particular, bars in runs NM, NF, PF, and HF have similar evolutions at lower redshifts ($z \lesssim 0.25$) and have similar influences over the disc material. However, run WM, having the less evolved bar in the sample (see Figures 5.3 and 5.4), shows the smallest scale radii and this is in agreement with e.g. Athanassoula and Misiriotis (2002) and Valenzuela and Klypin (2003). It should be noted that the difference in the disc scale radius and extent could be linked to the mass accretion episode at $z \approx 1.2$.

5.1.2.2 Frequency maps

A useful aspect of the analysis is the study of the orbital frequencies of the fully evolved galaxies ($z = 0$). Angular velocities and precession frequencies depend only on the gravitational potential and describe its inherent suitability to grow and sustain a bar (see § 3.3).

In dealing with bar-like structures, it is particularly interesting the study of the precession frequency $\Omega - \kappa/2$, which defines those orbits which would close exactly after two radial oscillations over a period, in a frame corotating with the bar (see also § 3.3). Here, κ is the epicycle frequency, which is linked to the angular velocity $\Omega(R)$ through Equation 2.15 in the epicycle approximation regime (see § 2.2 for further details).

In Figure 5.8, I include the frequency maps for the same two cases (runs WM and NF in the upper and lower panel, respectively) shown in Figure 5.7. In each panel, the black curve shows the angular velocity as a function of radius, whereas the red curve describes the trend of the two-fold precession curve $\Omega(R) - \kappa(R)/2$. The vertical blue line highlights the intersection between the bar frequency ($\Omega_{\rm bar}$, marked in the figure by the horizontal blue line) and the curve $\Omega(R)$. This point, the corotation radius $R_{\rm CR}$, has a major role in orbital theory and sets the upper limit for the bar extent (see Contopoulos, 1980). The shape of the $\Omega - \kappa/2$ curve is typical for galaxies with low central concentration, as in these cases. In both panels of Figure 5.8, $\Omega_{\rm bar}$ crosses the red curve in two points, since the frequency of the bar is below the peak of $\Omega - \kappa/2$: for these values of R the galaxies have their ILR[4]

During the whole galaxy evolution, the bar absorbs angular momentum from the inner regions and redistributes it to the outer disc and the halo (Lynden-Bell and Kalnajs, 1972; Fuchs and Athanassoula, 2005). If the disc is not tidally perturbed, in this process, the bar usually slows down and increases its extent, as discussed in § 3.4.1.

As a direct consequence of this frequency analysis, it is possible to identify the rate of bar rotation through the dimensionless parameter $\mathcal{R} = R_{\rm CR}/R_{\rm bar}$, where $R_{\rm bar}$ is the bar length (defined as R_Φ in this work). As reported by Debattista and Sellwood (2000), bars with $1.0 < \mathcal{R} < 1.4$ are called fast, whereas bars

[4]The runs NM, PF, and HF (not shown in Figure 5.8) all have a similar behaviour.

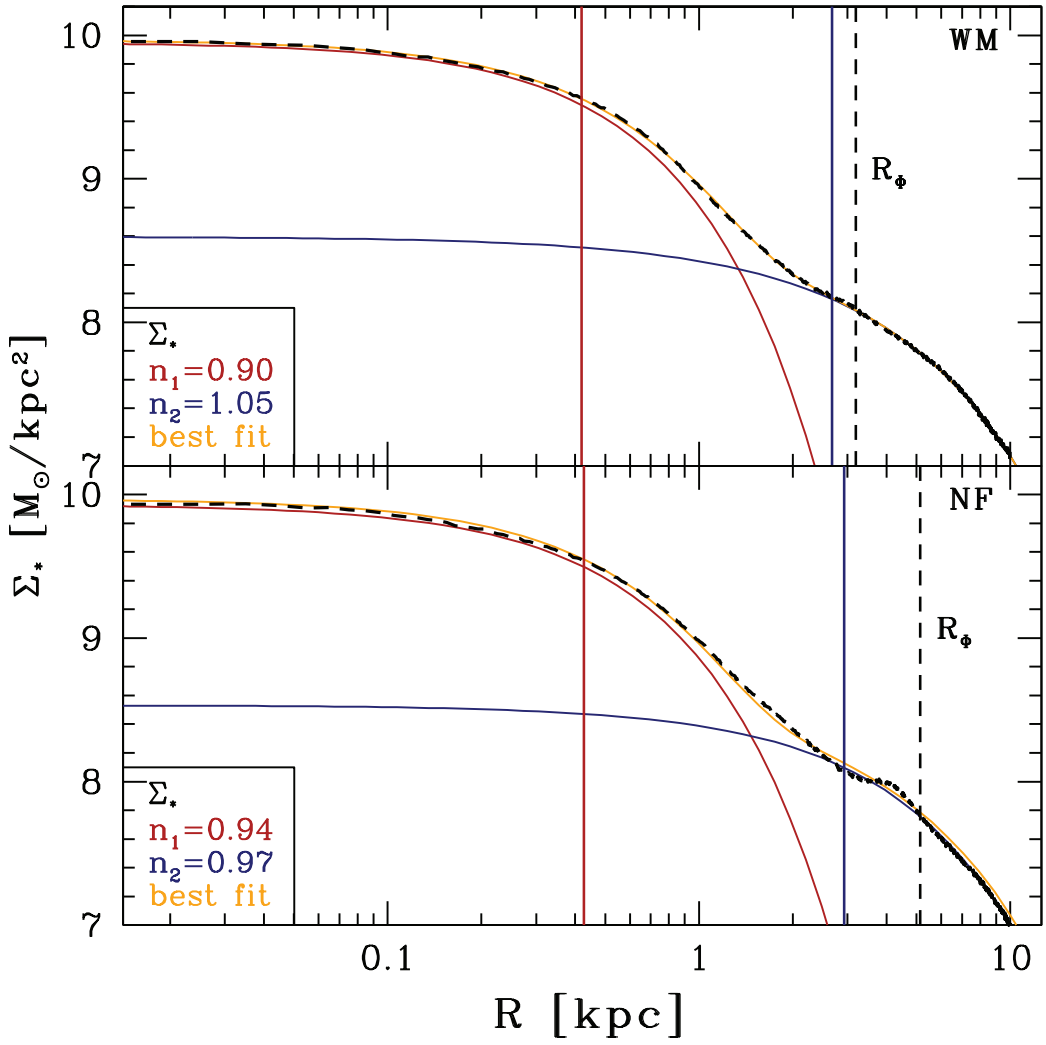

Figure 5.7: Profile decomposition of the stellar surface density for the WM (upper panel) and NF (lower panel) runs at $z = 0$. The black dashed lines display the radial profile of the galactic disc as it has been calculated by integrating the mass density in cylindrical bin of height 8 kpc. The yellow solid line shows the trend of the best fit, whereas the red and the blue lines refer to the inner and outer disc regions, respectively. The vertical solid lines mark the position of the scale radii of the corresponding fits with the same colour code. The black dashed lines show the bar length (R_Φ).

with $\mathcal{R} > 1.4$ are called slow. The ratio $\mathcal{R}$ at $z = 0$ is listed in Table 5.1 for each run. It is clear that, at the final stages of its evolution, each bar can be easily identified as slow, even if the dispersion of the values is large, emphasizing the different evolution histories of the various runs.

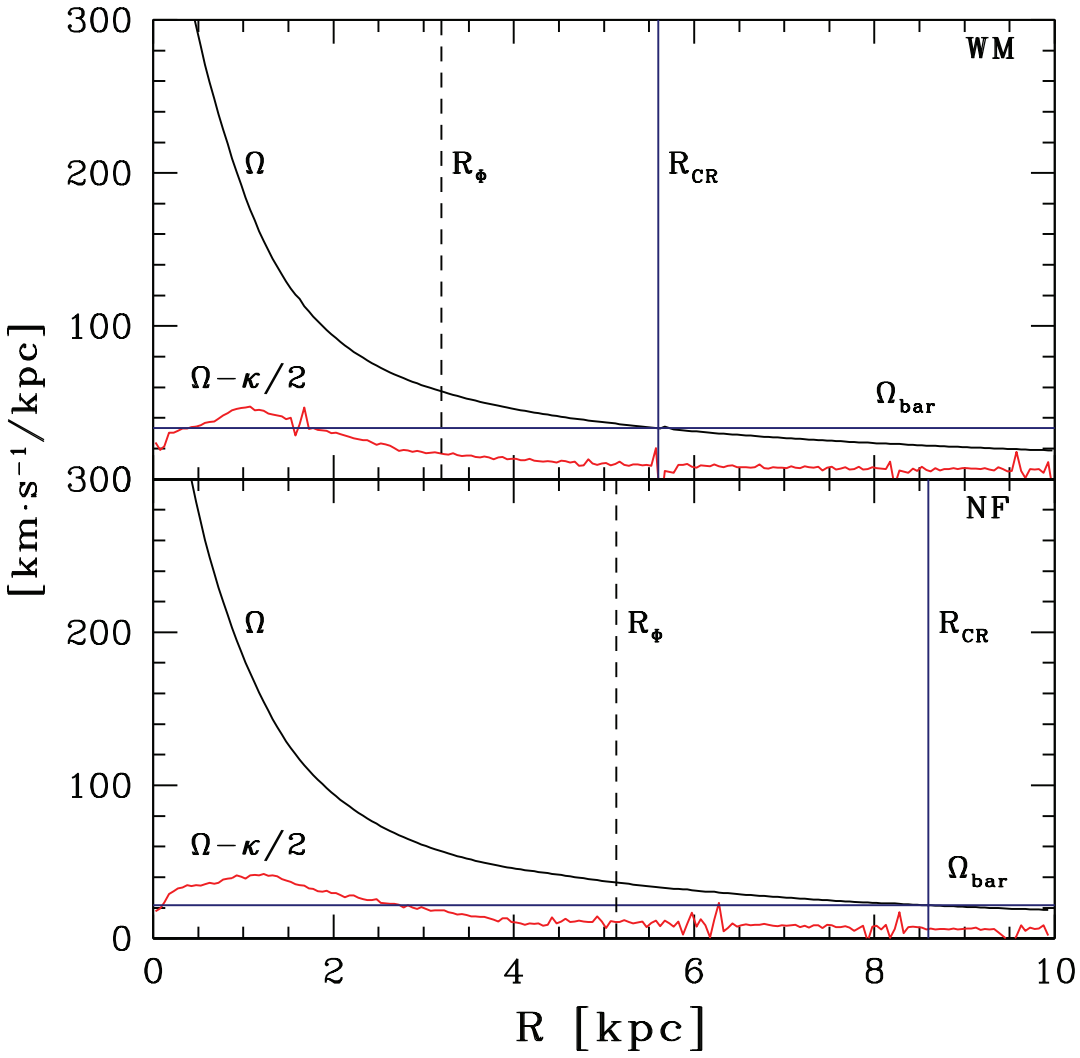

Figure 5.8: Frequency maps of the dominant galaxies in runs WM (upper panel) and NF (lower panel). As in Figure 5.7, the black dashed lines refer to the bar extent at $z = 0$. The black and red curves refer to the angular velocity $\Omega(R)$ and to the precession frequency $\Omega(R) - \kappa(R)/2$, respectively. The horizontal blue lines set the value of the bar angular velocities $\Omega_{\rm bar}$, evaluated at the end of their evolution, whereas the vertical lines highlight the positions of the corotation radii, $R_{\rm CR}$.

5.1.2.3 Boxy/peanut bulge emergence

As argued in § 3.4.1.1, bars arise from the stellar disc and, therefore, at the beginning, they share with it the same vertical density profile. Despite this, after

Table 5.1: Summary of the most relevant properties of the final ($z = 0$) bar for each run. From left to right, columns contain the run identifier, the bar extent R_Φ, the bar length in units of disc scale-radius, the ratio $R_{\rm CR}/R_{\rm bar}$, the indices of the Sérsic profiles adopted to fit the disc surface density, and the presence of the boxy/peanut (B/P) structure.

Run	R_Φ	$R_\Phi/R_{\rm disc}$	$\mathcal{R}$	n_1	n_2	**B/P**
WM	3.195	1.194	1.752739	0.90	1.05	no
NM	4.355	1.274	1.595867	0.94	0.86	yes
NF	5.135	1.753	1.674781	0.94	0.97	yes
PF	4.485	1.642	1.884058	0.93	0.99	yes
HF	4.615	2.045	1.516793	0.84	1.11	yes

a few periods, bars experience some vertical instability processes when their growth continues without interference. This dynamical evolution is considered the cause of the so-called boxy/peanut bulges (see § 3.4.1.1).
In order to assess its development in the various runs, I first select the edge-on projected density field with the bar aligned on the x-axis, for each run at $z = 0$. I then subdivide the surface density field in rectangular bins on the x-axis (in this work, the density on the y-axis is integrated over 15 kpc), and evaluate the z-position of the median density in each bin in the positive and negative z-directions separately (a similar approach has been used in Iannuzzi and Athanassoula, 2015, and is the basis of the procedure applied to ErisBH bar in § 7.3.). The z-positions of the median density as a function of the distance from the centre of the galaxy are shown on the right of Figure 5.9 for each run performed. In addition, each plot is accompanied by the corresponding surface density map. The double-horned shape is clearly observable in almost all the cases, with the only exception of run WM. The clearest structure is visible in run NF. As mentioned above, the bar in run WM is the least developed in the sample. On the contrary, the lack of significant perturbers in run NF favours the monotonic growth of the structure. For this reason, in run NF, the vertical instabilities take place at earlier stages compared to run WM, resulting in a more evolved X-shaped bulge. According to this scenario, the bar in run WM would face a similar fate in its future evolution.

5.2 Discussion and Conclusions

In this analysis, I assessed the nature of the bar resulting from a fully consistent cosmological simulation of a MW-sized galaxy. In particular, I analysed its late evolutionary stages ($z \lesssim 2$), when the central regions are already prone to bar instability, and I checked whether the seed perturbation that triggers the actual bar growth is due to secular/internal processes only, or to tidal perturbations exerted by the evolving background of satellite galaxies.

I ran multiple and different versions of the final phases of the ErisBH simulation, allowing for a modification of the sequence of interactions amongst the main galaxy and its satellites. More specifically, I removed the only minor

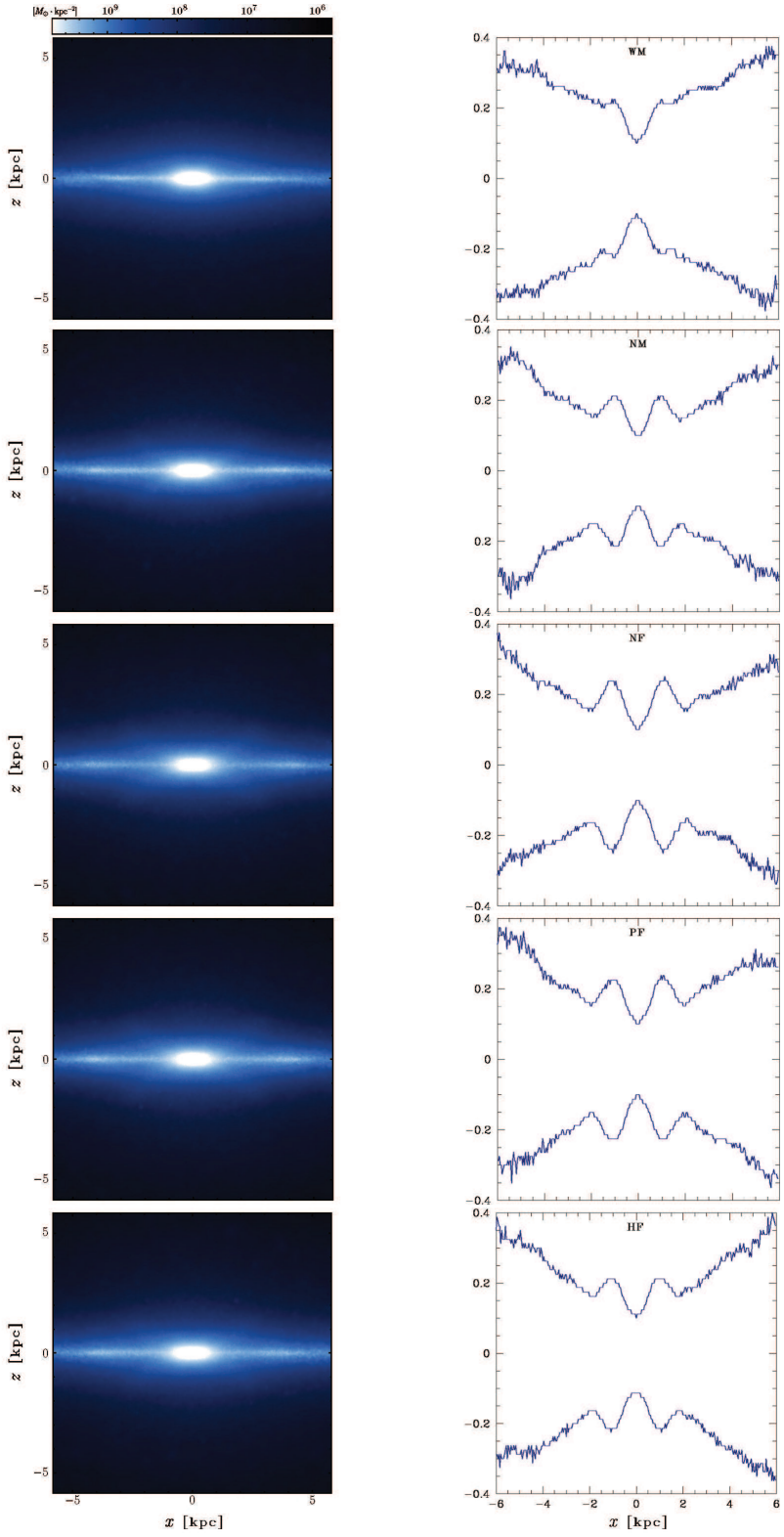

Figure 5.9: On the left, the stellar surface density of the central galaxy is displayed edge-on with the bar major axis parallel to the x-axis. The colour code is logarithmically spaced and the units are $\mathrm{M}_\odot/\mathrm{kpc}^2$. On the right, I show the position of the median density as a function of the distance from the centre of the galaxy, both for the region above ($z > 0$) and below ($z < 0$) the mid-plane. The scale on the x-axis is the same for the maps and the plots, whereas the y-axis scale is enlarged in the right-hand panels in order to highlight the variations. A developed X-shaped overdensity is immediately recognisable in every run, except in the case of run WM.

merger occurring in the galaxy evolutionary history after $z \approx 1.8$, and I changed either the orbital or structural parameters of the closest flyby in the system, or I simply avoided its formation in the galactic neighbourhood. Although all the different runs start at the same point and with the same exact physics and sub-grid physics modules, I did perturb the system to some extent by removing or changing the location of a subset of particles, i.e. modifying the energy and mass content in the box.

I demonstrated that the origin of the bar forming in ErisBH run is not linked to any particular tidal event. Indeed, an even stronger and longer bar forms when the merger does not occur at all. Furthermore, according to § 3.4.1.1, the boxy/peanut shape reflects the bar evolutionary stage, which is more advanced in the runs NM, NF, PF, and HF with respect to run WM. Analogously, the outcome of my experiments shows that no relevant numerical artefact has been introduced with the procedure as this would have had an impact on the dynamical evolution and on the development of the bar itself. This last point is also evident in Figure 5.1, where the primary galaxy evolves almost identically in all cases, suggesting that the numerical noise introduced by the engineering of the dynamical state of the system does not lead to any numerical instability.

Moreover, it seems that the flyby could delay the growth of a bar if such structure is already present, but certainly this interaction cannot be considered itself the trigger of the bar formation, and does not alter the further evolution of the bar properties. The delay could be due to the increase in the stellar velocity dispersion imprinted by the flyby, resulting in a more stable disc (Guedes et al., 2013). This point is similar to what found in chapter 6, where the destructive effect of a tidal perturber is assessed on the Eris2k simulation.

Another run was performed with different initial conditions. This case is similar to the case of HF, but the dark matter component of the flyby has been multiplied five times. I decided not to discuss it here, since its merger history (a further merger takes place at $z \lesssim 1$) does produce a significantly different object at $z = 0$ and, therefore, it cannot be directly compared with the other siblings. Notwithstanding this, the case would fall into the category of the objects whose bar has been strongly suppressed. As mentioned above, some studies claim that the global effect of the gravitational perturbers could be summarised in a growth/formation inhibition (e.g. Li et al., 2009; Lin et al., 2014).

It is interesting to compare my results to similar recent findings obtained by Moetazedian et al. (2017), who detailed the effect of low-mass satellites on the bar growth in a bar-unstable galaxy. The masses, tidal radii, and impact parameters of the perturbers are inferred from the cosmological Aquarius-D simulation (Springel et al., 2008). In agreement with my investigation, Moetazedian et al. (2017) finds that the only effect of the satellites is to either slightly anticipate or delay the bar growth (by at most ~ 1 Gyr), whereas the main properties of the bar as well as its growth rate remain almost identical. My results and those discussed in Moetazedian et al. (2017) complement each other. On one hand, my study takes into account the full assembly history of the main galaxy as well as the effect of gas, whereas both these aspects are not included in Moetazedian et al. (2017). On the other hand, the idealised nature of the Moetazedian et al. (2017) initial conditions results in an higher level of axisymmetry, which

allows for a better characterization of the initial seeding of the bar. As an example, Moetazedian et al. (2017) were able to follow the evolution of the bar strength parameter A_2[5] down to fluctuations of the order of $\simeq 10^{-3}$, well below the physical noise due to the small substructures present in my study. The consistency of the findings in such different studies strongly supports the internal/secular origin of bars in field galaxies.

In summary, I proved that there is no need of a major external perturbation for the formation of the bar in ErisBH. As long as the galactic potential is prone to bar instability, as in the last stages of ErisBH (Spinoso et al., 2017), a bar develops independently of any interaction (if these interactions are not strong enough to considerably modify the galactic potential). This points to the self-gravity of the disc and to its interplay with various internal processes, from cooling to energy input by SN feedback, as the main driver of bar formation and growth, similarly to what seen in simulations of secular evolution of massive spirals (Debattista et al., 2006). In chapter 7, the importance of self-gravity as a consequence of the feedback processes is analysed in detail.

At high redshifts, when galactic discs are still low in mass (hence weakly self-gravitating) and perturbations by tidal interactions and mergers with massive satellites are much more frequent, the role of tidal triggering in bar formation and growth might be more important, as suggested by Guedes et al. (2013) and Fiacconi, Feldmann, and Mayer (2015). Massive spiral galaxies at $z \lesssim 1$ should, instead, belong to the same regime studied in this chapter. This means that the standard scenario of secular evolution does hold, at low redshifts, even in the complex context of hierarchical galaxy formation.

[5]Note that the parameter defined as A_2 in this work is equivalent to A_2/A_0 in Moetazedian et al. (2017).

Chapter 6

The effects tidal interactions on bar evolution

It has been proposed that close interactions with satellite galaxies can significantly perturb the morphology of the main galaxy (see § 3.4.2). Unfortunately, the dynamical response of an already formed bar, following the interaction with the external environment, has not been studied in detail in a fully cosmological context with sufficient resolution.
In chapter 5, I discussed the possible delaying effect of a tidal perturbation on a forming bar. Indeed, almost each analysed galaxy among the siblings (see § 4.3) showed no significant axisymmetry deviations preceding the LMM or the first peripassage of the flyby[1], making the results of the chapter valid only for the process of formation of the bar.[2]

In this chapter, I contribute to the study of the effect of external interactions on to bars, by focussing on the repercussions that cosmologically motivated flybys have on already developed stellar bars. In order to do so, I analyse the state-of-the-art cosmological zoom-in simulation Eris2k (Sokołowska et al. 2016; Sokołowska et al. 2017; see § 4.2.2 for a detailed description of the run). A disc galaxy forms in the centre of the high-resolution region, showing a strong stellar bar extending over more than 5 kpc since $z \approx 1$. Within the Eris suite (see chapter 4), the Eris2k run has the most developed bar both in strength and in length. A deeper comparison between Eris2k and ErisBH (the only other run with a discernible stellar bar; Spinoso et al. 2017) is the topic of chapter 7. The exquisite mass resolution of Eris2k is of paramount importance for this study, since it allows to analyse the effect of a very unequal-mass flyby passing well within the main stellar disc. Such close interactions have been proposed to be the strongest perturbations to the evolution of bars in isolation (Moetazedian

[1] A minimal exception is found in the runs WM and HF, which measure a length of 1.8 kpc both and an $A_2(R)$ strength of 0.34 and 0.35, respectively.
[2] It should be noted that, subsequent passages of the flyby could have had a negative influence on the already growing structure (see, for instance, Figures 5.3 and 5.4).

et al., 2017). A coarser resolution would indeed strongly underestimate the number density of small structures which, being more common, have a higher (non-negligible) chance to experience close pericentric passages at low redshift, after the initial phase of bar growth.

I characterize the evolution of the bar strength and length showing that the perturbation exerted by the flyby shuffles the stellar orbits for less than one Gyr. After this time, the bar shows a remarkable resilience, reforming with properties comparable to those it had before the interaction. This work shows that close unequal-mass encounters, the most frequent interactions occurring during the evolution of cosmic structures, have (i) an overall minor impact on the global evolution of the bar in the long term, still (ii) their effect is destructive and (iii) a very weak interaction is sufficient to dismantle a strong bar leading to its "apparent death". As a consequence, due to the non-negligible duration of the bar-less period, a fraction of observed spiral galaxies classified as non-barred could be prone to bar formation.

All the results are published in Zana et al. (2018a).

6.1 Analysis and results of the simulation

Similarly to what done in chapter 5, I check for the appearance of a stellar bar and for the evolution of its strength by performing a two-dimensional Fourier analysis of the face-on stellar surface density, as explained in § 3.2.
In particular, I apply Equation 3.1 on page 29 both in its differential version, i.e. carrying out the summation over all particles within a shell around the cylindrical radius R, and in its cumulative form, considering every stellar particles from the centre to the radius R.

In addition, I constrain the length of the structure by employing both the methods described in § 3.2.2, i.e. $R_{\rm max}$, from the position of $A_{2,\rm max}(<R)$, and R_Φ from Equation 3.2, adopting $\Delta\Phi = \arcsin(0.15)$ and $\Phi_{\rm bar} = \Phi(R_{\rm max})$.

Operatively, the Fourier decomposition is performed within $R = 12$ kpc by dividing the stellar disc in linearly spaced cylindrical annuli of height 2 kpc.

The evaluation of the bar properties for the main galaxy in Eris2k run is far from straightforward, since the stellar surface density does not show a smooth profile, as in the cases analysed in chapter 5, and presents sometimes more than one non-axisymmetric feature. Thus, the analysis requires some additional steps in order to retrieve the correct bar parameters. The detailed procedure to overcome this problem is described in Appendix B. Here, I merely outline the result as a function of the redshift.

The evolution of the two strength parameters and of the two bar lengths for $z \lesssim 1.5$ are shown in Figure 6.1. A strong bar [i.e. a bar having $A_{2,\rm max}(R) > 0.2$] forms at $z \simeq 1.1$, rapidly increasing its size up to a considerable fraction of the stellar disc: at $z \sim 1$, $R_{\rm max} \gtrsim 4$ kpc and $R_\Phi \simeq 6$ kpc, whereas the Kron radius[3] is ≈ 3 kpc. The bar keeps growing in intensity with an approximately constant length until the end of the run at $z \approx 0.3$, with the only exception of a transient

[3] A mass-averaged galaxy radius. See Equation 7.1.

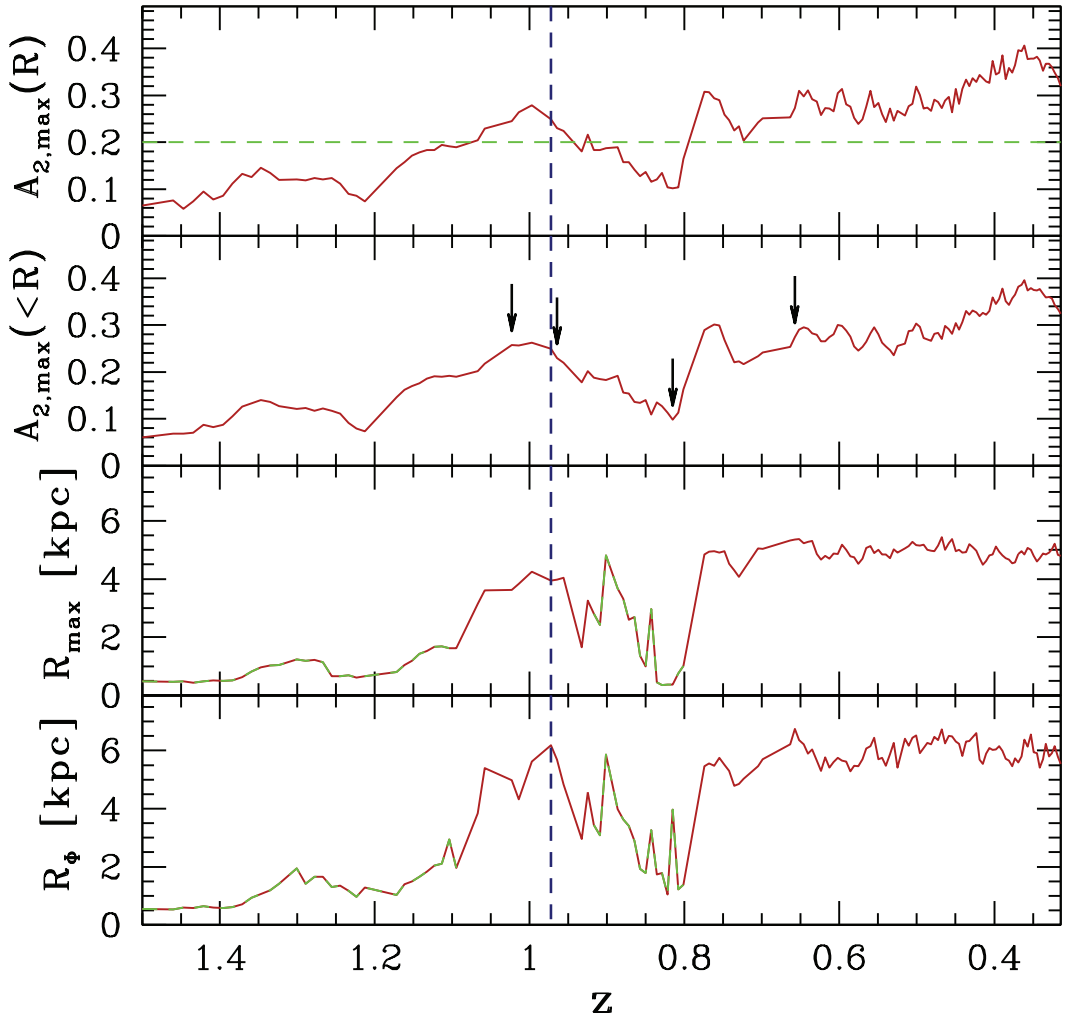

Figure 6.1: Redshift evolution of the bar properties. From top to bottom: the local intensity $A_{2,\max}(R)$ of the bar, its cumulative intensity $A_{2,\max}(< R)$, the radius $R_{\max}$ at which the cumulative intensity peaks, and the bar length R_{Φ} (see text for details). The horizontal, dashed green line in the uppermost panel marks the threshold $A_{2,\max}(R) = 0.2$. The sudden decrease in both the bar-intensity parameter and in the two bar length-scales is clearly observable immediately after the pericentre of the orbit of a satellite (a flyby), marked with a vertical, dashed blue line at $z \sim 1$. The bar length-scales estimated when $A_{2,\max}(R) < 0.2$ (i.e. when a strong bar is not present) are highlighted with green dashes. The four black arrows refer to the snapshots pictured in Figure 6.2 as notable stages in the bar evolutionary history.

weakening at about $0.95 \gtrsim z \gtrsim 0.8$. The weakening corresponds to a lower coherence of the bar structure, making the measurement of the bar extent in this phase more difficult and less significant (this is marked in Figure 6.1 by the dashed green-red lines). However, a clear decrease in the bar extent is still observable in the same redshift interval.

The physical trigger of the transient fading of the bar is the gravitational perturbation of a satellite galaxy undergoing its pericentre at $z \sim 1$ on a prograde orbit, well within the stellar disc ($R_{\rm peri} \simeq 6.5$ kpc). The apocentre-to-pericentre ratio of 6:1 agrees very well with the cosmologically expected value derived by Ghigna et al. (1998). The total (baryonic plus DM) mass of the perturber immediately before the pericentric passage (evaluated at a separation of about 20 kpc) is $M_{\rm sat} \simeq 1.1 \times 10^8$ M$_\odot$, whereas the main system has a total mass $M_{\rm gal} \simeq 1.5 \times 10^{11}$ M$_\odot$. It is important to note that the stellar mass ratio, $q_* \simeq 4.5 \times 10^{-3}$, albeit low, is larger than the total mass ratio since the perturber is not DM-dominated, contrary to the main galaxy.[4] After the bar has formed, the aforementioned perturber is the most massive amongst those objects with similar $R_{\rm peri}$.[5]

The effect of the satellite's passage on to the main galaxy is shown in Figure 6.2 for the four redshifts marked with arrows in Figure 6.1. The upper left panel shows the galactic morphology after the bar formation, but before the satellite's pericentre. A stage close to the pericentric passage is shown in the upper right panel, with the position of the satellite highlighted with a large circle and its position in the three previous snapshots marked with smaller filled circles. The perturbation alters the orbits of the bar's stars, and the bar loses its coherence (see the lower left panel) for ≈ 900 Myr.

The bar reforms with a size and strength very similar to those before the encounter, and this is observable in the lower-right panel. This is because the potential of the galaxy is almost unperturbed by the satellite passage, as shown in Figure 6.3 through the profiles of the orbital Ω and precession $\Omega - \kappa/2$ frequencies[6] before the strong interaction ($z_1 = 1.023$; upper panel in Figure 6.3 and upper-left panel in Figure 6.2) and during the faded-bar phase ($z_2 = 0.815$; middle panel in Figure 6.3 and lower-left panel in Figure 6.2). $\Omega - \kappa/2$ is particularly suited for this test, since its shape is extremely sensitive to small variations in the potential and, for this reason, it is used to determine whether a non-axisymmetric perturbation has Lindblad resonances.[7] The potential profile remains unchanged because the perturbation does not lead to a significant variation in the mass distribution of the disc. I also verified that neither a CMC

[4] Note that, while the satellite's DM halo is strongly affected by tidal stripping, almost its whole stellar component is preserved during the flyby.

[5] A perturber of similar mass and similar $R_{\rm peri}$ is observed at $z \approx 0.35$, concurrent with a small bar-strength decrease. However, in this case, (i) the weakening can be explained with an increasing in the CMC (see § 7.3), and (ii) it is not possible to confirm if the bar would completely disappear in the near future (either permanently or temporarily), since the run ends before $z = 0.3$.

[6] See § 3.2.2 and Equation 2.15.

[7] For instance, the $\Omega - \kappa/2$ profile has been also used to constrain the mass of central massive black holes even when their influence radii are not resolved (see Combes et al., 2014).

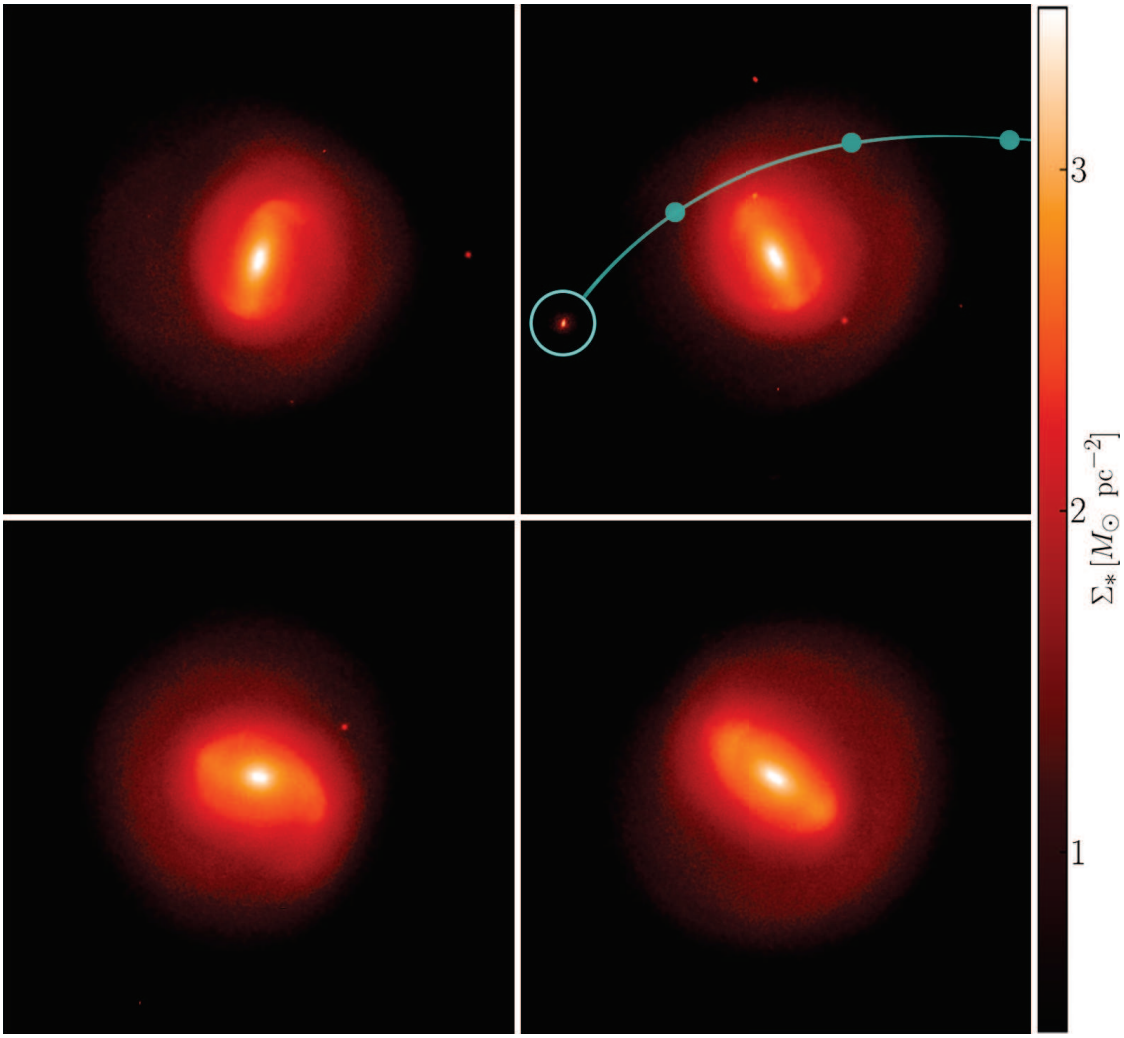

Figure 6.2: Stellar surface density maps (viewed face-on) of the main galaxy at four different redshifts, also marked in Figure 6.1 (black arrows). The upper left panel refers to $z = 1.023$, before the flyby pericentre. The upper right panel ($z = 0.964$) shows the satellite (highlighted with the large circle) soon after its pericentre passage ($z = 0.972$). The positions of the satellite in the previous three snapshots (created every 33 Myr) are highlighted with smaller filled circles. The lower left panel shows the galaxy at $z = 0.815$, when a clear bar is not discernible (in response to the tidal perturbation), whereas the lower right panel shows a later snapshot ($z = 0.658$), after the bar has re-assembled.

grows, nor the bar undergoes any vertical instability during the flyby passage. We have seen in § 3.4.1.1 and in § 3.4.1.2 that these two are competitive processes as bar weakening mechanisms.

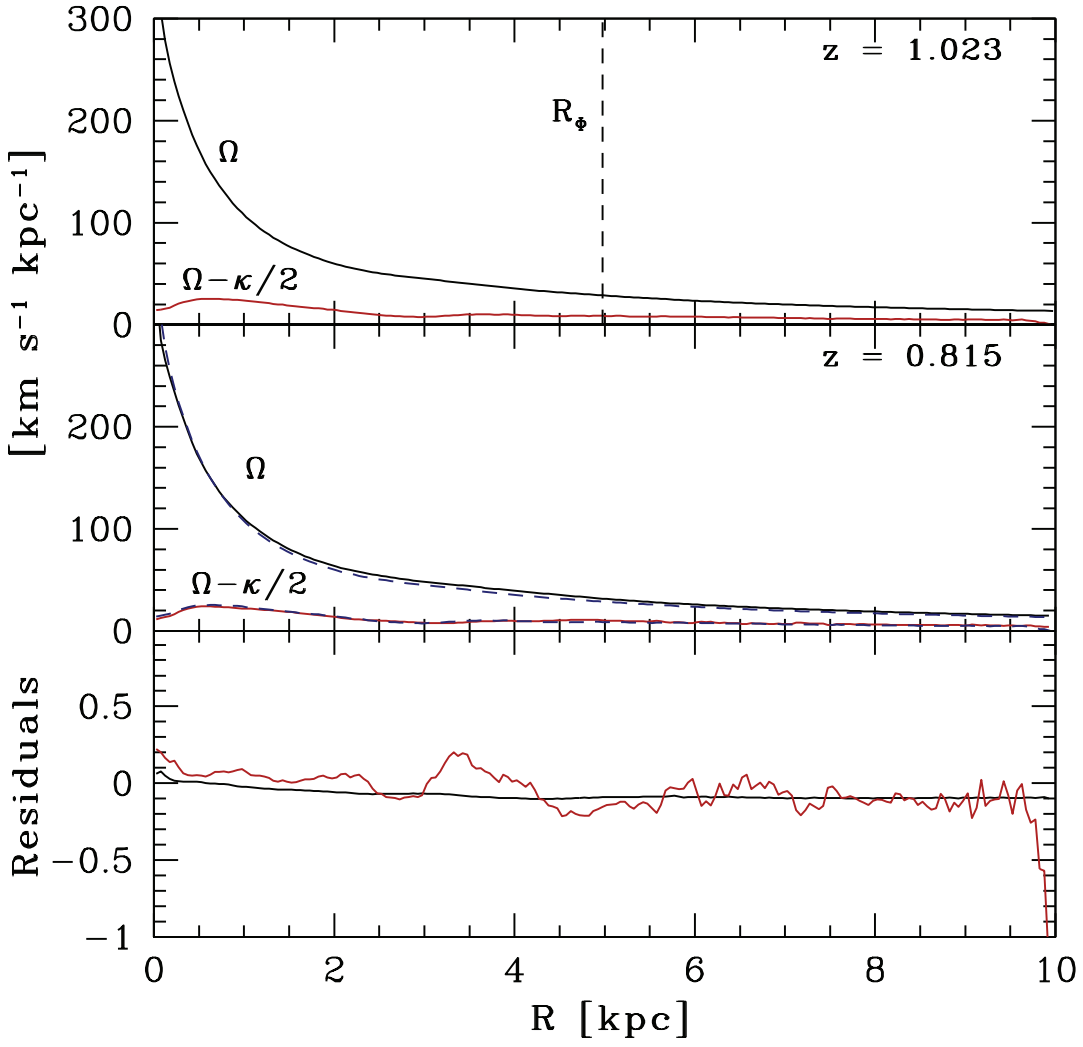

Figure 6.3: Frequency plot for the main galaxy. Upper panel: angular frequency Ω (solid black curve) and precession frequency $\Omega - \kappa/2$ (solid red curve) at $z_1 = 1.023$, before the satellite's pericentric passage (see the upper left panel of Figure 6.2). The vertical, dashed black line marks the length R_Φ of the bar at that time. Middle panel: angular frequency Ω (solid black curve) and precession frequency $\Omega - \kappa/2$ (solid red curve) at $z_2 = 0.815$, after the satellite's pericentric passage (see the lower left panel of Figure 6.2). For an easier comparison, the Ω and $\Omega - \kappa/2$ values evaluated at z_1 are also shown (dashed blue curves). Lower panel: relative variations of Ω (black curve), defined as $[\Omega(z_1) - \Omega(z_2)]/\Omega(z_1)$, and of $\Omega - \kappa/2$ (using the same definition; red line).

6.1.1 Comparison with previous works

This work strengthen the results of previous analysis performed on isolated simulations as discussed in § 3.4.2. Gerin, Combes, and Athanassoula (1990) studied the variation in bar strength and rotational speed due to external gravitational perturbations and concluded that the general effect of the perturbation could be summarised with the sign of the angle ψ between the bar and the perturber at the moment of its pericentre (see Equation 3.7). In Eris2k, it is hard to evaluate the precise moment of the pericentre, given the temporal resolution of about 33 Myr (the cosmological nature of the simulation prevented a more frequent sampling of the galactic evolution). In the snapshot with the shortest distance between the perturber and the centre of mass of the main system (the one adopted to compute $R_{\rm peri}$), $\psi = 82°$, which is very close to the neutral angle of $\pm 90°$, leaving a considerable uncertainity on the interpretation of the interaction. On the other hand, in the snapshots immediately before and after, the angles are equal to $\psi = -54°$ and $\psi = -79°$, respectively, and these results are compatible with the conclusion of Gerin, Combes, and Athanassoula (1990). Moreover, the results are not in disagreement with a slight increase of the bar angular velocity (see the last panel of Figure 7.3), but the trend is not obvious at all, as the variation is small and I do not have a reference simulation of the galaxy evolving in isolation in order to evaluate the phase difference (as performed in Gerin, Combes, and Athanassoula, 1990). However, whereas the pericentre in my case is similar to the values they investigated (from 5, to 17 kpc), the mass ratios $M_{\rm sat}/M_{\rm gal}$ they used (0.5 and 1) are far greater than mine (7×10^{-4}).
It follows that, in Eris2k, the perturbation is minimal with respect to those studied in Gerin, Combes, and Athanassoula (1990), but I found that this is sufficient to lower the bar strength parameter (see Figure 6.1) by about 70 per cent of its own value before the satellite pericentre.

It is also interesting to discuss how the statistical study of Peschken and Łokas (2018) on the barred systems in the Illustris-1 simulation is related to my work. In order to provide a quantitative comparison, I compute the angle β between the plane of the orbit of the satellite galaxy and the disc of the main system, along with the Elmegreen tidal strength parameter S through Equation 3.8. The perturbation in Eris2k run is very weak, given the really small mass ratio, yielding $S = 4.8 \times 10^{-3}$. In close proximity of the pericentre, the orbit is almost completely coplanar with the primary galaxy disc, with $\cos(\beta) = 0.96$. These values are in agreement with what the authors found in the Illustris run, confirming the scenario of small perturbations that work against the bar growth, independent of their orbital angular momentum.

6.2 Conclusions

I investigated the effect of the interactions between a growing disc galaxy and its satellites in the cosmological zoom-in simulation Eris2k, focussing on the impact that these interactions have on the persistence of the bar in the main galaxy. I identified the main interaction after the bar appearance as an

unequal-mass satellite ($q_* \simeq 4.5 \times 10^{-3}$) which undergoes a close pericentric passage ($R_{\rm peri} \simeq 6.5$ kpc, of the order of the bar length).

The perturbation shuffles the orbits of the stars which make up the bar, weakening and shortening the bar for about 900 Myr. The bar then reforms with strength and length comparable to those before the interaction. The reason for such bar resilience is due to the fact that the profile of the gravitational potential of the main galaxy and, as a consequence, that of its orbital and precession frequencies are not significantly affected by the perturbation.

This study thus provides a further indication that close unequal-mass encounters (most common during the cosmological evolution of structures) have a small impact on the internal evolution of field disc galaxies, where bars form spontaneously from small seed deviations from axisymmetry (see chapter 5).

However, due to the non-negligible duration of the bar-less period, a fraction of observed spiral galaxies classified as non-barred or weakly barred could be prone to bar formation. These galaxies could have hosted a strong bar in the (recent) past and currently be undergoing a bar-regrowth phase after a close flyby. I further speculate that, during such phase, a weak deviation from axisymmetry, in the form of lenses/ovals could be observed[8] and misinterpreted, for instance, as the sign of a "bar suicide" (see § 3.4.1.2 and references therein), if no analysis of the host potential is performed. The frequency of close flyby occurrences and their relative impact in the fraction of lensed/ansaed spirals cannot be assessed with a single cosmological zoom-in simulation. Moreover, the bulge-to-disc ratio, as measured through the stellar surface density fitting, decreases when the bar is suppressed, similarly to what has been observed during mergers in Guedes et al. (2013).

Due to the very unequal-mass ratio of the encounter, the disc potential remained basically unperturbed by the satellite passage (this is clearly shown in Figure 6.3). As a consequence, the current case does not result in the definitive disintegration of the non-axisymmetric structure. The cause for the "apparent death" of the bar in Eris2k is a minor and temporary energy exchange induced by the close tidal interaction (see also § 3.4.2.1). Even a small amount of energy is sufficient to azimuthally perturb the orbits in an almost-axisymmetric disc potential and, for this reason, the general effect of the flyby in the upper right panel of Figure 6.2 is to undermine the coherence of the orbits which contribute to the body of the bar, blurring its structural integrity. Once the perturbation has ceased, the self-gravity of the bar relic resumes the bar overdensity by slowly dissipating the energy of the encounter. Therefore, the bar is restored, but initially it appears to be puffier and less defined, as shown in the lower left panel of Figure 6.2.

An analogous fate has been observed in the previous chapter. Depending on the development stage of the bar, either its growth can appear delayed, as in chapter 5, or its whole structure can be destroyed (if the bar is fully grown and established) for a limited period, as shown in this work. The recurrent

[8] A central oval/lens is observable in the lower-left panel of Figure 6.2, but I caution the reader that a more detailed analysis (including the modelling of mock images) is needed to prove the actual observability of this morphological structure.

weakening of the bar due to encounters with satellites could be more important, and eventually critical, at higher redshift, as the interaction rate is supposed to increase.

Chapter 7

The importance of feedback

The study of the properties of the bar and of its complex interplay with the host system is a key factor in modern galaxy evolution theories. When N-body techniques were first applied to stellar dynamical problems, many significant steps forward were taken on the way to investigating the formation and growth of non-axisymmetries.

In the following chapter, I analyse and describe the outcome of the two simulations ErisBH and Eris2k which mainly differ in the prescriptions employed for gas cooling, star formation, and feedback from supernovae and black holes, as detailed in § 4.2.3. The enhanced stellar feedback in Eris2k, due to the collective effect of the different micro-physics implementations, results in a galaxy which is less massive than its ErisBH counterpart till $z \sim 1$. However, when the stellar content is large enough so that global dynamical instabilities can be triggered, the galaxy in Eris2k develops a stronger and more extended bar with respect to ErisBH. In particular, I detail the global-scale differences between the main galaxies, forming in the two above-mentioned cosmological runs (§ 7.1), the formation and growth of their bars (§ 7.2), and the following deaths of the same sub-structures (§ 7.3). § 7.4 presents a dynamical analysis that links the observed differences to the different stellar-physics and sub-resolution prescriptions. Finally, I present my conclusions in § 7.5.

I demonstrate that the structural properties and time evolution of the two bars are very different and strictly connected to the unresolved physics implemented. The results highlight the importance of accurate sub-grid prescriptions in cosmological zoom-in simulations of the process of galaxy formation and evolution, and the possible use of a statistical sample of barred galaxies to assess the strength of the feedback mechanisms.

The results described in this chapter are about to be published (Zana et al., 2018b).

7.1 Feedback effects on global scales: galaxy growth histories

As discussed in § 4.2.3, ErisBH and Eris2k share the same cosmological initial conditions and, as a consequence, are hosted in extremely similar large-scale DM haloes. Only the central regions of these DM haloes differ one from the other because of the unequal evolution of the baryons that dominate the central dynamics (see the two lowermost panels in Figure 7.1). This is mostly due to the different implementations of the IMF in the two runs, which result in a considerable disparity in the energy input into the interstellar medium via SN feedback. Indeed, the specific SN feedback energy input in new stars is 3.9×10^{48} and 1.0×10^{49}erg $\mathrm{M}_{\odot}^{-1}$ in ErisBH and Eris2k, respectively[1] (i.e. the SN energy per unit mass is more than 2.5 times higher in the Eris2k run). Concurrently, the difference in the SF thresholds used in the two simulations produces only a second-order effect. The minimum density n_{SF} has the greatest impact on the timing of SF, rather than on the resulting total mass of formed stars. From a collapsing gas cloud of sufficient mass, a higher SF threshold would be still reached, though later in time. Indeed, some recent works showed that the total stellar mass is only minimally affected by the variation of n_{SF} (see, e.g. Lupi, Volonteri, and Silk, 2017).

The enhanced effective feedback in Eris2k (see § 4.2.3) results in a larger fraction of the gas being preserved from forming stars, and thus, in a delayed stellar mass growth, as shown in the two uppermost panels of Figure 7.1. The steady increase of stellar mass produces, in turn, an increment of the DM component within the inner 20 kpc (of about 10^{10} $\mathrm{M}_{\odot}$ with respect to ErisBH), caused by the consequent adiabatic contraction (e.g. Blumenthal et al., 1986).

Interestingly, the radial extent of the galaxies is less sensitive to the different amount of SN feedback.

Due to the large (and varying) number of components needed to accurately fit Σ_* in the two runs, and the uncertainty associated to the fitting of an inherently elongated structure (the bar) with an axisymmetric component, it is preferable not to estimate the disc extent directly from the scale length of the fitted disc component (see Figures 4.2 and A.1 for two examples of such decomposition). I decided instead to compute the Kron (1980) radius R_{K}, i.e. a mass-averaged radius of the galaxy:[2]

$$R_{\mathrm{K}}(R) = \frac{\int_0^R \Sigma(x) x^2 dx}{\int_0^R \Sigma(x) x dx}, \tag{7.1}$$

evaluated at the radius R where $\mathrm{d}R_{\mathrm{K}}/\mathrm{d}R < 0.03$.[3]

[1] The quantities are calculated by integrating the high-mass tail of each IMF from 8 to 40 $\mathrm{M}_{\odot}$ and considering the related efficiency ϵ_{SN}.

[2] Note that the original formulation of the Kron radius weighs the radii using the stellar surface brightness, whereas here the focus is on the actual mass distribution. The two approaches are equivalent under the assumption of a R-independent mass-to-light ratio.

[3] Such definition is needed to prevent the contamination by stars not associated to the main

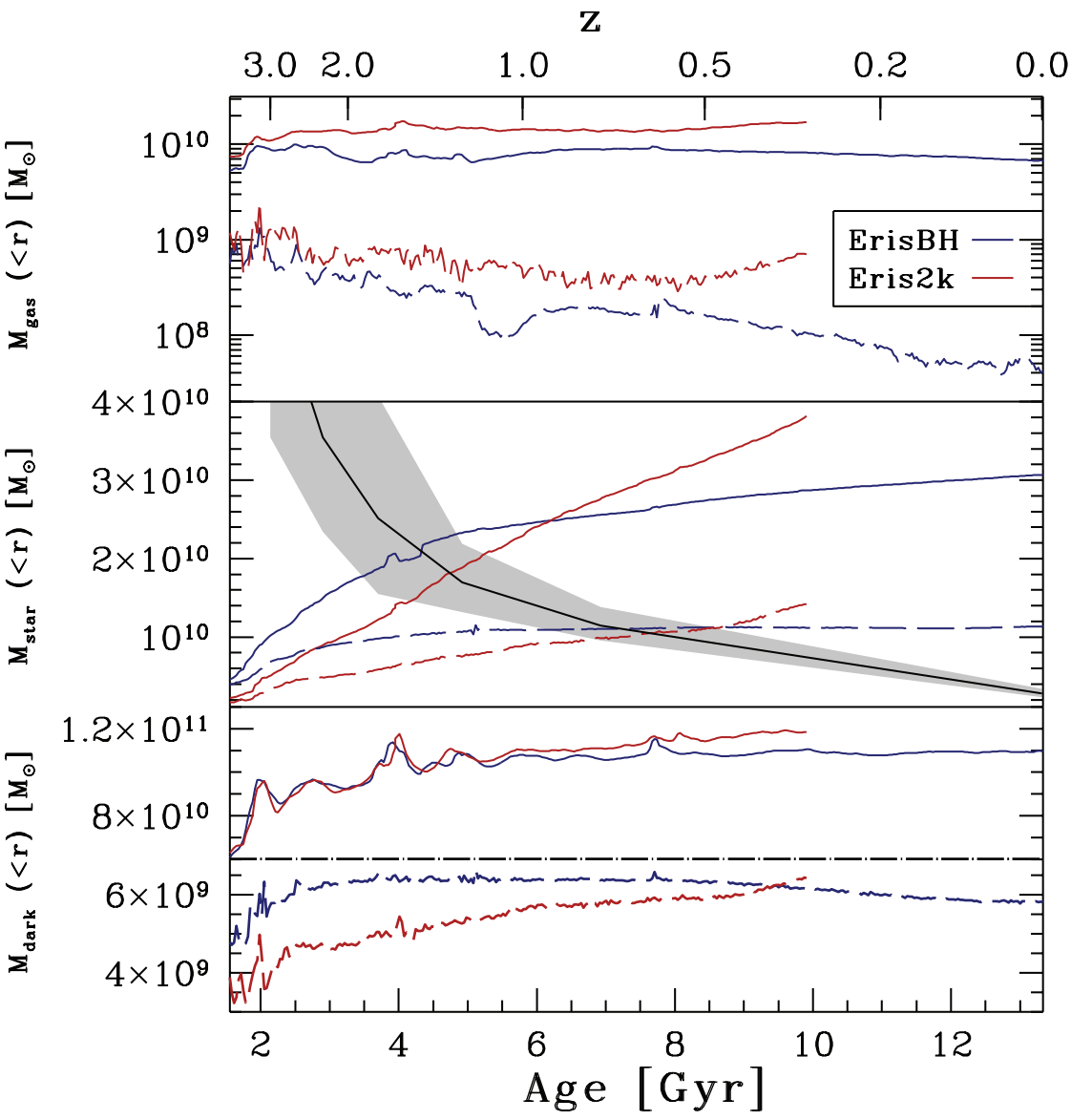

Figure 7.1: From top to bottom: Gas (first panel), stellar (second panel), and DM (third and fourth panels) masses enclosed within spheres of 20 (solid lines) and 2 (dashed lines) kpc radii. The blue lines refer to the ErisBH run, whereas the red lines to Eris2k. The galaxy in the Eris2k simulation, from $z = 3$, till the end of the run, approximately quadruples its stellar mass within both the analysed spheres, whereas the evolution is more modest in the ErisBH case. The peak in DM mass within 20 kpc at $z \sim 1.5$ in both runs corresponds to the close interaction with a satellite. The black solid line in the second panel refers to the knee mass in the relation between specific SF rate and stellar mass in Gavazzi et al. (2015; the errors are indicated by the shaded area), who proposed it as a threshold for the growth of stellar bars (see the discussion in § 7.5).

The Kron radius grows during the evolution of the discs from about 1 to about 4 kpc in both the runs and, at each redshift, the difference between the two $R_{\rm K}$ remains within $\sim$10 per cent of each other. On the other hand, the stellar mass of the two galaxies (both within 2 and 20 kpc) can differ by almost a factor of two. This hints to a far smaller effect of the different stellar-physics prescriptions over the disc extent, compared to other fundamental properties, such as the stellar mass. A comparison between the two runs at different times is presented in Figure 7.2. It is worth emphasizing here a fundamental difference between the studies of idealized isolated disc galaxies and cosmological studies: whereas in the former case the galaxies evolve for up to ~ 10 Gyr (e.g. Athanassoula, Machado, and Rodionov, 2013) as if they formed from a monolithic collapse at the dawn of times, here each galaxy undergoes a significant evolution in mass and size, even during the last evolutionary stages when a growing bar is present. This gives us the unique opportunity to link the evolution of sub-structures, in particular the bars, to the cosmological growth history of the galaxies.

7.2 Feedback effects on sub-structures: the different lives of bars

In order to quantify the formation epochs, strengths, lengths, and angular speeds of the bars forming in the two simulated galaxies, I perform a Fourier decomposition of the face-on view of the stellar surface density Σ_* as explained in § 3.2. More specifically, I compute the local strength of any bar-like deviations from axisymmetry through the the quadrupole-to-monopole ratio of Equation 3.1.

Analogously to what done in chapter 5 and 6, I provide both the value of the differential $A_2(R)$ profile (considering only the particles in each annulus built around the radius R, and the cumulative $A_2(<R)$ profile (extending the summation over every particles from the centre of the system to R). The disc within 12 kpc is divided in 1000 linearly spaced cylindrical annuli of height 2 kpc. The maxima of the two profiles – $A_{2,\rm max}(R)$ and $A_{2,\rm max}(<R)$ – are the estimates of the bar strength, and their evolution with time is shown in the two uppermost panels of Figure 7.3.

The sizes of the growing bars and their angular speeds are obtained through the radial profile of the angular phase of any two-fold asymmetry, given by Equation 3.2.

Wherever a bar-like structure (i.e. a straight $m = 2$ mode) is present, the profile of $\Phi(R)$ shows a plateau (see, for instance, the middle row of Figure 7.4). As described in § 3.2.2, the length R_Φ of such asymmetry, whose evolution is shown in the third panel of Figure 7.3, has been estimated by checking for the extent of such plateau. Operatively, R_Φ is defined as the radius at which $\Phi(R)$

galaxy.

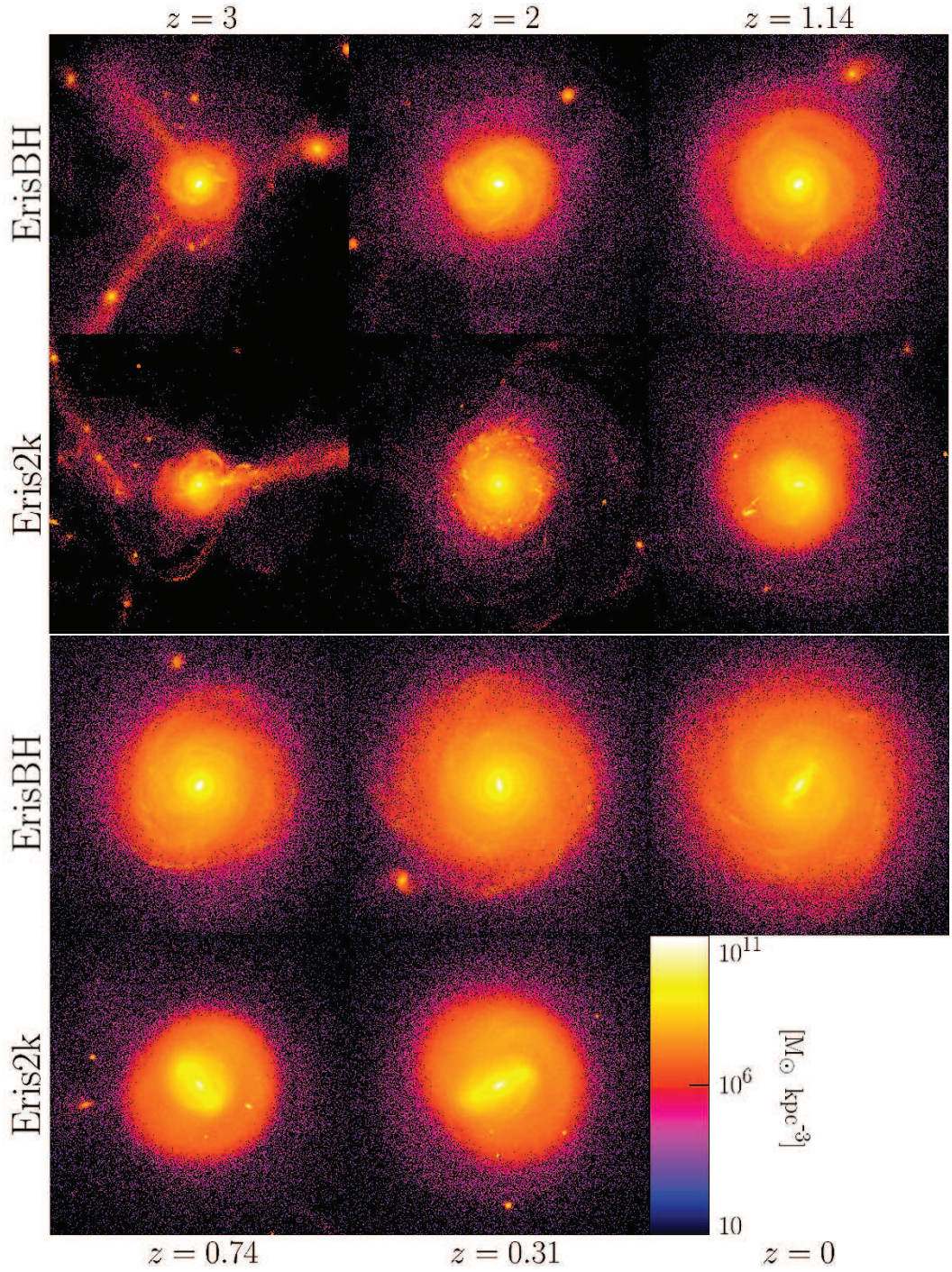

Figure 7.2: Comparison between the stellar density maps of the main galaxies in ErisBH (first and third rows) and Eris2k (second and fourth rows) simulations. The boxes measure 40 kpc per side and have a fixed logarithmic colour scale, ranging from 10 to 10^{11} $\mathrm{M_\odot kpc^{-3}}$. In the first block on top (six panels), I show, from left to right, the systems at $z = 3$, 2, and 1.14, which is when the bar starts growing in Eris2k (see § 7.4). In the lower block (five panels), the redshift are $z = 0.74$ (the ErisBH bar formation time), 0.31 (the last snapshot of Eris2k), and 0, which is present only for the ErisBH simulation, since the Eris2k run has been halted at $z \approx 0.3$. In order to better appreciate the growing bars, Figures 7.5 and 7.6 provide the three projections of the central 12 kpc of the disc at the time of bar formation and at the end of the two simulations, respectively.

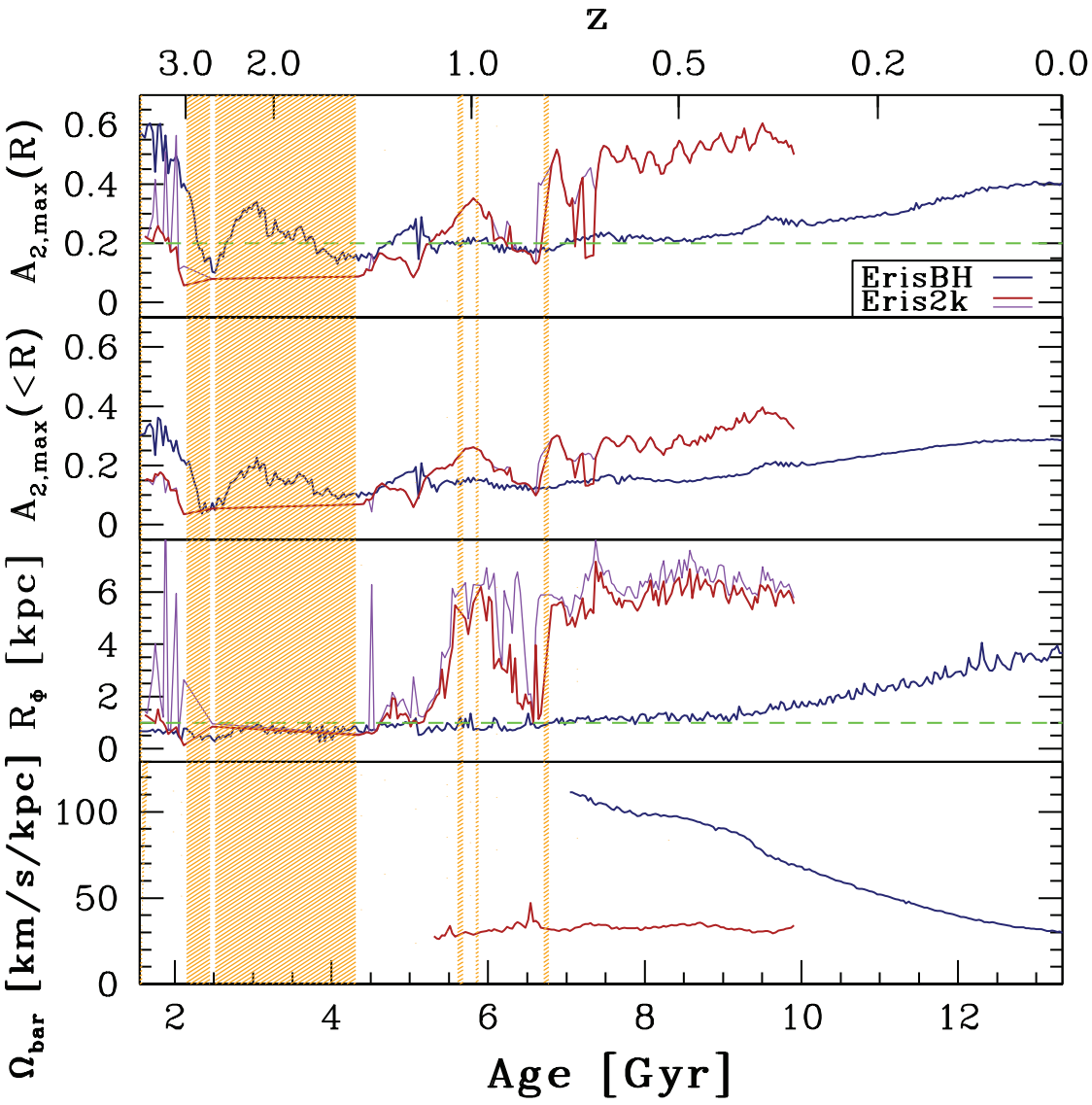

Figure 7.3: Redshift evolution of the bar properties. From top to bottom: maximum strength of the two-fold deviation from axisymmetry measured in thin radial annuli (first panel) and averaged within any given radius R (second panel); radial extent of such deviation (third panel), and its corresponding angular frequency (fourth panel). The shaded areas mark the redshift ranges where it was impossible to retrieve the bar properties for the galaxy in Eris2k. The purple lines show the Eris2k values for the overdensities marked as bars when $|\Phi(R_{\rm peak}) - \Phi(R)| < \Delta\Phi = \arcsin(0.3)$, as opposed to $\Delta\Phi = \arcsin(0.15)$ in all other cases.

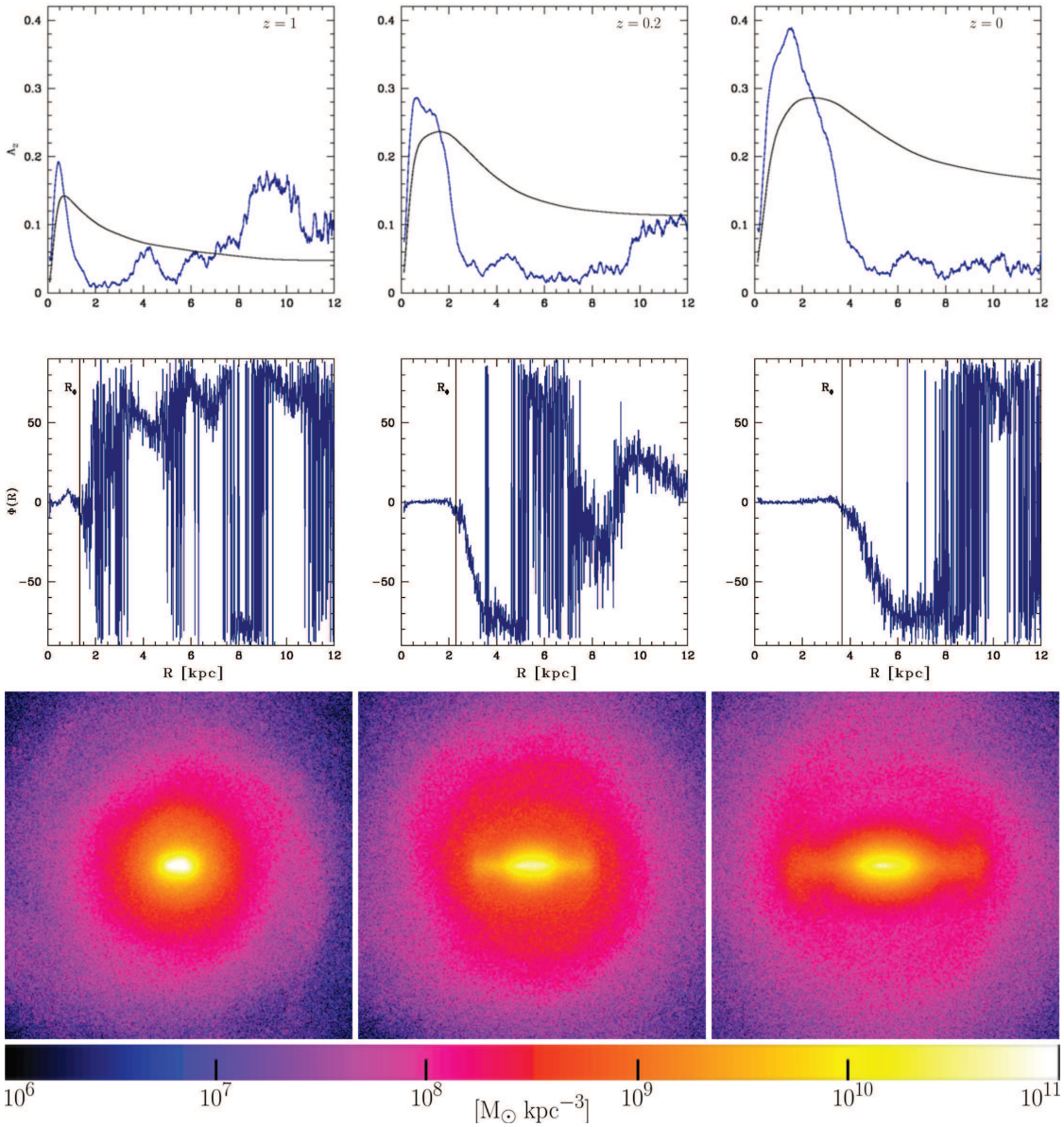

Figure 7.4: Three snapshot of ErisBH, with increasing time from left to right. The evolution of the $A_2(R)$ profile (blue lines) is shown along with its cumulative counterpart $A_2(< R)$ (black lines) in the uppermost row, whereas the profiles of the phase $\Phi(R)$ (blue lines) are shown in the middle row as they are computed through Equation (3.2). The black vertical lines mark the positions of the bar length estimator R_Φ. As the redshift approaches $z = 0$, the peaks of both the A_2 functions become higher (the bar gains in strength) and move farther out (the bar gains in length). At the same time, the plateau in $\Phi(R)$ becomes longer. The growth of the structure is echoed in the corresponding stellar density maps (lowermost row). The logarithmic colour scale ranges from 10^6 (black) to 10^{11} $\mathrm{M}_\odot\ \mathrm{kpc}^{-3}$ (white) and the side of each panel measures only 12 kpc, in order to focus on the bar region.

deviates from $\Phi(R_{\rm peak})$ by more than $\arcsin(0.15)$, where $R_{\rm peak}$[4] is the radius corresponding to $A_{2,\rm max}(<R)$.

Figure 7.4 exemplifies how the Fourier decomposition method allows to follow the growing non-axisymmetries of this analysis, showing, for three ErisBH snapshots of decreasing redshift (from left to right), both the $A_2(R)$ (blue lines) and the $A_2(<R)$ (black lines) profiles (uppermost row), the phase profile $\Phi(R)$ (middle row) and the corresponding stellar density maps (lowermost row). The longer and clearer the barred overdensity becomes, the higher the peaks in both the profiles of A_2 are and their positions move toward larger radii. A clear evolution is also visible in the progressive straightening of the phase, which, in turn, results in a gradual increase of the length R_Φ (black vertical lines in the middle row).

Whereas the procedure to identify the bar is applied without restrictions on the ErisBH run, the bar in the Eris2k simulation appears less defined and the related surface density profiles are, in general, more noisy. As a consequence, the associated analysis requires some additional steps, which are detailed in Appendix B.

The sudden drops of the red lines of Figure 7.3, like the one at ∼7 Gyr, are signs of the "clumpiness" of the Eris2k surface density map (see Figure 7.2). Some of them are absent in the purple lines, which provide an alternative estimate for the quantities $A_{2,\rm max}(R)$, $A_{2,\rm max}(<R)$, and R_Φ, using $|\Phi(R_{\rm peak})-\Phi(R)|<\arcsin(0.3)$, instead of $\arcsin(0.15)$. Even if the differences between the two estimates are minimal, it is clear that the drops are just numerical and can be removed, e.g. by increasing the maximum variation $\Delta\Phi$ allowed to $\Phi(R)$. Unfortunately, this comes at the price of losing accuracy in the determination of R_Φ, hence I maintain $\Delta\Phi=\arcsin(0.15)$ as preferred criterion.

Whenever a bar is present, its angular speed $\Omega_{\rm bar}$ (lowest panel of Figure 7.3) is computed using the values of $\Phi_{\rm bar}$ [obtained by averaging $\Phi(R)$ over the annuli that are part of the bar] between consecutive snapshots.

In order to avoid possible effects due to the sub-optimal resolution or to misinterpret transient deviations from axisymmetry (caused, for instance, by a self-gravitating object not originated from the disc), I impose very conservative requirements for the detection of a *strong* bar in the analysed runs. In particular a strong bar is identified when

1. $A_{2,\rm max}(R)>0.2$;
2. $R_\Phi>1$ kpc (about 10 softening lengths for $z<9$).

These criteria result in a bar formation epoch of $z\approx1.14$ for Eris2k and $z\approx0.74$ for ErisBH[5] (the conditions are also briefly met at $z\sim1.2$, but this is due to the last minor merger; see chapter 5). Figure 7.5 shows the stellar

[4] Differently from § 3.2.2, the name $R_{\rm peak}$ is used here instead of $R_{\rm max}$, because the $A_{2,\rm max}(<R)$ profile shows often more than one peak.

[5] A small (barely resolved) non-axisymmetric structure can be detected even at higher redshift, especially in the case of ErisBH; see also Guedes et al. (2013) for a similar result in the case of the Eris simulation.

density maps of both the galaxies at the epoch of bar formation, according to our constraints. In the central regions of both galaxies the origins of two elongated overdensities are recognizable, especially in face-on viewed maps (left-hand panels). The evolutions in strength, length, and speed of the two forming bars are remarkably different. Eris2k has a significantly faster growth, with the bar length reaching a close to constant value in less than 1 Gyr. The sudden drop in the strength and length of the bar at $z \approx 0.95$–0.8 has been studied in chapter 6, and is caused by the temporary shuffling of the orbits of the stars building the bar, due to the close passage (pericentric distance of ~ 6.5 kpc) of a small satellite ($M_{\rm sat} \approx 1.1 \times 10^8$ M$_\odot$). As discussed in § 6.1, the satellite passage does not modify substantially the primary potential profile nor, as a consequence, $\Omega_{\rm bar}$, and the bar regains its pre-interaction properties within ≈ 900 Myr. Only close to the end of the run (age > 9 Gyr in Figure 7.3), the Eris2k bar starts to weaken and shorten, due to a bar-driven strong inflow of gas as in the bar-suicide scenario (see § 7.3).

The ErisBH bar, on the other hand, shows a later start and a slower evolution, with strength and length gradually increasing till $z \sim 0$, when the growth in $A_2(R)$ and $A_2(< R)$ slows down due to the vertical instabilities and the consequent buckling of the bar (see § 7.3).[6] $\Omega_{\rm bar}$ shows a slow and approximately constant decrease, as commonly found in isolated systems (see § 3.4.1).

7.3 Feedback effects on sub-structures: the different deaths of bars

The weakening and shortening of the Eris2k bar at $z \lesssim 0.4$ is related to the strong bar-driven gas inflow within the central 400 pc observable in the middle panel of Figure 7.7. It must be noted that, at higher redshift, the mass of the galactic nucleus in Eris2k remains significantly lower than in ErisBH, due to the same higher impact of SN feedback that delays the overall growth of the galaxy with respect to its ErisBH counterpart. Only when the galaxy potential well is deep enough and the bar is already fully developed, the gas flowing toward the central regions of the galaxy can efficiently form a central stellar knot. This gas transfer leads to the so-called bar-suicide process (see § 3.4.1.2 and references therein), which is when the fast differential precession at different radii unravels the stars in the inner regions of the bar, decreasing its strength.

The effect of such a dense stellar nucleus is clearly observable in the radial profile of the precession frequency $\Omega(R) - \kappa(R)/2$ of a test particle on (little-)eccentric orbits in the disc plane (see § 3.3). As discussed in chapter 6, $\Omega(R) - \kappa(R)/2$ is strongly sensitive to any central mass concentration and has been already used to put constraints on the central MBH mass of a disc galaxy, even when the black hole influence radius was poorly resolved (Combes et al., 2014).

[6] The difference between $A_2(R)$ and $A_2(< R)$ is hardly noticeable in Eris2k, whereas it is clearer in the ErisBH run. This is due to the different mass concentrations in the stellar-dominated galactic nuclei: the stellar mass within 400 pc is up to three times larger in the ErisBH case (see § 7.3), affecting the monopole term of the Fourier development.

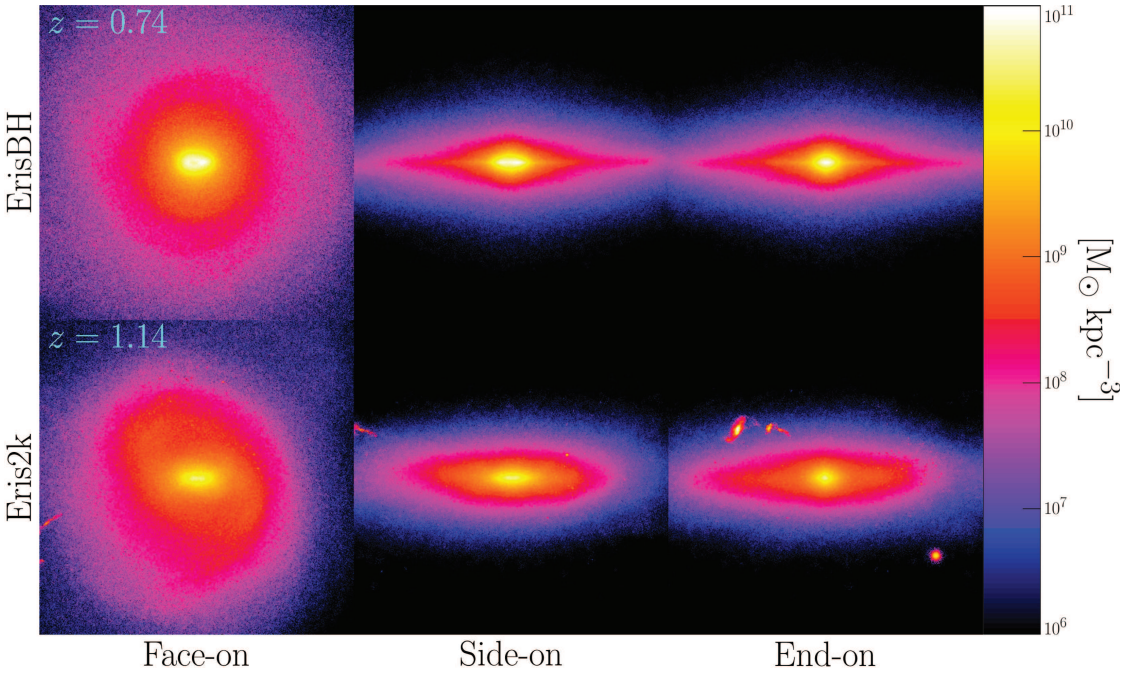

Figure 7.5: From left to right: face-on, side-on, and end-on projections of the central region (12 kpc per side) for both the simulations ErisBH (top row) and Eris2k (bottom row) at the time of formation of their bar, according to the criteria discussed in the text. The logarithmic colour scale ranges from 10^6 (black) to 10^{11} $\mathrm{M}_\odot\ \mathrm{kpc}^{-3}$ (white). The bars are barely discernible in these snapshots, but they soon increase their strength and length, following the evolution examined in § 7.2, to culminate in the fully grown structures visible in Figure 7.6.

The profiles of $\Omega(R)$ and $\Omega(R) - \kappa(R)/2$ are shown in Figure 7.8 for the last snapshot of the two runs. Eris2k shows a central cusp in $\Omega(R) - \kappa(R)/2$, that drops only at radii comparable to the gravitational force resolution. Such peak is not present before the above-mentioned gas inflow, and, as a consequence, no inner ILR was found until $z = 0.43$, as shown in the bottom panel of Figure 7.7.[7]

The precession frequency profile is considerably different in the ErisBH case, where the increase of $\Omega(R) - \kappa(R)/2$ toward the centre starts earlier in time and at larger radii, due to the large mass concentration already present at high redshift, but does not keep growing to the smallest resolved scales, probably due to the MBH feedback implemented in this run.[8]

[7] The combined mass of the newly formed stars (of about 3.7×10^7 $\mathrm{M}_\odot$ within 0.2 kpc and 6.2×10^7 $\mathrm{M}_\odot$ within 0.4 kpc) after $z = 0.43$ is almost equal to the variation of the total stellar mass in the same regions and in the same period. It follows that the gaseous inflow is fully responsible for the increase in the central mass concentration.

[8] The influence radius of the MBH in ErisBH is far from being resolved. If it was resolved, $\Omega(R) - \kappa(R)/2$ would show a central divergence at pc scales and an ILR would always be present at such scales.

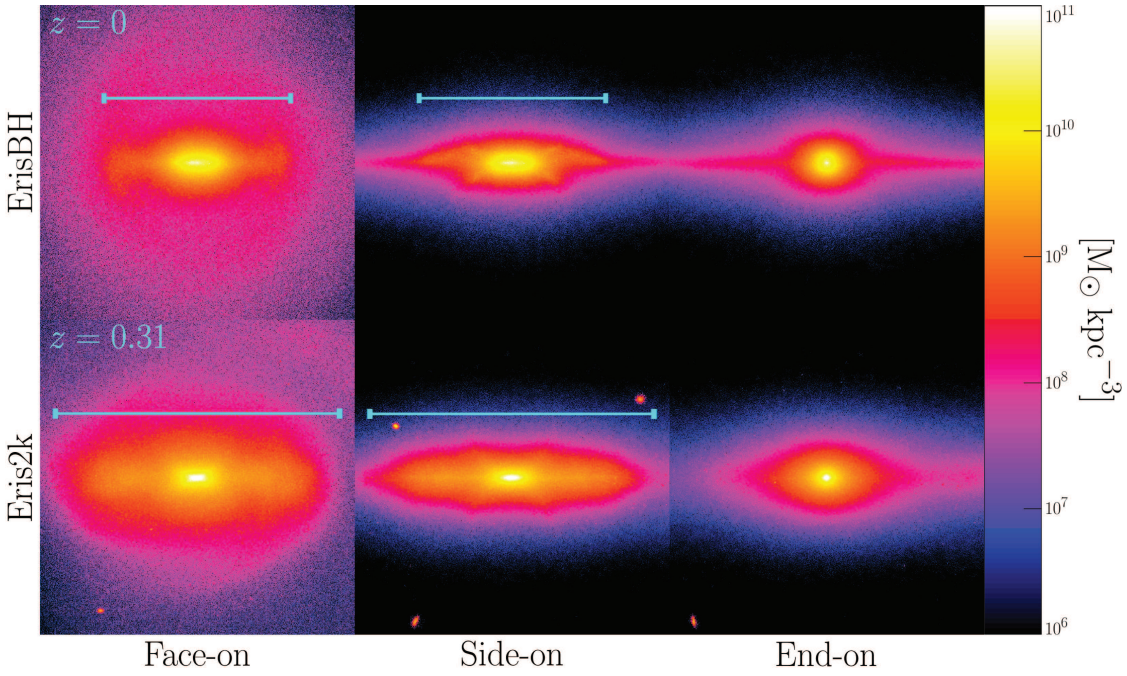

Figure 7.6: Same as Figure 7.5, but at the final snapshots of the two simulations. The colour scale and size are kept identical to those of Figure 7.5 in order to facilitate the comparison. At the represented times the bar (semi-)length R_Φ are 3.7 kpc in ErisBH and 5.5 kpc in Eris2k. The cyan rods correspond to twice R_Φ. The fully evolved structures almost fill the related panels, whereas the characteristic X-shaped pseudobulge is noticeable in the centre of both the galaxies as an index of the bar development stage. This is larger in the case of ErisBH, which also shows the signs of a progressive vertical asymmetry, completely missing in Eris2k (see § 7.3, for a discussion of this process).

As a consequence, the ILR in ErisBH appears only when the bar has slowed down enough to intersect the $\Omega(R) - \kappa(R)/2$ profile, as shown in the bottom panel of Figure 7.7.

The slowing down of the bar growth in ErisBH is not associated to any gas inflow, as demonstrated in Figures 7.7 (the stellar mass within 400 pc even shows a decrease at low redshift) and 7.8, but it is due to the buckling of the central regions of the bar, when the radial motions get partially converted into vertical motions above the disc plane, breaking the symmetry of the stellar distribution with respect to the disc plane and weakening the bar (see § 3.4.1.1 and references therein).

As originally suggested by Raha et al. (1991), the buckling is expected to occur when the ratio between the vertical and the radial velocity dispersion σ_z^2/σ_R^2 decreases below a given stability threshold. I follow Martinez-Valpuesta, Shlosman, and Heller (2006) by computing σ_z^2/σ_R^2 on the stars that are in the bar only, i.e. by selecting only particles within 2 kpc from the disc plane and within 2 kpc from the bar's major axis.

Isolated numerical models set the buckling-unstable threshold to $\sigma_z^2/\sigma_R^2 \approx 0.6$ (Sotnikova and Rodionov, 2005). The evolution of σ_z^2/σ_R^2 is presented for ErisBH

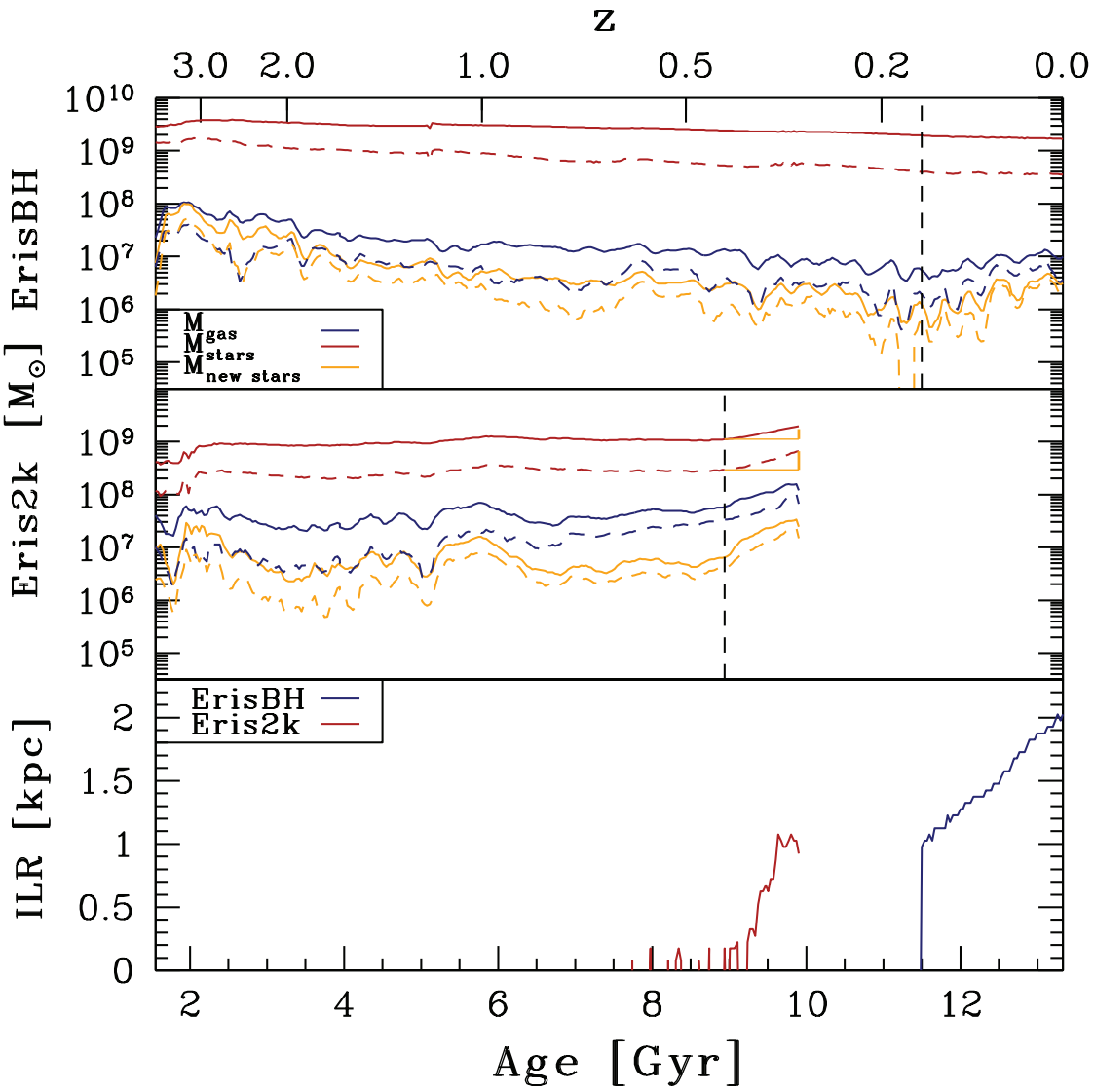

Figure 7.7: Upper two panels: comparison between the central stellar (red lines) and gas (blue lines) masses in ErisBH (first panel) and Eris2k (second panel). Yellow lines refer to newly formed stars only (i.e. stars formed within 33 Myr, in between two snapshots). Solid and dashed lines refer to the mass within 0.4 and 0.2 kpc, respectively. The time when the ILR starts to arise is marked with a vertical black dashed line (see the discussion in the main text). The mass in stars formed after $z = z_{\rm ILR}$ (yellow vertical segment in the figure) is a significant fraction of the final stellar mass in the nucleus at $z \approx 0.3$. Lower panel: evolution of the ILR radii for ErisBH (blue line) and Eris2k (red line).

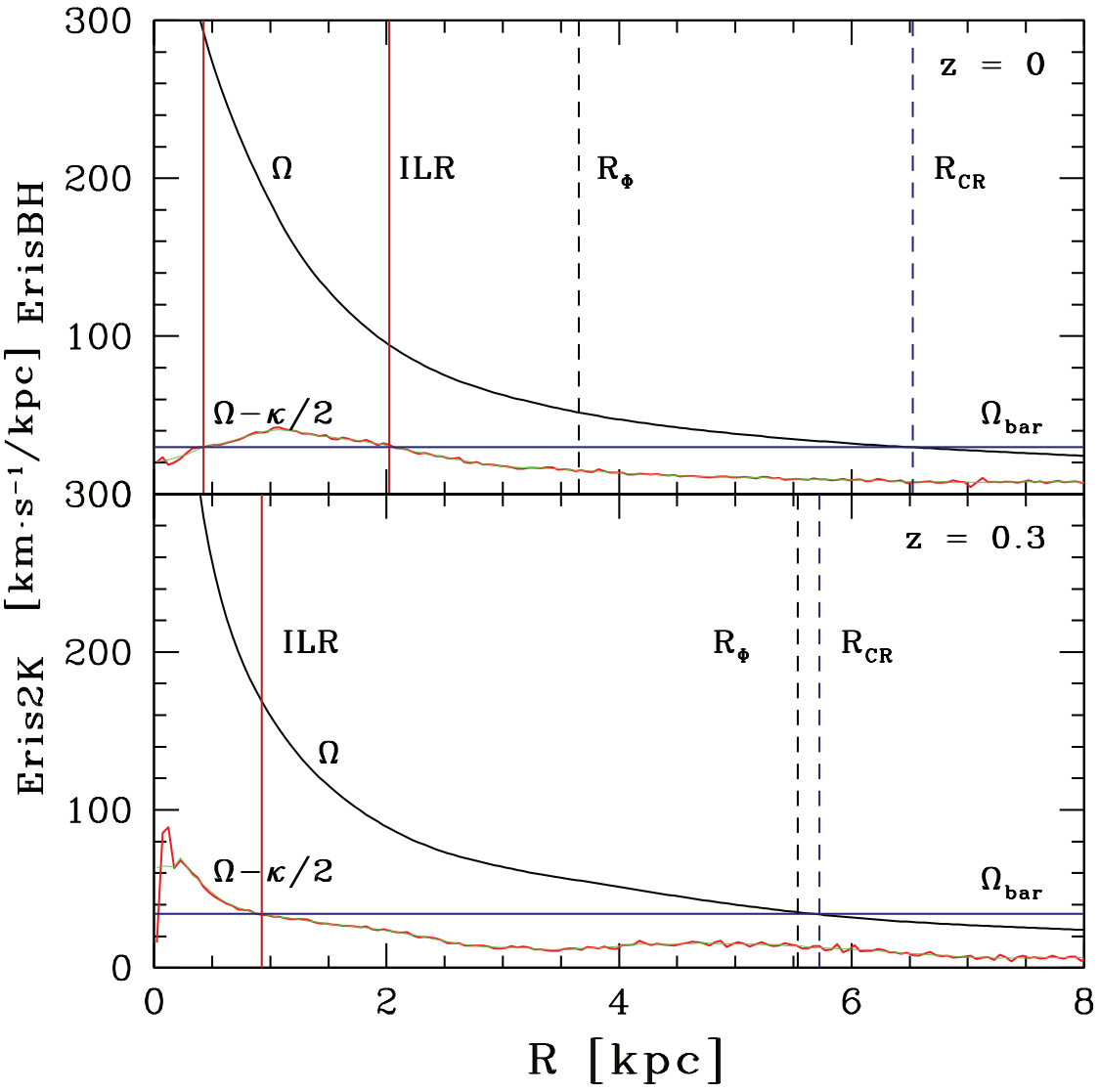

Figure 7.8: Frequency maps of the main galaxies in ErisBH (upper panel) and Eris2k (lower panel) at the end of the two runs. The black and red curves refer to the angular velocity $\Omega(R)$ and to the precession frequency $\Omega(R) - \kappa(R)/2$, respectively. The horizontal blue lines refer to the bar angular velocities $\Omega_{\rm bar}$. The green lines show a smoothing of the precession frequency curves that have been used to find the intersections with $\Omega_{\rm bar}$. The black dashed lines refer to the bar extent (R_Φ), whereas the other vertical lines highlight the positions of the corotation radii $R_{\rm CR}$ (blue dashed lines) and of the ILR (solid red lines; see § 2.4).

in the upper panel of Figure 7.9, showing a decreasing trend as a function of time down to the above-mentioned threshold at $z \approx 0.1$. Martinez-Valpuesta, Shlosman, and Heller (2006) performed a Fourier decomposition of the side-on stellar surface density[9] and selected the $m = 1$ (over the $m = 0$) mode as an estimate of the degree of buckling, according to

$$A_{1,z}(x < x_{\max}) \equiv \frac{\left|\sum_j m_j e^{i\phi_j}\right|}{\sum_j m_j}, \tag{7.2}$$

where the sum is performed only over the bar stars with the same geometrical limits adopted for the computation of σ_z^2/σ_R^2. The time evolution of $A_{1,z}$, estimated within $x_{\max} < 1$ kpc, $A_{1,z}(< 1\ \mathrm{kpc})$, is shown in the middle panel of Figure 7.9. A net increase in the buckling parameter is clearly observable as soon as the galaxy becomes buckling-unstable, due to the breaking of symmetry with respect to the disc plane. This bump corresponds to an increase in σ_z (hence in the σ_z^2/σ_R^2 parameter) observable in the upper panel at late times. The richness of small sub-structures of both cosmological and internal origin produces the fluctuations present in the evolution of $A_{1,z}(< 1\mathrm{kpc})$.

I therefore provide a new quantitative estimate for the degree of buckling: at any value of x, I first compute the height above and below the disc plane within which 90 per cent of the stellar mass is included [dubbed $z^+(x)$ and $z^-(x)$, respectively], applying again the same geometrical boundaries used to compute σ_z^2/σ_R^2 and $A_{1,z}$. I then quantify the buckling asymmetry by computing the x-averaged relative difference of the $z^+(x)$ and $z^-(x)$ profiles:

$$\delta = 2\frac{\int_{-8\,\mathrm{kpc}}^{8\,\mathrm{kpc}}(z^+(x) - |z^-(x)|)\mathrm{d}x}{\int_{-8\,\mathrm{kpc}}^{8\,\mathrm{kpc}}(z^+(x) + |z^-(x)|)\mathrm{d}x}. \tag{7.3}$$

The evolution of δ is shown in the bottom panel of Figure 7.9, where a clear prominent peak is observed at $z \lesssim 0.1$, in agreement with the other estimators. The buckled part of the disc does evolve close to the end of the run into a boxy/peanut bulge, decreasing the asymmetry as observable both in $A_{1,z}(< 1\mathrm{kpc})$ and δ, as already detailed for the ErisBH case in Spinoso et al. (2017) (see § 3.4.1.1).

[9] Here, the position on the bar major axis is indicated with x.

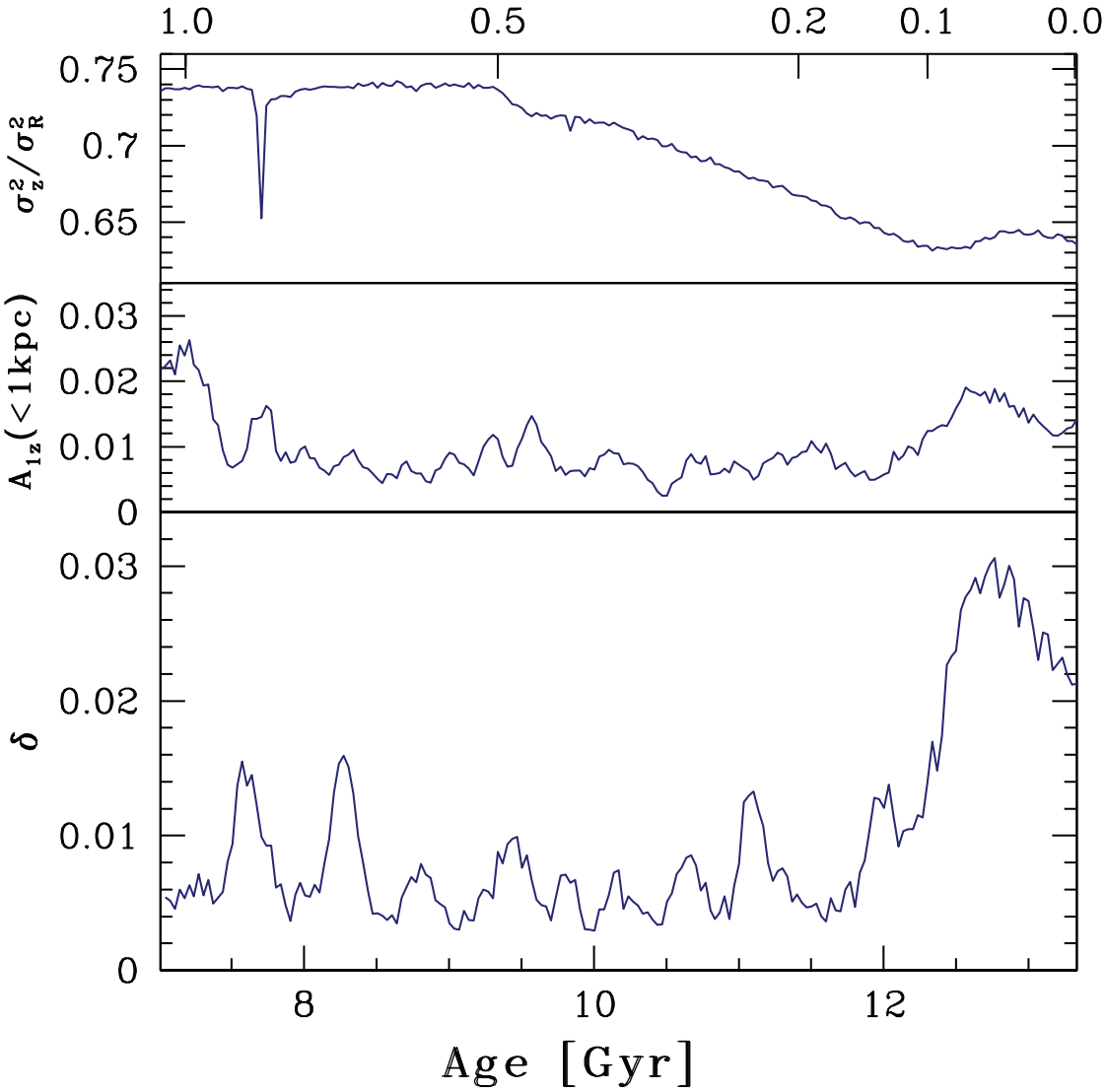

Figure 7.9: Evolution of the buckling-instability estimator σ_z^2/σ_R^2 (uppermost panel), of the $m = 1$ Fourier-based buckling-strength parameter $A_{1,z}(< 1\mathrm{kpc})$, and of the newly defined buckling-strength parameter δ, for the ErisBH run.

7.4 Dynamical interpretation of the different bar properties

In § 3.3, I described the role of the parameters Q (Equation 3.3) and X (Equation 3.4 on page 32) to determine the susceptibility of a stellar disc to develop a bar. Moreover, even if $\lambda_{\rm crit}$ from Equation 3.5 cannot directly measure the perturbation wavelength for a non-axisymmetric mode such as $m = 2$, it does provide an estimate of the scale size of the disc region that can become unstable to its own self-gravity.

As previously discussed, there are no precise values for Q and X to determine the onset of a non-axisymmetric instability. However, a common assumption (that I adopt in the following) is that spiral waves and bars can form for $1 < Q \lesssim 2$ and $X \lesssim 3$ (e.g. Toomre, 1964; Toomre, 1981).

To assess the conditions for bar formation in Eris2K and ErisBH, I estimate Q, X, and $\lambda_{\rm crit}$ as a function of R for different redshifts, from $z = 1.75$, when the bar is not formed yet, down to $z = 0.34$. The different quantities are reported in Figure 7.10 (ErisBH) and Figure 7.11 (Eris2K). Both Q and X depend directly on the galactic potential, hence on the stellar distribution within the galaxy. Differences in these parameters are directly associated to the different (both in time and space) SF histories in the two runs, as discussed in § 7.1 and § 7.2.

In ErisBH, Q (top panel) does not vary significantly over the redshift range considered, showing a shallow radial profile with $Q \gtrsim 2.5$ between $R = 1$ and $R = 4$ kpc. In Eris2K, on the other hand, Q monotonically decreases with redshift, settling around $Q \sim 1.5$ for $R < 4$ kpc and remains always lower than the ErisBH values.[10] Here, the flattening in the profile of Q occurs when the bar forms, with $Q \gtrsim 3$ only above $R \sim 5$ kpc, corresponding roughly to the extension of the bar (see Figure 7.3). Assuming a critical value $Q_{\rm crit} \sim 2$ for global instabilities to develop, the observed trends confirm indeed that the bar in Eris2K, at formation time, is already larger and stronger than that in ErisBH, which is limited to the central kpc only.

$\lambda_{\rm crit}$ (middle panels) and X (bottom panels), on the other hand, show a completely different evolution. As the galaxy evolves, $\lambda_{\rm crit}$ (X) in ErisBH exhibits a slow decrease (increase) that limits the maximum extension the bar could possibly reach during its evolution. In Eris2K, instead, both quantities remain (almost) constant, witnessing a negligible change of the bar properties.

A comparison of the two figures shows that the (slightly) later formation time and the initial extension of the bar in ErisBH can be easily explained in terms of Q and X, that are $\sim$ 1.5–2 times larger, for $R \lesssim$ 4–5 kpc, than in Eris2K, making the disc in the latter case prone to stronger instabilities able to trigger the formation of a stronger and more extended bar.

During the evolution of the bar, the stability parameter analysis remains consistent with the picture in Figure 7.3. In particular, the bar in ErisBH is initially small ($Q < 2$ only within the central kpc), and grows up to $R_\Phi \sim 4$ kpc by $z = 0$. The maximum extension in this case is limited by the decrease of

[10] The only exception in the evolutionary trend of Eris2K appears at $z \lesssim 0.4$, and is compatible with the bar weakening (see § 7.3).

$\lambda_{\rm crit}$, which peaks around 4 kpc at $z = 0.34$. The bar in Eris2k, on the contrary, is fully developed from its start, because of $Q \lesssim 2$ up to $R \sim 4$ kpc and $\lambda_{\rm crit}$ peaking around 6–7 kpc, but does not evolve significantly with redshift. The only exception is $z = 0.34$, when the bar starts to dissolve, and the disc becomes stable also at smaller scales (Q and X start to increase and $\lambda_{\rm crit}$ drops to less than 4 kpc).

It should be noted that Toomre's stability criterion (Equation 3.3), as well as the swing amplification criterion (Equation 3.4) are derived in the Wentzel–Kramers–Brillouin (WKB) approximation,[11] which is only reliable when $\lambda_{\rm crit}$ is short compared to the length of the system, or if $X > 1$. Although the previous discussion is only aimed at the comparison of the evolving properties of the two simulations, from Figures 7.10 and 7.11 it is clear that the WKB approximation is not satisfied for $R \lesssim 1$. The description of instability waves in these conditions would require a more advanced method in non-linear theory, which is beyond the scope of this work.

In § 3.3, I discussed the use of the ELN criterion in order to evaluate the disc responsiveness to non-axisymmetric instabilities. The ELN parameter $\epsilon_{\rm ELN}$ has been computed for both the simulations here stuidied, but does not add any information to the investigation of the bar formation process. However, the results are presented in Appendix C.

[11] In linear perturbation theory, the WKB approximation assumes that the long-range gravitational coupling is negligible with respect to local interactions, so that the response can be locally described (Binney and Tremaine, 2008).

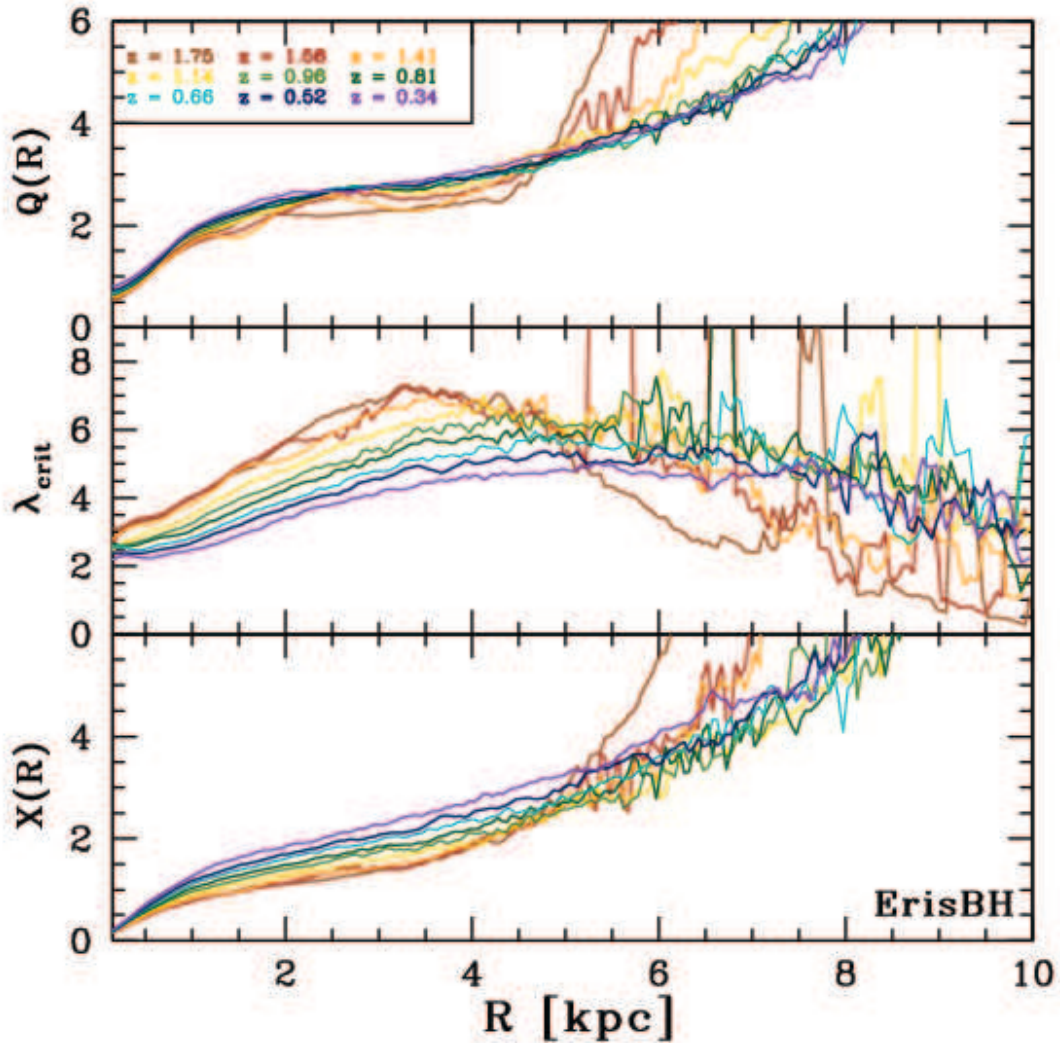

Figure 7.10: Stability parameters for ErisBH (from top to bottom): Toomre parameter Q, critical wavelength $\lambda_{\rm crit}$, and swing amplification parameter X. The profiles are evaluated from the centre of the galaxy till 10 kpc, over 1000 equally-spaced circular bins of height 8 kpc. The different colours refer to different cosmic times, as it is reported in the upper panel with the corresponding colour-code (from red to violet, the time is monotonically increasing).

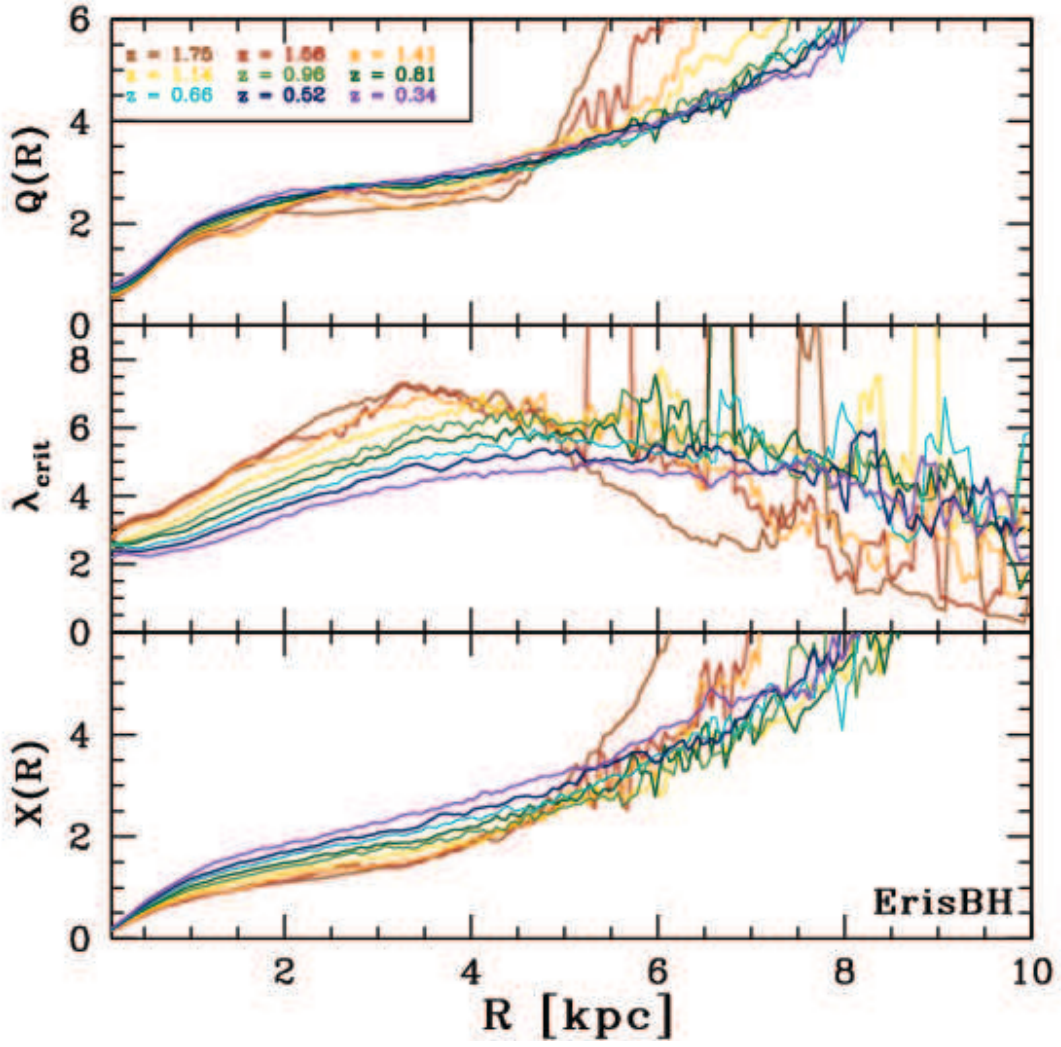

Figure 7.11: Same as Figure 7.10 but for Eris2k.

7.5 Conclusions

In this study, I presented a detailed comparison of the differences between two distinct cosmological zoom-in simulations starting with the same initial conditions. The different physical prescriptions on unresolved scales assumed in the two runs resulted in the formation of two disc barred galaxies whose bars show very different properties. A bar forms early ($z \approx 1.1$) in Eris2k, reaching a size of $\gtrsim 6$ kpc within a very short initial growth phase of ≈ 1 Gyr. After such sudden growth, both the bar length and precession velocity remain approximately constant up to the final stages of weakening due to a bar-triggered gas inflow as in the bar-suicide scenario. Large and fast bars, like that of Eris2k, are not uncommon in the Universe. Some examples are provided, for instance, by NGC–266, NGC–1530, NGC–2595, or NGC–7479 (Font et al., 2017, see

Figure 7.12). On the other hand, the bar in ErisBH starts forming at slightly later times ($z \approx 0.7$) and keeps increasing its size (and decreasing its precession velocity) until the end of the run. The bar in ErisBH remains always smaller than its Eris2k counterpart, reaching a maximum size of ~ 4 kpc at $z \sim 0$, when it stops growing due to a buckling event.

Figure 7.12: SB(rs)b galaxy NGC–1530 (left, Adam Block–Mount Lemmon SkyCenter) and SB(s)c galaxy NGC–7479 (right, Hubble Space Telescope). Both galaxies show an enormous (about 16 and 11 kpc, respectively) and very fast rotating ($\mathcal{R} = 1.17, 1.14$, respectively; see § 5.1.2.2) bar. Data are provided by Font et al. (2017).

In chapter 5, I demonstrated that the last minor merger in the ErisBH simulation does not provide the initial trigger necessary to the formation of the bar. However, the encounter can induce a delay in the formation time. The difference between the bar formation epochs of ErisBH and Eris2k, being of the same order of magnitude of such a delay, could also be explained by a dynamical perturbation external to the galactic environment. As a consequence, it is not clear whether the overall feedback produces any variation in the bar formation time, but it surely sensibly controls its structural properties by moulding the disc potential both on small and large scales.

The distinct bar evolutions and features are due to the different mass growths of the galaxy. The stronger stellar feedback in Eris2k has the effect of initially pushing the gas out of the galaxy, more effectively reducing the SF, and results, in turn, in an initial stellar mass smaller than that in ErisBH. The pushed-away gas flows back onto the main galaxy but, only when the disc is massive enough to prevent SN-driven massive gas ejections, Eris2k starts forming stars with high SF rate. The more efficient removal of low angular momentum gas at early times in Eris2k results in a lower CMC with respect to ErisBH. Such central stellar nuclei contribute in shaping the overall gravitational potential of the two galaxies, initially determining the size of the bar-unstable regions and, on the long run, the bar evolutions.

A recent study by Gavazzi et al. (2015) has observationally proved a link between a knee mass ($M_{\rm knee}$) in the specific SF rate versus stellar mass plane for local star forming galaxies and the occurrence of strong bars at $z \sim 0$. They

further speculated that the increased probability of forming a bar at high masses could explain the correlation they found between $M_{\rm knee}$ and z. The paucity of sufficiently high angular resolution images of stellar discs at cosmological distances prevents the statistical confirmation of such conjecture. Interestingly, the bars in ErisBH and Eris2k form when the galaxies become more massive than $M_{\rm knee}(z)$, as shown in Figure 7.1. A larger statistical sample of high-resolution cosmological simulations of disc galaxies could populate the bar-formation-mass versus z plane, to theoretically probe the redshift-dependent mass threshold for bar formation proposed by Gavazzi et al. (2015).

It is noteworthy how well the feedback prescriptions can be connected to the different bar morphologies. Although the rigid constraints chosen to identify a strong bar (which are the subject of this investigation) are not fulfilled in the ErisBH run for $z > 0.7$, a small non-axisymmetric overdensity could anyway be observed, surely more pronounced with respect to the Eris2k equivalent galaxy (at the same redshift; see Figure 7.3). Despite the presence of this possible proto-bar (that can also be due to spurious numerical effects, as stressed in § 7.2), it is clear that the evolved bar at lower redshift remains close to the nuclear region, in contrast with the grand-scale bar of Eris2k. These differences could be attributed to the distinct domains of the feedback mechanisms: whereas the effect of MBH feedback is confined to the region < 1 kpc, the strong stellar feedback in Eris2k acts on a global scale.

Even though the analysis is limited to only two cosmological zoom-in simulations, it is enticing to speculate on the general relationship between feedback and bars. From the results presented in this work, one can expect that, at low redshift ($z \lesssim 1$), bars are generally stronger and longer when the feedback is enhanced. Since strong/long bars are easier to observe, especially at $z \gtrsim 0.5$, the number of observed bars could give us some hints on the strength of stellar feedback during the cosmological build-up of galaxies. However, this comparison is possibly degenerate with other physical phenomena, such as the global merging history and environment.

In conclusion, this study clearly highlights a link between the structural properties of bars (and of the whole discs) and the sub-resolution physics implemented in simulations. This connection could be exploited to constrain and better tune the parameters of such implementations, possibly breaking the degeneracy with other free parameters such as, e.g. spatial and mass resolution or MBH physics. A large number of high-resolution cosmological simulations would be necessary for the purpose, also to isolate the influence of the external perturbations on to the processes of bar formation and evolution (see, chapter 6 for an example on the Eris2k case).

Chapter 8

Conclusions

Bars play undoubtedly a fundamental role in disc galaxy evolution. They indeed can alter considerably the stellar and gaseous distribution in the disc and the signs of bar-driven transformation are visible long after the demise of the bar structure itself.

Despite all the efforts to determine the complex interplay between bars and their host environment, some aspects of bar formation and evolution remain today still unconstrained. N-body simulations represent the main tool to probe these intricate dynamical problems, but only recently the hardware performance and code scalability have allowed to replicate highly resolved systems, with realistic boundary conditions.

In this thesis, I have contributed to the investigations of two essential topics in bar formation and evolution: the effects of tidal encounters and the importance of sub-grid physics. All the analysis have been performed over zoom-in cosmological simulations which succeeded in reproducing realistic Milky Way-sized galaxies within their resolved region.

8.1 The effects of tidal interactions

In chapter 5, I focussed on the origin of the strong bar visible in the ErisBH galaxy at $z = 0$. I tested whether the initial perturbations responsible for the two-fold structure formation was either due to internal processes only, or could be found outside the galactic environment (in the form of a tidal encounter).

To do so, I ran different versions of the last stages ($z \lesssim 2$) of the ErisBH run, each time with a slight modification of its interaction history. In particular, after re-simulating the unchanged ErisBH system as a control sample, I

- removed the LMM at $z \sim 1.1$;
- removed the LMM and avoided the formation of the satellite that would have undercome the closest passage at $z \sim 0.7$ (closest flyby);

- removed the LMM and provided the flyby with a radial velocity component in order to reduce its gravitational influence over the main system;

- removed the LMM and doubled the DM mass of the flyby, to increase the perturbing effect of the satellite over the main galaxy.

The results confirm that a strong non-axisymmetry is visible at $z = 0$ in every simulated case. As a consequence, I did not find the trigger of bar formation in any of the tidal encounter analysed. As a matter of fact, an even stronger and longer bar forms when the merger and the flyby do not occur at all, and it appears to be more pronounced and evolved in the least perturbed cases. Similarly, Moetazedian et al. (2017) found that a satellite could, at most, postpone or anticipate the formation of the bar, without affecting the main properties of the structures. A galaxy will develop a bar after it has become bar-unstable (which is the case of the main galaxy in ErisBH simulation after $z \lesssim 2$; Spinoso et al. 2017), regardless of its interactions with external objects. The main driver of bar formation seems to be more connected to the galaxy self-gravity and to how this property influence the disc secular evolution processes (in agreement with, e.g. Debattista et al., 2006). Obviously, the situation would be very different if the perturbation is violent enough to significantly modify the galactic potential well. For instance, a major merger would be able to completely alter the morphology of the system, transforming it to a pressure-supported spheroid, incapable to host a stellar sub-structure with proper precession frequency (a similar case was the outcome of a last run performed, but not analysed, where the DM mass of the flyby has been further increased; see § 5.2).

Once the bar is formed and fully established, the flyby appears to have a delaying effect on the bar growth. The reason could lie in the increase of the stellar velocity dispersion induced in the close interaction and resulting in a more stable disc (Guedes et al., 2013). However, a still wide region of the orbital parameter space must be investigated and, in particular, the effect of the satellite orbital angular momentum could be a crucial factor on the perturbation effect (see § 8.3.1).

In chapter 6, I deepened the subject of flyby-induced perturbations on barred system. The analysis has been performed over the Eris2k cosmological simulation, where the strongest interaction after the formation of the bar is the passage of a companion galaxy with very unequal mass ratio and relatively close pericentre. The perturbation, in spite of the satellite low mass content, is able to considerably shuffle the orbits which contribute to the bar structure, promoting in this way a phase, where the bar disappears for almost 1 Gyr. After this *apparent death* (see § 3.4.2.1), the bar reforms with almost the same strength and length it had before the interaction. The bar is resilient because the galactic potential did not experience any appreciable modification and the disc remains strongly bar-unstable. When the galaxy starts over to evolve in isolation (when the perturbation passes), the energy of the interaction is dissipated and the self-gravity of the bar relic quickly re-assembles the previous structure. The main conclusions of this analysis can be summarized with the following:

1. a highly unequal-mass perturber is able to deeply modify the appearance of a disc galaxy (*short-term effect*). The interaction can also change the morphological type of the object (from barred to unbarred);

2. the (completely) disappearance of the strong bar can be only temporary and the features of the re-assembled bar are almost identical to the the structure before the pericentre: it is not a new bar, but the same orbits in the same old (nearly) unchanged potential are repopulated (*long-term effect*);

3. however, the non-negligible duration of the bar-less period may be important in, e.g., a survey to determine the fraction of barred system. Indeed, a strongly bar-unstable galaxy could be classified as non-barred or weakly barred during the phase of orbit-shuffling or bar-regrowth. In addition, some occasionally observed structures, such as lenses or ovals could be produced during this latter stage;

4. finally, the overall effect of the perturber is destructive on the bar structure.

Point 4 describes a scenario in which tidal interactions are likely to be antagonistic to bar formation and evolution. This is in agreement with chapter 5, where the general influence of the perturbations (resulting either in a merger, or just in flyby) was to delay or slightly inhibit the formation or the growth of the structure.
The additional sibling run performed (see § 5.2), where the DM mass of the flyby has been further increased, resulted in a later major merger which profoundly changed the nature of the target system. Even though I did not analyse the output of this simulation, for it has produced a far different outcome with respect to the other siblings, the case would anyway contribute to the same scenario of point 4. It is interesting to note that, some observative works (see, e.g. Lin et al., 2014) found that barred galaxies prefer less dense environment, where mergers and close encounters in general are less probable. In conclusion, depending on the development stage of the bar, either its growth can appear delayed, or its whole structure can be destroyed (if the bar is fully grown and established) for a limited period.

Most works finds a decreasing bar fraction toward higher redshift (Sheth et al., 2008; Melvin et al., 2014; Simmons et al., 2014). When the Universe was younger, spiral galaxies were less massive, according to the hierarchical formation of structures. This is compatible with the hypothesis that self-gravitation is the main driver of bar formation, since smaller galaxies could have not reached yet the needed mass necessary to host a strong bar. However, at higher redshift the also increasing rate of tidal interactions (e.g. Hammer et al., 2009) would represent a competitive process in order to justify the reduced population of barred galaxies with respect to $z = 0$.

It must be considered that the orbital angular momentum of the interacting companion may play a major role on the outcomes of the gravitational perturbations discussed. For instance, Peschken and Łokas (2018) distinguish

the encounters according to the orbital angular momentum of the approaching satellite, and conclude that strong interactions on prograde orbits could even enhance the intensity of the non-axisymmetric structure in the target galaxy. Even if the results has to be taken with caution because of the low time, mass and spatial resolution adopted to describe such a sub-galactic scale phenomenon, the effect must be tested in high resolution zoom-in simulations in order to generalize the claimed impact of external perturbers (see § 8.3).

8.2 The effects of sub-grid physics

In chapter 7, I carefully compared the outputs of the two simulations ErisBH and Eris2k, focussing on the impact that different sub-grid physics prescriptions can have on the processes of bar formation and evolution.

The different effective feedbacks implemented (from stars and MBH) produce two distinct accretion histories in the galaxies. At $z \gtrsim 3$, the larger number (mainly due to the implementation of K01 instead of K93 as IMF) of more efficient (due to the higher $\epsilon_{\rm SN}$) SNe, expel the weakly bounded interstellar medium from the Eris2k disc. The gas is re-accreted on to the disc at later time as the galactic potential well increases. As a consequence, the Eris2k run, compared to the ErisBH central system, starts its evolution with a lower amount of stars (and DM), but slowly reaches (at $z \sim 1$) and exceeds the mass level of ErisBH. Moreover, even though the MBH feedback in ErisBH succeeds in reducing an otherwise large CMC (as in the Eris original run, according to Bonoli et al. 2016), the Eris2k galaxy, due to the overall stronger feedback, is able to evolve as a pure disc with no bulge component prior to the onset of the bar (as shown by the analysis of both stellar density and stellar kinematics by Sokołowska et al. 2017).

The consequent differences in the shape of the galactic potentials are then reflected in the creation of two distinct bar structures: a shorter and slow-evolving bar in ErisBH, and a more extended and almost static bar in Eris2k.

The main conclusions of chapter 7 can be summarised in the following:

1. the major difference between the bars do not lie in the formation epochs, but in their structural properties. According to chapter 5, once the disc has become bar-unstable, the initial instabilities can be searched within the host system, possibly in the chaotic nature of its own environment, rather than among external perturbations. The delay in the formation times of the structures could be explained by a dynamical interaction which temporary increases the random motion of the stars (as it appears to be the general influence of external perturbations). On the other hand the bars show very different masses and sizes, which, in turn, affect their evolutionary histories (a more massive bar has a higher inertia against its evolution);

2. both the bars form when the stellar mass of the galaxy becomes higher than the $M_{\rm knee}(z)$ provided in Gavazzi et al. (2015). This further support the scenario of galactic self-gravity as major driver of the bar formation process;

3. beyond the obvious effect on the global mass distribution produced by the feedback, there is a clear correlation between the size of the bars and the physical regions where the feedback mechanisms dominate. Whereas the MBH activity affects only the first kpc in the ErisBH galaxy, the enhanced stellar feedback of the Eris2k simulation is distributed all over the disc, and the two bars lie in the nearly corresponding "bar-unstable zones";

4. the relationship between sub-grid physics and bars could provide a further independent tool to investigate the two phenomena. If bars are truly stronger and larger when the feedback is enhanced, resolving a bar structure in the local Universe could give information about, e.g., the rate of SN explosions or the past MBH activity. Moreover, since strong and more extended bars are easier to identify and to observe, bar fraction alone could provide an indicator of strength of the stellar feedback in the sample. Finally, the relation could also be exploited when designing the newest zoom-in cosmological simulations, in order to produce more or less strong barred systems. Unfortunately, the effects of feedback are degenerate with other factors, such as the merging history of the systems and more numerical studies should investigate this aspect (see § 8.3.3).

In conclusion, an external trigger is not necessary in order to form a bar when the disc is already bar-unstable, instead, tidal encounters have, in general, a destructive effect on to bar structures whether forming or evolving. The mass seems to be the main requirement in order to trigger bar formation, at any given value of the radial velocity dispersion, and the feedback play a major role in shaping the galactic potential, in order to make a disc bar-unstable.

8.3 Future prospects

The recent developments in computational astrophysics created a series of exciting conditions for the cosmological investigation of barred systems.

8.3.1 Dependence on the angular momentum

As previously discussed, the orbital angular momentum of a perturber has been proposed (e.g. Gerin, Combes, and Athanassoula, 1990; Romano-Díaz et al., 2008; Lang, Holley-Bockelmann, and Sinha, 2014; Łokas et al., 2016; Peschken and Łokas, 2018) to have considerable importance on the outcome of its tidal interaction with a barred galaxy.[1] However, what is missing is a full cosmological study with the needed resolution to proper address the problem.

In order to generalize the results of chapter 5 and 6, a natural follow-up of my work would be the analysis of other systems, analogous to those described in chapter 4, with different orbital parameters for the interacting flyby. The strength of this work would rely both on the solid cosmological framework of

[1] Not only the orbital angular momentum, but also the relative position of the satellite at the pericentre with respect to the bar; see § 3.4.2.

the Eris suite simulations, and on the high spatial and mass resolution provided by the zoom-in nature of the runs.
The orbit of the flyby in chapter 5 is more or less retrograde, whereas it is almost completely prograde for the small satellite of chapter 6. Although the two orbits are substantially different, I found the effect on the growing structure to be nearly the same. However, the strength of the perturbation can have a significant part in determining the reaction of the growing bar (see, e.g. Peschken and Łokas, 2018). A more numerous sample of interactions would also allow to investigate the dependence on the intensity of the perturbation.

8.3.2 Very large zoom-in cosmological simulation

One of the main limits of zoom-in cosmological simulations is the lack of statistics. To strengthen the results of the study of the effects of tidal interactions, a higher number of barred systems has to be analysed. A possible solution is to run a larger cosmological box with multiple refined zones, centred on different galaxies with similar properties. In this context, I would follow the onset of the bar instability in various field disc galaxies with different evolutionary histories and final masses. More objects in the same cosmological volume would allow, on the one hand, to deeper sample the space of the dynamical parameters linked to bar formation and evolution and, on the other, to save time and optimize the computational efforts.

This ambitious approach would be possible only thanks to the latest parallel-computing strategies and hardware facilities. In particular, in agreement with the original work described in chapter 5, I would take advantage of the last version of the state-of-the-art SPH N-body code ChaNGa (see § 4.1.3), which proved to be very stable and versatile with highly clustered datasets. Indeed, the code showed almost perfect scalability up to 128K cores for a multi-stepping run with 2×10^9 particles (Menon et al., 2015).

A larger statistical sample of highly resolved disc galaxies could also contribute to theoretically test how the mass threshold for bar formation evolves with redshift and if it has the trend proposed by Gavazzi et al. (2015).

8.3.3 Feedback

Focussing on the sub-grid physics effect, it is important to further populate the bar formation versus feedback plane to quantitatively investigate the relation. Given the complexity of the topic, various external influences has to be isolate in order to verify the role of feedback on the formation of sub-structures, such as the interaction with the galaxy satellites and the environment.

A deeper analysis of the central stellar system in the Eris original simulation could confirm or improve the results of chapter 7, since the run has the same initial conditions but different sub-grid methods. In particular the Eris simulation does not implement any BH accretion prescription, whereas the stellar feedback has a much lower intensity with respect to the Eris2k run. After this, a new zoom-in hydrodynamical and cosmological simulation of a field barred galaxy,

can be performed adopting a further enhanced stellar feedback (provided that the higher injected energy will not significantly change the disc morphology).

Engineering these modern state-of-the art simulations proved to be a fruitful way of probing the particular topics of my analysis. Providing an advantageous cosmological laboratory, this approach still has a huge potential for the study of galactic dynamics.

Appendix A

Fitting method

In this section, I provide a brief explanation of the adopted method to produce the one-dimensional fits of the stellar distributions, exemplified in Figure 4.2 for the final snapshots of the two runs, and in Figure A.1 at $z = 1.03$.

First, a stellar surface density profile is extracted from each snapshot by dividing the disc into 20 pc-wide concentric cylindrical bins, starting from the galactic centre. The height of the bins measures 8 kpc in order to ensure that the entire galactic structure is included and the external contaminations are minimized. The results are the black dashed lines of Figures A.1 and 4.2 on page 52.

The decomposition procedure is based on a fitting algorithm from Press et al. (1993) included in an iterative procedure discussed in the following.

For the case of ErisBH, the profiles are simpler with respect to Eris2k, and are typical of a disc galaxy with a small bulge/bar. For this reason, I use a superposition of two Sérsic functions (Sérsic, 1963; Sérsic, 1968) in order to represent these two components (see the red lines in the top panel of Figure A.1). The evolution of the galaxy is less disturbed by random encounters and its surface density shows a more predictable development. Accordingly, the method is almost completely automatised and flawlessly allows to find a satisfactory fit for each snapshot. Once the first snapshot at $z = 0$ is successfully fitted,[1] the resulting parameters are used as the initial guess for the previous (in time) contiguous snapshot and so on, towards higher redshift, when the trend of the density profiles becomes less and less trivial.

For Eris2k, given the higher complexity of the stellar mass distribution, a two-components fit is not sufficient, hence I select a four-components fit for the vast majority of the snapshots (see the bottom panel of Figure A.1) and a three-components fit for a few remaining snapshots at higher redshift. Operatively, (i) I first fit the galaxy outskirt only (for $R > 15$ kpc), using an exponential profile (blue solid line in the bottom panel of Figure A.1). Then (ii) I fit the

[1] The decomposition starts from the last temporal snapshot, since it is, in general, easier to fit.

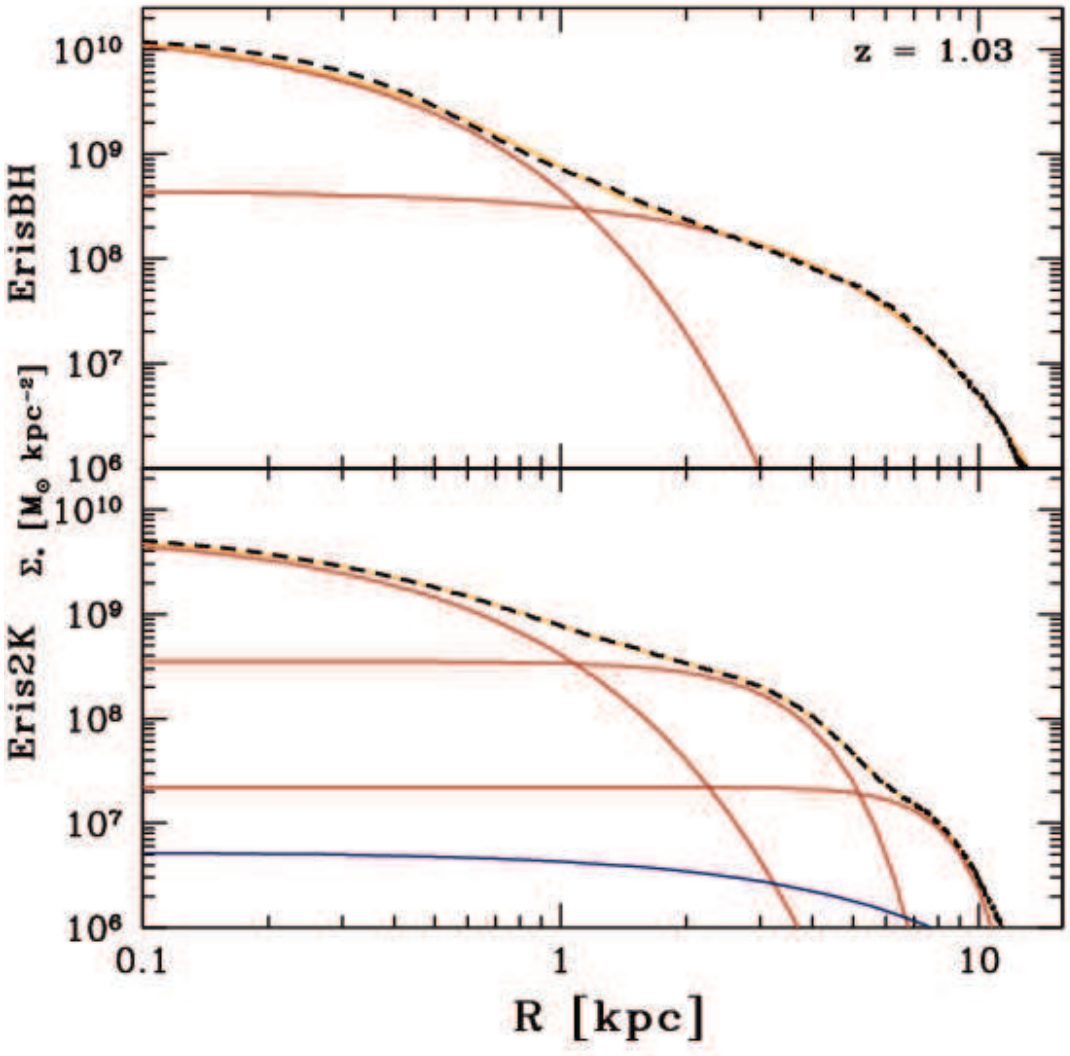

Figure A.1: Example of the fitting procedure applied onto the ErisBH (top panel) and Eris2k (bottom panel) main galaxies at $z = 1.03$. The agreements between the surface density profile Σ_* (black dashed lines) and the best fits (yellow solid lines) show the goodness of the fit. The red solid lines refer to the Sérsic components, whereas the blue solid line in the bottom panel represents the exponential function we use to fit the stellar background in Eris2k.

inner regions with three (two for a few cases) Sérsic profiles, keeping fixed the exponential background, previously extrapolated. In this case as well, I initially focus on the last snapshot (at $z = 0.31$), since its components are far more recognizable. Hence, the procedure is mostly automatised (with minimal or no user intervention), by adopting the outcoming fitting parameters of each snapshot as the initial guess for the next snapshot to analyse.

The method is applied recursively more than once for each profile, in order to achieve an even better final agreement.

Appendix B

Finding the bar in Eris2k

As anticipated in § 6.1 and § 7.2, the larger inhomogeneities and the overall higher granularity of the stellar distribution in the Eris2k run, mostly due to the specific feedback prescriptions implemented, result in density profiles less obvious to interpret (see also Appendix A). As a consequence, a clear bar is not always evident in every snapshot, for the $A_2(R)$ and the $A_2(<R)$ profiles have likely more than one peak within the investigated radial range. Figure B.1 shows two typical A_2 profiles coming from the Eris2k run. Differently from the ErisBH case, where almost every profile is unambiguous (as it is exemplified by the three snapshots shown in Figure 7.4), Eris2k offers numerous surface density profiles similar to the one in the left-hand panel of Figure B.1, where both $A_2(R)$ (blue line) and $A_2(<R)$ (black line) display more crests.

The various peaks could be due, for instance, to a deformation of the bar structure, to the growth of other disc instabilities, or to the presence of a stellar cluster. Thus, the real structure could be linked to any/none (or even more than one) of them.

In order to properly follow the evolution of the two-fold non-axisymmetry, regardless of the environmental disturbances, and to retrieve its correct parameters in the Eris2k main galaxy, I first collect, for each snapshot, a list of all the peaks in the $A_2(<R)$ profile (black lines in Figure B.1), that correspond to as many $m = 2$ overdensities. Then, for each peak, I check the phase-shift of its corresponding overdensity through Equation (3.2), after smoothing the phase at the peak $\Phi(R_{\rm peak})$ with a small kernel in order to obtain a more representative value for that overdensity. In detail, I select the structure only if the overdensity has constant phase, i.e. if $|\Phi(R_{\rm peak}) - \Phi(R)| < \arcsin(0.15)$, over a radial range $\Delta R > 0.6\, R_{\rm peak}$. When more than one overdensity survives this selection, I choose the one with the highest value of $A_2(R)$.

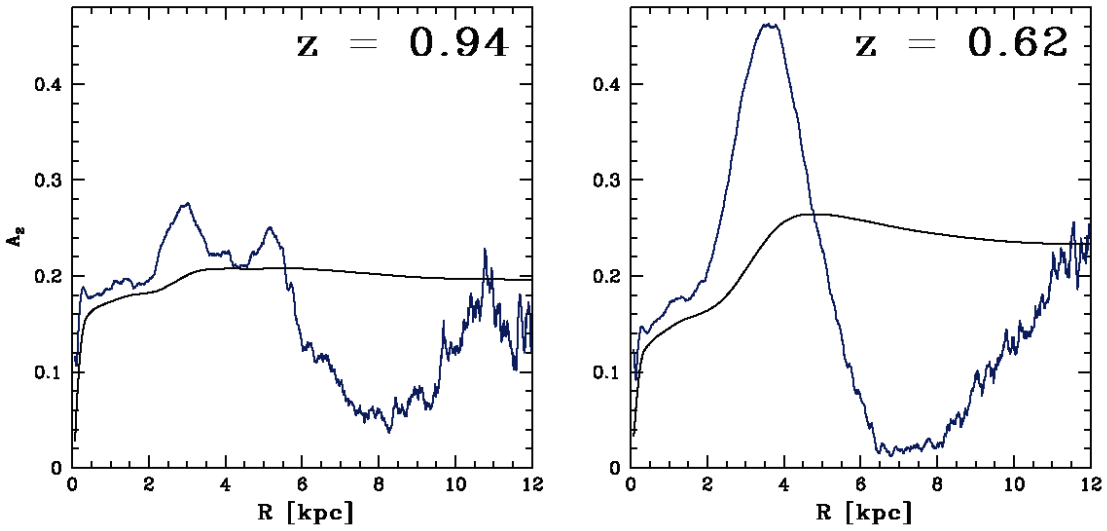

Figure B.1: Typical outcomes of the Fourier decomposition applied to the Eris2k primary galaxy. The colour code is the same used in the upper panels of Figure 7.4. The $A_2(R)$ profiles (blue lines) of two non-consecutive snapshots are superimposed on their relative $A_2(<R)$ profiles (black lines). The presence of various maxima in both the lines of the left panel requires an additional study (see text for more details).

Appendix C

Additional analysis

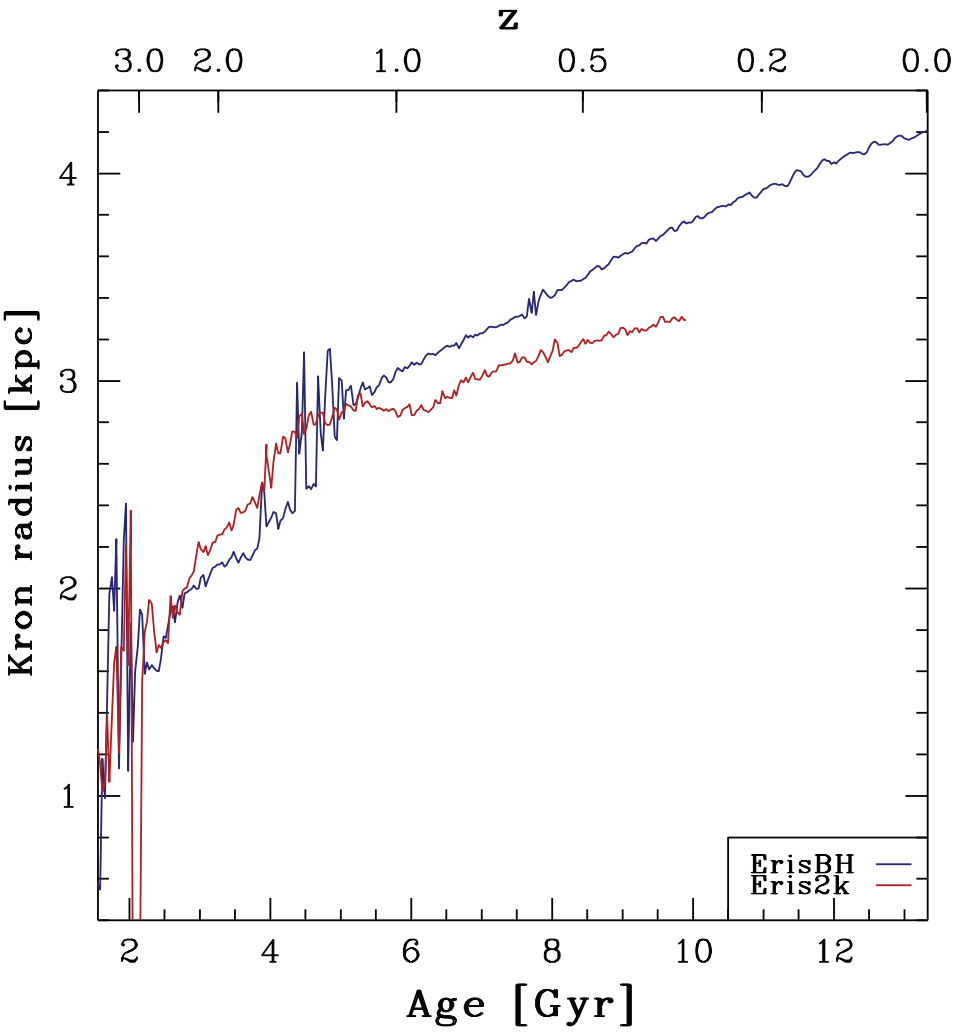

Figure C.1: Time evolution of the Kron radius (Equation 7.1) for the ErisBH (blue line) and Eris2k (red line) simulations.

As discussed in § 7.1, the Kron radii of the two simulations (Figure C.1) are

very similar and show almost the same trend (the differences are within ~ 10 per cent of each other). Also for this property, Eris2k (red line) has a lower evolution in redshift with respect to ErisBH (blue lines), once the bar has formed (~ 5.3 Gyr). The fluctuations in the blue line at ~ 5 Gyr are due to the merger in ErisBH.

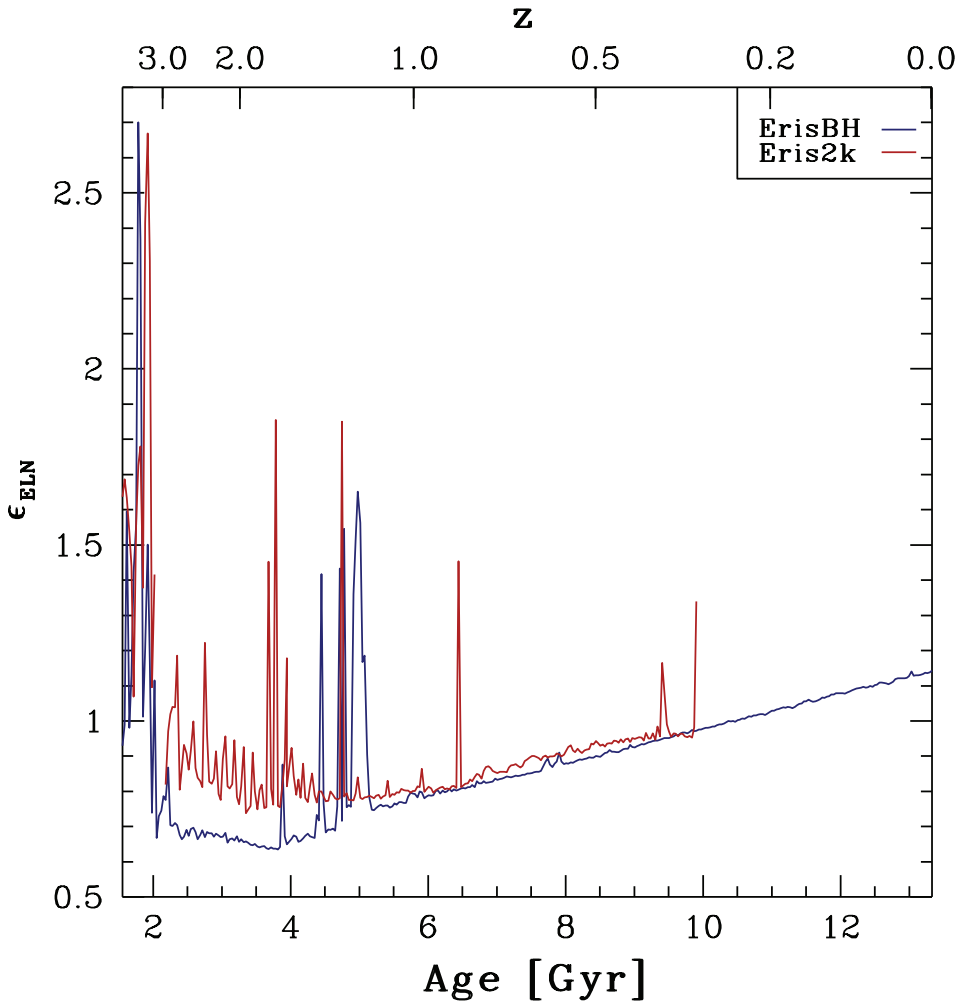

Figure C.2: Evolution of the $\epsilon_{\rm ELN}$ criterion for the two simulations analysed in chapter 7 with the same colour code adopted in Figure C.1.

Figure C.2, shows the time evolution of the $\epsilon_{\rm ELN}$ criterion (Efstathiou, Lake, and Negroponte, 1982) computed via Equation 3.6, considering all the stellar particles within a cylinder of radius 5 times the corresponding Kron radius and height of 4 kpc.

Although the criterion does not consider the stellar velocity dispersion, it provides a quantitative estimate of the disc self-gravity. Using the threshold of $\epsilon \sim 1$ (see § 3.3), it is clear that both the galaxies are bar-unstable till $z \sim 0.2$ (the galaxy in the Eris2k run is always under the threshold). The result does not help in order to determine the formation time of the bars, however the criterion is undoubtedly fulfilled in both the systems when the instabilities start growing.

Bibliography

Algorry, D. G. et al. (July 2017). "Barred galaxies in the EAGLE cosmological hydrodynamical simulation". In: MNRAS 469, pp. 1054–1064. DOI: 10.1093/mnras/stx1008. arXiv: 1609.05909 (cit. on pp. 29, 34).

Alonso, M. S., G. Coldwell, and D. G. Lambas (Jan. 2013). "Effect of bars in AGN host galaxies and black hole activity". In: A&A 549, A141, A141. DOI: 10.1051/0004-6361/201220117. arXiv: 1211.5156 (cit. on p. 9).

Appel, A. W. (Jan. 1985). "An Efficient Program for Many-Body Simulation". In: *SIAM Journal on Scientific and Statistical Computing, vol. 6, no. 1, January 1985, p. 85-103.* 6, pp. 85–103 (cit. on p. 42).

Athanassoula, E. (Nov. 1992). "The existence and shapes of dust lanes in galactic bars". In: MNRAS 259, pp. 345–364. DOI: 10.1093/mnras/259.2.345 (cit. on pp. xii, 9).

Athanassoula, E. (Apr. 2002). "Bar-Halo Interaction and Bar Growth". In: ApJ 569, pp. L83–L86. DOI: 10.1086/340784. eprint: astro-ph/0203368 (cit. on p. 35).

Athanassoula, E. (June 2003). "What determines the strength and the slowdown rate of bars?" In: MNRAS 341, pp. 1179–1198. DOI: 10.1046/j.1365-8711.2003.06473.x. eprint: astro-ph/0302519 (cit. on pp. xi, 35).

Athanassoula, E. (Jan. 2005a). "Dynamical Evolution of Barred Galaxies". In: *Celestial Mechanics and Dynamical Astronomy* 91, pp. 9–31. DOI: 10.1007/s10569-004-4947-7. eprint: astro-ph/0501196 (cit. on p. 7).

Athanassoula, E. (Apr. 2005b). "On the nature of bulges in general and of box/peanut bulges in particular: input from N-body simulations". In: MNRAS 358, pp. 1477–1488. DOI: 10.1111/j.1365-2966.2005.08872.x. eprint: astro-ph/0502316 (cit. on p. 9).

Athanassoula, E. (June 2007). "A bar in the inner halo of barred galaxies - I. Structure and kinematics of a representative model". In: MNRAS 377, pp. 1569–1578. DOI: 10.1111/j.1365-2966.2007.11711.x. eprint: astro-ph/0703184 (cit. on p. 7).

Athanassoula, E. (July 2008a). "Boxy/peanut and discy bulges: formation, evolution and properties". In: *Formation and Evolution of Galaxy Bulges*. Ed. by M. Bureau, E. Athanassoula, and B. Barbuy. Vol. 245. IAU Symposium, pp. 93–102. DOI: 10.1017/S1743921308017389 (cit. on pp. 5, 37).

Athanassoula, E. (Oct. 2008b). "Disc instabilities and semi-analytic modelling of galaxy formation". In: MNRAS 390, pp. L69–L72. DOI: 10.1111/j.1745-3933.2008.00541.x. arXiv: 0808.0016 (cit. on p. 33).

Athanassoula, E., R. E. G. Machado, and S. A. Rodionov (Mar. 2013). "Bar formation and evolution in disc galaxies with gas and a triaxial halo: morphology, bar strength and halo properties". In: MNRAS 429, pp. 1949–1969. DOI: 10.1093/mnras/sts452. arXiv: 1211.6754 (cit. on p. 88).

Athanassoula, E. and L. Martinet (July 1980). "A correlation between the lengths of bars and the sizes of bulges". In: A&A 87, p. L10 (cit. on p. 5).

Athanassoula, E. and A. Misiriotis (Feb. 2002). "Morphology, photometry and kinematics of N -body bars - I. Three models with different halo central concentrations". In: MNRAS 330, pp. 35–52. DOI: 10.1046/j.1365-8711.2002.05028.x. eprint: astro-ph/0111449 (cit. on pp. 30, 31, 67).

Athanassoula, E. and J. A. Sellwood (July 1986). "Bi-symmetric instabilities of the Kuz'min/Toomre disc". In: MNRAS 221, pp. 213–232. DOI: 10.1093/mnras/221.2.213 (cit. on pp. 27, 32).

Athanassoula, E. et al. (Nov. 1983). "Orbits as building blocks of a barred galaxy model". In: A&A 127, pp. 349–360 (cit. on p. 26).

Balsara, D. S. (1995). "von Neumann stability analysis of smooth particle hydrodynamics–suggestions for optimal algorithms". In: *Journal of Computational Physics* 121, pp. 357–372. DOI: 10.1016/S0021-9991(95)90221-X (cit. on p. 46).

Barnes, J. and P. Hut (Dec. 1986). "A hierarchical O(N log N) force-calculation algorithm". In: Nature 324, pp. 446–449. DOI: 10.1038/324446a0 (cit. on pp. 41, 42).

Bauer, J. S. and L. M. Widrow (Aug. 2018). "Can Stellar Discs in a Cosmological Setting Avoid Forming Strong Bars?" In: *ArXiv e-prints*. arXiv: 1809.00090 (cit. on p. 32).

Bellovary, J. M. et al. (Oct. 2010). "Wandering Black Holes in Bright Disk Galaxy Halos". In: ApJ 721, pp. L148–L152. DOI: 10.1088/2041-8205/721/2/L148. arXiv: 1008.5147 [astro-ph.CO] (cit. on pp. 47, 48).

Benz, W. (1989). *Numerical Modelling of Stellar Pulsation* (cit. on p. 46).

Berentzen, I. et al. (Oct. 1998). "Gas-driven evolution of stellar orbits in barred galaxies". In: MNRAS 300, pp. 49–63. DOI: 10.1046/j.1365-8711.1998.01836.x. eprint: astro-ph/9806138 (cit. on p. 37).

Binney, J. and M. Merrifield (1998). *Galactic Astronomy* (cit. on pp. xi, 7).

Binney, J. and S. Tremaine (2008). *Galactic Dynamics: Second Edition*. Princeton University Press (cit. on pp. 12, 32, 101).

Bird, J. C. et al. (Aug. 2013). "Inside out and Upside down: Tracing the Assembly of a Simulated Disk Galaxy Using Mono-age Stellar Populations". In: ApJ 773, 43, p. 43. DOI: 10.1088/0004-637X/773/1/43. arXiv: 1301.0620 (cit. on p. 46).

Blackman, C. P. (Jan. 1983). "UBVRI Surface Photometry of the Barred Spiral NGC7479". In: MNRAS 202, p. 379. DOI: 10.1093/mnras/202.2.379 (cit. on p. 5).

Blumenthal, G. R. et al. (Feb. 1986). "Contraction of dark matter galactic halos due to baryonic infall". In: ApJ 301, pp. 27–34. DOI: 10.1086/163867 (cit. on p. 86).

Bondi, H. (1952). "On spherically symmetrical accretion". In: MNRAS 112, p. 195. DOI: 10.1093/mnras/112.2.195 (cit. on p. 47).

Bondi, H. and F. Hoyle (1944). "On the mechanism of accretion by stars". In: MNRAS 104, p. 273. DOI: 10.1093/mnras/104.5.273 (cit. on p. 47).

Bonoli, S. et al. (July 2016). "Black hole starvation and bulge evolution in a Milky Way-like galaxy". In: MNRAS 459, pp. 2603–2617. DOI: 10.1093/mnras/stw694. arXiv: 1508.07328 (cit. on pp. 29, 34, 46, 47, 57, 110).

Bournaud, F. and F. Combes (Jan. 2004). "Bar dissolution and reformation mechanisms". In: *Penetrating Bars Through Masks of Cosmic Dust*. Ed. by D. L. Block et al. Vol. 319. Astrophysics and Space Science Library, p. 165. DOI: 10.1007/978-1-4020-2862-5_13 (cit. on p. 38).

Bovino, S. et al. (May 2016). "A chemical model for the interstellar medium in galaxies". In: A&A 590, A15, A15. DOI: 10.1051/0004-6361/201628158. arXiv: 1510.07016 (cit. on p. 50).

Bromm, V. et al. (Dec. 2001). "The fragmentation of pre-enriched primordial objects". In: MNRAS 328, pp. 969–976. DOI: 10.1046/j.1365-8711.2001.04915.x. eprint: astro-ph/0104271 (cit. on p. 50).

Brooks, A. M. et al. (Feb. 2011). "Interpreting the Evolution of the Size-Luminosity Relation for Disk Galaxies from Redshift 1 to the Present". In: ApJ 728, 51, p. 51. DOI: 10.1088/0004-637X/728/1/51. arXiv: 1011.0432 (cit. on p. 29).

Bureau, M. and E. Athanassoula (June 2005). "Bar Diagnostics in Edge-On Spiral Galaxies. III. N-Body Simulations of Disks". In: ApJ 626, pp. 159–173. DOI: 10.1086/430056. eprint: astro-ph/0403226 (cit. on pp. xii, 36).

Bureau, M. et al. (Aug. 2006). "K-band observations of boxy bulges - I. Morphology and surface brightness profiles". In: MNRAS 370, pp. 753–772. DOI: 10.1111/j.1365-2966.2006.10471.x. eprint: astro-ph/0606056 (cit. on p. 36).

Byrd, G. and M. Valtonen (Feb. 1990). "Tidal generation of active spirals and S0 galaxies by rich clusters". In: ApJ 350, pp. 89–94. DOI: 10.1086/168362 (cit. on p. 33).

Byrd, G. G. et al. (Sept. 1986). "Tidal triggering of Seyfert galaxies and quasars - Perturbed galaxy disk models versus observations". In: A&A 166, pp. 75–82 (cit. on p. 33).

Capelo, P. R. et al. (Apr. 2018). "The effect of non-equilibrium metal cooling on the interstellar medium". In: MNRAS 475, pp. 3283–3304. DOI: 10.1093/mnras/stx3355. arXiv: 1710.01302 (cit. on p. 50).

Chandrasekhar, S. (Nov. 1941). "A Statistical Theory of Stellar Encounters." In: ApJ 94, p. 511. DOI: 10.1086/144357 (cit. on p. 11).

Cheung, E. et al. (Dec. 2013). "Galaxy Zoo: Observing Secular Evolution through Bars". In: ApJ 779, 162, p. 162. DOI: 10.1088/0004-637X/779/2/162. arXiv: 1310.2941 (cit. on pp. xii, 8).

Cheung, E. et al. (Feb. 2015). "Galaxy Zoo: Are bars responsible for the feeding of active galactic nuclei at $0.2 < z < 1.0$?" In: MNRAS 447, pp. 506–516. DOI: 10.1093/mnras/stu2462. arXiv: 1409.5434 (cit. on p. 9).

Choi, J.-H. et al. (Nov. 2006). "Dark matter halo response to the disc growth". In: MNRAS 372, pp. 1869–1874. DOI: 10.1111/j.1365-2966.2006.10990.x. eprint: astro-ph/0604587 (cit. on p. 3).

Christodoulou, D. M., I. Shlosman, and J. E. Tohline (Apr. 1995). "A new criterion for bar-forming instability in rapidly rotating gaseous and stellar systems. 2: Nonaxisymmetric form". In: ApJ 443, pp. 563–569. DOI: 10.1086/175548. eprint: astro-ph/9502074 (cit. on p. 32).

Cisternas, M. et al. (Apr. 2015). "The Role of Bars in AGN Fueling in Disk Galaxies Over the Last Seven Billion Years". In: ApJ 802, 137, p. 137. DOI: 10.1088/0004-637X/802/2/137. arXiv: 1409.2871 (cit. on p. 8).

Coelho, P. and D. A. Gadotti (Dec. 2011). "Bars Rejuvenating Bulges? Evidence from Stellar Population Analysis". In: ApJ 743, L13, p. L13. DOI: 10.1088/2041-8205/743/1/L13. arXiv: 1111.1736 (cit. on p. 8).

Cole, D. R. et al. (Dec. 2014). "The formation of stellar nuclear discs in bar-induced gas inflows". In: MNRAS 445, pp. 3352–3369. DOI: 10.1093/mnras/stu1985. arXiv: 1410.4339 (cit. on p. 9).

Colín, P., O. Valenzuela, and A. Klypin (June 2006). "Bars and Cold Dark Matter Halos". In: ApJ 644, pp. 687–700. DOI: 10.1086/503791. eprint: astro-ph/0506627 (cit. on p. 7).

Combes, F. (1994). "Gas Inflow due to Perpendicular Orbits in Barred Potentials". In: *Mass-Transfer Induced Activity in Galaxies*. Ed. by I. Shlosman, p. 170 (cit. on p. 37).

Combes, F. (2000). "Bar-driven Galaxy Evolution and Time-scales to Feed AGN". In: *Dynamics of Galaxies: from the Early Universe to the Present*. Ed. by F. Combes, G. A. Mamon, and V. Charmandaris. Vol. 197. Astronomical Society of the Pacific Conference Series, p. 15. eprint: astro-ph/9908145 (cit. on p. 8).

Combes, F. (Nov. 2004). "The role of bars". In: *The Interplay Among Black Holes, Stars and ISM in Galactic Nuclei*. Ed. by T. Storchi-Bergmann, L. C. Ho, and H. R. Schmitt. Vol. 222. IAU Symposium, pp. 383–388. DOI: 10.1017/S1743921304002704. eprint: astro-ph/0404210 (cit. on pp. xi, 37).

Combes, F. and M. Gerin (Sept. 1985). "Spiral structure of molecular clouds in response to bar forcing - A particle simulation". In: A&A 150, pp. 327–338 (cit. on p. 9).

Combes, F. and R. H. Sanders (Mar. 1981). "Formation and properties of persisting stellar bars". In: A&A 96, pp. 164–173 (cit. on pp. 5, 32, 36).

Combes, F. et al. (July 1990). "Box and peanut shapes generated by stellar bars". In: A&A 233, pp. 82–95 (cit. on pp. 27, 36, 37).

Combes, F. et al. (May 2014). "ALMA reveals the feeding of the Seyfert 1 nucleus in NGC 1566". In: A&A 565, A97, A97. DOI: 10.1051/0004-6361/201423433. arXiv: 1401.4120 (cit. on pp. 8, 78, 93).

Consolandi, G. (Oct. 2016). "Automated bar detection in local disk galaxies from the SDSS. The colors of bars". In: A&A 595, A67, A67. DOI: 10.1051/0004-6361/201629115. arXiv: 1607.05563 (cit. on p. xi).

Consolandi, G. et al. (Feb. 2017). "Bars as seen by Herschel and Sloan". In: A&A 598, A114, A114. DOI: 10.1051/0004-6361/201629213. arXiv: 1701.00364 (cit. on pp. xii, 8).

Contopoulos, G. (Jan. 1980). "How far do bars extend". In: A&A 81, pp. 198–209 (cit. on pp. 26, 35, 67).

Contopoulos, G. and P. Grosbol (Nov. 1989). "Orbits in barred galaxies". In: A&A Rev. 1, pp. 261–289. DOI: 10.1007/BF00873080 (cit. on p. 26).

Contopoulos, G. and T. Papayannopoulos (Dec. 1980). "Orbits in weak and strong bars". In: A&A 92, pp. 33–46 (cit. on p. 26).

Contopoulos, G. and P. O. Vandervoort (Apr. 1992). "A rotating Staeckel potential". In: ApJ 389, pp. 118–128. DOI: 10.1086/171191 (cit. on p. 12).

Crain, R. A. et al. (June 2015). "The EAGLE simulations of galaxy formation: calibration of subgrid physics and model variations". In: MNRAS 450, pp. 1937–1961. DOI: 10.1093/mnras/stv725. arXiv: 1501.01311 (cit. on p. 29).

Crane, P. (Apr. 1975). "Surface photometry of galaxies. I - The SB0 NGC 2950". In: ApJ 197, pp. 317–319. DOI: 10.1086/153516 (cit. on p. 5).

Curir, A., P. Mazzei, and G. Murante (Feb. 2006). "Bar instability in cosmological halos". In: A&A 447, pp. 453–463. DOI: 10.1051/0004-6361:20053418. eprint: astro-ph/0510182 (cit. on p. 33).

Daddi, E. et al. (May 2010). "Different Star Formation Laws for Disks Versus Starbursts at Low and High Redshifts". In: ApJ 714, pp. L118–L122. DOI: 10.1088/2041-8205/714/1/L118. arXiv: 1003.3889 (cit. on p. 8).

de Vaucouleurs, G. (1959). "Classification and Morphology of External Galaxies." In: *Handbuch der Physik* 53, p. 275 (cit. on pp. xi, 2).

Debattista, V. P. and J. A. Sellwood (Nov. 2000). "Constraints from Dynamical Friction on the Dark Matter Content of Barred Galaxies". In: ApJ 543, pp. 704–721. DOI: 10.1086/317148. eprint: astro-ph/0006275 (cit. on pp. 30, 67).

Debattista, V. P. et al. (Apr. 2004). "Bulges or Bars from Secular Evolution?" In: ApJ 604, pp. L93–L96. DOI: 10.1086/386332. eprint: astro-ph/0402484 (cit. on p. 37).

Debattista, V. P. et al. (July 2006). "The Secular Evolution of Disk Structural Parameters". In: ApJ 645, pp. 209–227. DOI: 10.1086/504147. eprint: astro-ph/0509310 (cit. on pp. 37, 73, 108).

Ding, Hong-Qiang, Naoki Karasawa, and William A. Goddard (1992). "The reduced cell multipole method for Coulomb interactions in periodic systems with million-atom unit cells". In: *Chemical Physics Letters* 196.1, pp. 6 –10. ISSN: 0009-2614. DOI: https://doi.org/10.1016/0009-2614(92)85920-6. URL: http://www.sciencedirect.com/science/article/pii/0009261492859206 (cit. on p. 44).

Duval, M. F. and E. Athanassoula (May 1983). "Photometry, kinematics, and dynamics of the barred spiral galaxy NGC 5383". In: A&A 121, pp. 297–312 (cit. on p. 5).

Eddington, A. S. (Nov. 1916). "On the radiative equilibrium of the stars". In: MNRAS 77, pp. 16–35. DOI: 10.1093/mnras/77.1.16 (cit. on p. 48).

Efstathiou, G., G. Lake, and J. Negroponte (June 1982). "The stability and masses of disc galaxies". In: MNRAS 199, pp. 1069–1088. DOI: 10.1093/mnras/199.4.1069 (cit. on pp. 32, 33, 122).

Ellison, S. L. et al. (Sept. 2011). "The impact of gas inflows on star formation rates and metallicities in barred galaxies". In: MNRAS 416, pp. 2182–2192. DOI: 10.1111/j.1365-2966.2011.19195.x. arXiv: 1106.1177 (cit. on p. 8).

Elmegreen, B. G. and D. M. Elmegreen (Jan. 1985). "Properties of barred spiral galaxies". In: ApJ 288, pp. 438–455. DOI: 10.1086/162810 (cit. on p. 5).

Elmegreen, B. G. and D. M. Elmegreen (May 1990). "Optical tracers of spiral wave resonances in galaxies - Applications to NGC 1566". In: ApJ 355, pp. 52–58. DOI: 10.1086/168740 (cit. on p. 26).

Elmegreen, D. M. (1998). *Galaxies and galactic structure* (cit. on pp. xi, 7).

Elmegreen, D. M. et al. (Apr. 1991). "Properties and simulations of interacting spiral galaxies with transient 'ocular' shapes". In: A&A 244, pp. 52–63 (cit. on p. 39).

Emsellem, E. et al. (Jan. 2015). "The interplay between a galactic bar and a supermassive black hole: nuclear fuelling in a subparsec resolution galaxy simulation". In: MNRAS 446, pp. 2468–2482. DOI: 10.1093/mnras/stu2209. arXiv: 1410.6479 (cit. on pp. 8, 9).

Eskridge, P. B. et al. (Feb. 2000). "The Frequency of Barred Spiral Galaxies in the Near-Infrared". In: AJ 119, pp. 536–544. DOI: 10.1086/301203. eprint: astro-ph/9910479 (cit. on p. xii).

Evrard, A. E. (Dec. 1988). "Beyond N-body - 3D cosmological gas dynamics". In: MNRAS 235, pp. 911–934. DOI: 10.1093/mnras/235.3.911 (cit. on p. 46).

Ewald, P. P. (1921). "Die Berechnung optischer und elektrostatischer Gitterpotentiale". In: *Annalen der Physik* 369.3, pp. 253–287. DOI: 10.1002/andp.19213690304. eprint: https://onlinelibrary.wiley.com/doi/pdf/10.1002/andp.19213690304. URL: https://onlinelibrary.wiley.com/doi/abs/10.1002/andp.19213690304 (cit. on p. 44).

Fanali, R. et al. (Dec. 2015). "Bar formation as driver of gas inflows in isolated disc galaxies". In: MNRAS 454, pp. 3641–3652. DOI: 10.1093/mnras/stv2247. arXiv: 1509.08474 (cit. on pp. xii, 9).

Feldmann, R. et al. (Jan. 2010). "The Evolution of Central Group Galaxies in Hydrodynamical Simulations". In: ApJ 709, pp. 218–240. DOI: 10.1088/0004-637X/709/1/218. arXiv: 0906.3022 [astro-ph.CO] (cit. on p. 29).

Ferland, G. J. et al. (July 1998). "CLOUDY 90: Numerical Simulation of Plasmas and Their Spectra". In: PASP 110, pp. 761–778. DOI: 10.1086/316190 (cit. on p. 49).

Fiacconi, D., R. Feldmann, and L. Mayer (Jan. 2015). "The Argo simulation - II. The early build-up of the Hubble sequence". In: MNRAS 446, pp. 1957–1972. DOI: 10.1093/mnras/stu2228. arXiv: 1410.6818 (cit. on p. 73).

Font, J. et al. (Feb. 2017). "Kinematic Clues to Bar Evolution for Galaxies in the Local Universe: Why the Fastest Rotating Bars are Rotating Most Slowly". In: ApJ 835, 279, p. 279. DOI: 10.3847/1538-4357/835/2/279. arXiv: 1702.01743 (cit. on pp. 103, 104).

Friedli, D. (1999). "Birth, Aging, and Death of Galactic Bars". In: *The Evolution of Galaxies on Cosmological Timescales*. Ed. by J. E. Beckman and T. J. Mahoney. Vol. 187. Astronomical Society of the Pacific Conference Series, pp. 88–99. eprint: astro-ph/9903143 (cit. on p. 34).

Friedli, D. and W. Benz (Feb. 1993). "Secular evolution of isolated barred galaxies. I - Gravitational coupling between stellar bars and interstellar medium". In: A&A 268, pp. 65–85 (cit. on p. 37).

Fuchs, B. and E. Athanassoula (Dec. 2005). "Interaction between a galactic disk and a live dark halo with an anisotropic velocity distribution". In: A&A 444, pp. 455–459. DOI: 10.1051/0004-6361:20052894. eprint: astro-ph/0509902 (cit. on p. 67).

Gauthier, J.-R., J. Dubinski, and L. M. Widrow (Dec. 2006). "Substructure around M31: Evolution and Effects". In: ApJ 653, pp. 1180–1193. DOI: 10.1086/508860. eprint: astro-ph/0606015 (cit. on p. 33).

Gavazzi, G. et al. (Aug. 2015). "Hα3: an Hα imaging survey of HI selected galaxies from ALFALFA. VI. The role of bars in quenching star formation from z = 3 to the present epoch". In: A&A 580, A116, A116. DOI: 10.1051/0004-6361/201425351. arXiv: 1505.07836 (cit. on pp. xi, 8, 87, 104, 105, 110, 112).

Genzel, R. et al. (Oct. 2010). "A study of the gas-star formation relation over cosmic time". In: MNRAS 407, pp. 2091–2108. DOI: 10.1111/j.1365-2966.2010.16969.x. arXiv: 1003.5180 (cit. on p. 8).

Gerin, M., F. Combes, and E. Athanassoula (Apr. 1990). "The influence of galaxy interactions on stellar bars". In: A&A 230, pp. 37–54 (cit. on pp. 33, 38, 81, 111).

Ghigna, S. et al. (Oct. 1998). "Dark matter haloes with in clusters". In: MNRAS 300, pp. 146–162. DOI: 10.1046/j.1365-8711.1998.01918.x. eprint: astro-ph/9801192 (cit. on p. 78).

Gingold, R. A. and J. J. Monaghan (Nov. 1977). "Smoothed particle hydrodynamics - Theory and application to non-spherical stars". In: MNRAS 181, pp. 375–389 (cit. on pp. 41, 44).

Goldreich, P. and S. Tremaine (June 1978). "The excitation and evolution of density waves". In: ApJ 222, pp. 850–858. DOI: 10.1086/156203 (cit. on p. 32).

Goldreich, P. and S. Tremaine (Nov. 1979). "The excitation of density waves at the Lindblad and corotation resonances by an external potential". In: ApJ 233, pp. 857–871. DOI: 10.1086/157448 (cit. on p. 32).

Goldreich, P. and S. Tremaine (Feb. 1981). "The origin of the eccentricities of the rings of Uranus". In: ApJ 243, pp. 1062–1075. DOI: 10.1086/158671 (cit. on p. 26).

Goulding, A. D. et al. (July 2017). "Galaxy-scale Bars in Late-type Sloan Digital Sky Survey Galaxies Do Not Influence the Average Accretion Rates of Supermassive Black Holes". In: ApJ 843, 135, p. 135. DOI: 10.3847/1538-4357/aa755b. arXiv: 1705.08895 (cit. on p. 9).

Governato, F. et al. (Feb. 2007). "Forming disc galaxies in ΛCDM simulations". In: MNRAS 374, pp. 1479–1494. DOI: 10.1111/j.1365-2966.2006.11266.x. eprint: astro-ph/0602351 (cit. on pp. 29, 33).

Goz, D. et al. (Feb. 2015). "Properties of barred spiral discs in hydrodynamical cosmological simulations". In: MNRAS 447, pp. 1774–1788. DOI: 10.1093/mnras/stu2557 (cit. on pp. 29, 34).

Grosbøl, P., P. A. Patsis, and E. Pompei (Sept. 2004). "Spiral galaxies observed in the near-infrared K band. I. Data analysis and structural parameters". In: A&A 423, pp. 849–859. DOI: 10.1051/0004-6361:20035804 (cit. on p. 9).

Guedes, J. et al. (Dec. 2011). "Forming Realistic Late-type Spirals in a ΛCDM Universe: The Eris Simulation". In: ApJ 742, 76, p. 76. DOI: 10.1088/0004-637X/742/2/76. arXiv: 1103.6030 (cit. on pp. 28, 46, 47).

Guedes, J. et al. (July 2013). "Pseudobulge Formation as a Dynamical Rather than a Secular Process". In: ApJ 772, 36, p. 36. DOI: 10.1088/0004-637X/772/1/36. arXiv: 1211.1713 (cit. on pp. 72, 73, 82, 92, 108).

Haardt, F. and P. Madau (Apr. 1996). "Radiative Transfer in a Clumpy Universe. II. The Ultraviolet Extragalactic Background". In: ApJ 461, p. 20. DOI: 10.1086/177035. eprint: astro-ph/9509093 (cit. on pp. 47, 49, 51, 55).

Haardt, F. and P. Madau (Feb. 2012). "Radiative Transfer in a Clumpy Universe. IV. New Synthesis Models of the Cosmic UV/X-Ray Background". In: ApJ 746, 125, p. 125. DOI: 10.1088/0004-637X/746/2/125. arXiv: 1105.2039 (cit. on pp. 49, 51).

Hakobyan, A. A. et al. (Mar. 2016). "Supernovae and their host galaxies - III. The impact of bars and bulges on the radial distribution of supernovae in disc galaxies". In: MNRAS 456, pp. 2848–2860. DOI: 10.1093/mnras/stv2853. arXiv: 1511.08896 (cit. on p. xii).

Hammer, F. et al. (Dec. 2009). "The Hubble sequence: just a vestige of merger events?" In: A&A 507, pp. 1313–1326. DOI: 10.1051/0004-6361/200912115. arXiv: 0903.3962 (cit. on p. 109).

Hasan, H. and C. Norman (Sept. 1990). "Chaotic orbits in barred galaxies with central mass concentrations". In: ApJ 361, pp. 69–77. DOI: 10.1086/169168 (cit. on p. 37).

Hasan, H., D. Pfenniger, and C. Norman (May 1993). "Galactic bars with central mass concentrations - Three-dimensional dynamics". In: ApJ 409, pp. 91–109. DOI: 10.1086/172644 (cit. on p. 37).

Hernandez, O. et al. (July 2005). "BHαBAR: big Hα kinematical sample of barred spiral galaxies - I. Fabry-Perot observations of 21 galaxies". In: MNRAS 360, pp. 1201–1230. DOI: 10.1111/j.1365-2966.2005.09125.x. eprint: astro-ph/0504393 (cit. on p. 7).

Hernquist, L. and N. Katz (June 1989). "TREESPH - A unification of SPH with the hierarchical tree method". In: ApJS 70, pp. 419–446. DOI: 10.1086/191344 (cit. on p. 45).

Ho, L. C., A. V. Filippenko, and W. L. W. Sargent (Oct. 1997). "The Influence of Bars on Nuclear Activity". In: ApJ 487, pp. 591–602. DOI: 10.1086/304643. eprint: astro-ph/9704100 (cit. on p. xii).

Hohl, F. (Sept. 1971). "Numerical Experiments with a Disk of Stars". In: ApJ 168, p. 343. DOI: 10.1086/151091 (cit. on pp. 27, 33).

Holmes, L. et al. (Aug. 2015). "The incidence of bar-like kinematic flows in CALIFA galaxies". In: MNRAS 451, pp. 4397–4411. DOI: 10.1093/mnras/stv1254. arXiv: 1506.01378 (cit. on pp. 6, 7).

Hoyle, F. and R. A. Lyttleton (1939). "The effect of interstellar matter on climatic variation". In: *Proceedings of the Cambridge Philosophical Society* 35, p. 405. DOI: 10.1017/S0305004100021150 (cit. on p. 47).

Hozumi, S. and L. Hernquist (Aug. 1999). "Secular Evolution of Barred Galaxies with Central Massive Black Holes". In: *Galaxy Dynamics - A Rutgers Symposium*. Ed. by D. R. Merritt, M. Valluri, and J. A. Sellwood. Vol. 182. Astronomical Society of the Pacific Conference Series (cit. on p. 37).

Hubble, E. P. (Dec. 1926). "Extragalactic nebulae." In: ApJ 64. DOI: 10.1086/143018 (cit. on p. 1).

Hubble, E. P. (1936). *Realm of the Nebulae*. Yale University Press (cit. on pp. xi, 1).

Hummel, E. et al. (Sept. 1990). "Environmental impact on the nuclear radio activity in spiral galaxies". In: A&A 236, pp. 333–345 (cit. on p. 8).

Hunt, L. K. and M. A. Malkan (May 1999). "Morphology of the 12 Micron Seyfert Galaxies. I. Hubble Types, Axial Ratios, Bars, and Rings". In: ApJ 516, pp. 660–671. DOI: 10.1086/307150. eprint: astro-ph/9901410 (cit. on p. xii).

Husemann, B. et al. (Jan. 2013). "CALIFA, the Calar Alto Legacy Integral Field Area survey. II. First public data release". In: A&A 549, A87, A87. DOI: 10.1051/0004-6361/201220582. arXiv: 1210.8150 [astro-ph.CO] (cit. on p. 7).

Iannuzzi, F. and E. Athanassoula (July 2015). "2D kinematic signatures of boxy/peanut bulges". In: MNRAS 450, pp. 2514–2538. DOI: 10.1093/mnras/stv764. arXiv: 1504.00010 (cit. on p. 70).

Jetley, P. et al. (Apr. 2008). "Massively parallel cosmological simulations with ChaNGa". In: *2008 IEEE International Symposium on Parallel and Distributed Processing*, pp. 1–12. DOI: 10.1109/IPDPS.2008.4536319 (cit. on pp. 28, 46).

Jetley, Pritish et al. (2010). "Scaling Hierarchical N-body Simulations on GPU Clusters". In: *Proceedings of the 2010 ACM/IEEE International Conference for High Performance Computing, Networking, Storage and Analysis*. SC '10. Washington, DC, USA: IEEE Computer Society, pp. 1–11. ISBN: 978-1-4244-7559-9. DOI: 10.1109/SC.2010.49. URL: https://doi.org/10.1109/SC.2010.49 (cit. on pp. 28, 46).

Jogee, S. (2006). "The Fueling and Evolution of AGN: Internal and External Triggers". In: *Physics of Active Galactic Nuclei at all Scales*. Ed. by D. Alloin. Vol. 693. Lecture Notes in Physics, Berlin Springer Verlag, p. 143. DOI: 10.1007/3-540-34621-X_6. eprint: astro-ph/0408383 (cit. on p. 8).

Jogee, S., N. Scoville, and J. D. P. Kenney (Sept. 2005). "The Central Region of Barred Galaxies: Molecular Environment, Starbursts, and Secular Evolution". In: ApJ 630, pp. 837–863. DOI: 10.1086/432106. eprint: astro-ph/0402341 (cit. on p. xii).

Khoperskov, S. et al. (Jan. 2018). "Bar quenching in gas-rich galaxies". In: A&A 609, A60, A60. DOI: 10.1051/0004-6361/201731211. arXiv: 1709.03604 (cit. on p. 8).

Kim, W.-T. et al. (Mar. 2012). "Central Regions of Barred Galaxies: Two-dimensional Non-self-gravitating Hydrodynamic Simulations". In: ApJ 747, 60, p. 60. DOI: 10.1088/0004-637X/747/1/60. arXiv: 1112.6055 (cit. on p. 9).

Klypin, A. et al. (Sept. 2009). "Dynamics of barred galaxies: effects of disc height". In: MNRAS 398, pp. 1027–1040. DOI: 10.1111/j.1365-2966.2009.15187.x. arXiv: 0808.3422 (cit. on p. 32).

Knapen, J. H. (2007). "Barred Galaxies and Galaxy Evolution". In: *Astrophysics and Space Science Proceedings* 3, p. 175. DOI: 10.1007/978-1-4020-5573-7_29 (cit. on p. 9).

Kormendy, J. (Dec. 1983). "The stellar kinematics and dynamics of barred galaxies. I NGC 936". In: ApJ 275, pp. 529–548. DOI: 10.1086/161552 (cit. on p. 6).

Kormendy, J. (1993). "Kinematics of extragalactic bulges: evidence that some bulges are really disks". In: *Galactic Bulges*. Ed. by H. Dejonghe and H. J. Habing. Vol. 153. IAU Symposium, p. 209 (cit. on p. 9).

Kormendy, J. (Oct. 2013). "Secular Evolution in Disk Galaxies". In: *Secular Evolution of Galaxies*. Cambridge University Press, p. 1 (cit. on pp. xi, xii, 7).

Kormendy, J. and M. E. Cornell (Jan. 2004). "Secular Evolution And The Growth of Pseudobulges In Disk Galaxies". In: *Penetrating Bars Through Masks of Cosmic Dust*. Ed. by D. L. Block et al. Vol. 319. Astrophysics and Space Science Library, p. 261. DOI: 10.1007/978-1-4020-2862-5_24. eprint: astro-ph/0407434 (cit. on p. 9).

Kormendy, J. and R. C. Kennicutt Jr. (Sept. 2004). "Secular Evolution and the Formation of Pseudobulges in Disk Galaxies". In: ARA&A 42, pp. 603–683. DOI: 10.1146/annurev.astro.42.053102.134024. eprint: astro-ph/0407343 (cit. on pp. xi, 4, 9).

Kraljic, K., F. Bournaud, and M. Martig (Sept. 2012). "The Two-phase Formation History of Spiral Galaxies Traced by the Cosmic Evolution of the Bar Fraction". In: ApJ 757, 60, p. 60. DOI: 10.1088/0004-637X/757/1/60. arXiv: 1207.0351 (cit. on pp. 28, 29, 34).

Kron, R. G. (June 1980). "Photometry of a complete sample of faint galaxies". In: ApJS 43, pp. 305–325. DOI: 10.1086/190669 (cit. on pp. 49, 86).

Kroupa, P. (Apr. 2001). "On the variation of the initial mass function". In: MNRAS 322, pp. 231–246. DOI: 10.1046/j.1365-8711.2001.04022.x. eprint: astro-ph/0009005 (cit. on pp. 49–51, 110).

Kroupa, P., C. A. Tout, and G. Gilmore (June 1993). "The distribution of low-mass stars in the Galactic disc". In: MNRAS 262, pp. 545–587. DOI: 10.1093/mnras/262.3.545 (cit. on pp. 47, 50, 51, 110).

Krumholz, M. R. and C. F. McKee (Sept. 2005). "A General Theory of Turbulence-regulated Star Formation, from Spirals to Ultraluminous Infrared Galaxies". In: ApJ 630, pp. 250–268. DOI: 10.1086/431734. eprint: astro-ph/0505177 (cit. on p. 8).

Krumholz, M. R., C. F. McKee, and J. Tumlinson (July 2009). "The Star Formation Law in Atomic and Molecular Gas". In: ApJ 699, pp. 850–856. DOI: 10.1088/0004-637X/699/1/850. arXiv: 0904.0009 [astro-ph.GA] (cit. on p. 8).

Kuijken, K. and M. R. Merrifield (Apr. 1995). "Establishing the connection between peanut-shaped bulges and galactic bars". In: ApJ 443, pp. L13–L16. DOI: 10.1086/187824. eprint: astro-ph/9501114 (cit. on p. 36).

Lang, M., K. Holley-Bockelmann, and M. Sinha (Aug. 2014). "Bar Formation from Galaxy Flybys". In: ApJ 790, L33, p. L33. DOI: 10.1088/2041-8205/790/2/L33. arXiv: 1405.5832 (cit. on p. 111).

Laurikainen, E., H. Salo, and R. Buta (May 2004). "Comparison of Bar Strengths and Fractions of Bars in Active and Nonactive Galaxies". In: ApJ 607, pp. 103–124. DOI: 10.1086/383462. eprint: astro-ph/0111376 (cit. on pp. xi, xii).

Lee, G.-H. et al. (May 2012). "Do Bars Trigger Activity in Galactic Nuclei?" In: ApJ 750, 141, p. 141. DOI: 10.1088/0004-637X/750/2/141. arXiv: 1203.1693 (cit. on p. xi).

Li, C. et al. (Aug. 2009). "The clustering of barred galaxies in the local Universe". In: MNRAS 397, pp. 726–732. DOI: 10.1111/j.1365-2966.2009.15028.x. arXiv: 0902.1175 (cit. on pp. 33, 72).

Lin, Y. et al. (Dec. 2014). "The Environment of Barred Galaxies in the Low-redshift Universe". In: ApJ 796, 98, p. 98. DOI: 10.1088/0004-637X/796/2/98. arXiv: 1405.6768 (cit. on pp. 33, 72, 109).

Łokas, E. L. et al. (Aug. 2016). "Tidally Induced Bars of Galaxies in Clusters". In: ApJ 826, 227, p. 227. DOI: 10.3847/0004-637X/826/2/227. arXiv: 1601.07433 (cit. on pp. 33, 111).

Lucy, L. B. (Dec. 1977). "A numerical approach to the testing of the fission hypothesis". In: AJ 82, pp. 1013–1024. DOI: 10.1086/112164 (cit. on pp. 41, 44).

Lupi, A., M. Volonteri, and J. Silk (Sept. 2017). "Simplified galaxy formation with mesh-less hydrodynamics". In: MNRAS 470, pp. 1673–1686. DOI: 10.1093/mnras/stx1313. arXiv: 1705.09285 (cit. on p. 86).

Lütticke, R., R.-J. Dettmar, and M. Pohlen (Oct. 2000). "Box- and peanut-shaped bulges. II. NIR observations". In: A&A 362, pp. 435–446. eprint: astro-ph/0008478 (cit. on pp. xii, 36).

Lynden-Bell, D. and A. J. Kalnajs (1972). "On the generating mechanism of spiral structure". In: MNRAS 157, p. 1. DOI: 10.1093/mnras/157.1.1 (cit. on pp. xi, 35, 67).

Maiolino, R. et al. (Mar. 2000). "Discovery of a Nuclear Gas Bar Feeding the Active Nucleus in Circinus". In: ApJ 531, pp. 219–231. DOI: 10.1086/308444. eprint: astro-ph/9910160 (cit. on p. 9).

Martinet, L. and D. Friedli (July 1997). "Bar strength and star formation activity in late-type barred galaxies." In: A&A 323, pp. 363–373. eprint: astro-ph/9701091 (cit. on p. xii).

Martinez-Valpuesta, I., J. Aguerri, and C. González-García (May 2016). "Characterization of Bars Induced by Interactions". In: *Galaxies* 4, p. 7. DOI: 10.3390/galaxies4020007 (cit. on p. 33).

Martinez-Valpuesta, I. and I. Shlosman (Sept. 2004). "Why Buckling Stellar Bars Weaken in Disk Galaxies". In: ApJ 613, pp. L29–L32. DOI: 10.1086/424876. eprint: astro-ph/0408241 (cit. on p. 37).

Martinez-Valpuesta, I., I. Shlosman, and C. Heller (Jan. 2006). "Evolution of Stellar Bars in Live Axisymmetric Halos: Recurrent Buckling and Secular Growth". In: ApJ 637, pp. 214–226. DOI: 10.1086/498338. eprint: astro-ph/0507219 (cit. on pp. 37, 95, 98).

Mashchenko, S., J. Wadsley, and H. M. P. Couchman (Jan. 2008). "Stellar Feedback in Dwarf Galaxy Formation". In: *Science* 319, p. 174. DOI: 10.1126/science.1148666. arXiv: 0711.4803 (cit. on p. 50).

Masters, K. L. et al. (Mar. 2011). "Galaxy Zoo: bars in disc galaxies". In: MNRAS 411, pp. 2026–2034. DOI: 10.1111/j.1365-2966.2010.17834.x. arXiv: 1003.0449 (cit. on p. xi).

Mayer, L. and J. Wadsley (Jan. 2004). "The formation and evolution of bars in low surface brightness galaxies with cold dark matter haloes". In: MNRAS 347, pp. 277–294. DOI: 10.1111/j.1365-2966.2004.07202.x. eprint: astro-ph/0303239 (cit. on p. 33).

McKee, C. F. and J. P. Ostriker (Nov. 1977). "A theory of the interstellar medium - Three components regulated by supernova explosions in an inhomogeneous substrate". In: ApJ 218, pp. 148–169. DOI: 10.1086/155667 (cit. on pp. 49, 50).

Melvin, T. et al. (Mar. 2014). "Galaxy Zoo: an independent look at the evolution of the bar fraction over the last eight billion years from HST-COSMOS". In: MNRAS 438, pp. 2882–2897. DOI: 10.1093/mnras/stt2397. arXiv: 1401.3334 (cit. on p. 109).

Menéndez-Delmestre, K. et al. (Mar. 2007). "A Near-Infrared Study of 2MASS Bars in Local Galaxies: An Anchor for High-Redshift Studies". In: ApJ 657, pp. 790–804. DOI: 10.1086/511025. eprint: astro-ph/0611540 (cit. on p. xii).

Menon, H. et al. (Mar. 2015). "Adaptive techniques for clustered N-body cosmological simulations". In: *Computational Astrophysics and Cosmology* 2, 1, p. 1. DOI: 10.1186/s40668-015-0007-9. arXiv: 1409.1929 [astro-ph.IM] (cit. on pp. 28, 41, 46, 55, 112).

Miller, R. H., K. H. Prendergast, and W. J. Quirk (Sept. 1970). "Numerical Experiments on Spiral Structure". In: ApJ 161, p. 903. DOI: 10.1086/150593 (cit. on p. 27).

Mo, H., F. C. van den Bosch, and S. White (May 2010). *Galaxy Formation and Evolution* (cit. on p. 4).

Moetazedian, R. et al. (Aug. 2017). "Effects of galaxy-satellite interactions on bar formation". In: A&A 604, A75, A75. DOI: 10.1051/0004-6361/201630024. arXiv: 1703.06002 (cit. on pp. 33, 72, 73, 75, 108).

Monaghan, J. J. (1992). "Smoothed particle hydrodynamics". In: ARA&A 30, pp. 543–574. DOI: 10.1146/annurev.aa.30.090192.002551 (cit. on p. 43).

Nair, P. B. and R. G. Abraham (May 2010). "On the Fraction of Barred Spiral Galaxies". In: ApJ 714, pp. L260–L264. DOI: 10.1088/2041-8205/714/2/L260. arXiv: 1004.0684 (cit. on p. xi).

Navarro, J. F. and W. Benz (Oct. 1991). "Dynamics of cooling gas in galactic dark halos". In: ApJ 380, pp. 320–329. DOI: 10.1086/170590 (cit. on p. 28).

Noguchi, M. (Oct. 1987). "Close encounter between galaxies. II - Tidal deformation of a disc galaxy stabilized by massive halo". In: MNRAS 228, pp. 635–651. DOI: 10.1093/mnras/228.3.635 (cit. on p. 33).

Noguchi, M. (Sept. 1988). "Gas dynamics in interacting disc galaxies - Fuelling of nuclei by induced bars". In: A&A 203, pp. 259–272 (cit. on p. 8).

Norman, C. and H. Hasan (1990). "Chaotic orbits in barred structures with central mass concentration." In: *Dynamics and Interactions of Galaxies*. Ed. by R. Wielen, pp. 479–482 (cit. on p. 26).

Norman, C. A., J. A. Sellwood, and H. Hasan (May 1996). "Bar Dissolution and Bulge Formation: an Example of Secular Dynamical Evolution in Galaxies". In: ApJ 462, p. 114. DOI: 10.1086/177133 (cit. on p. 37).

Okamoto, T., M. Isoe, and A. Habe (Aug. 2015). "Cosmic evolution of bars in simulations of galaxy formation". In: PASJ 67, 63, p. 63. DOI: 10.1093/pasj/psv037. arXiv: 1410.0442 (cit. on pp. 29, 34).

Ostriker, J. P. and P. J. E. Peebles (Dec. 1973). "A Numerical Study of the Stability of Flattened Galaxies: or, can Cold Galaxies Survive?" In: ApJ 186, pp. 467–480. DOI: 10.1086/152513 (cit. on pp. 27, 32, 33).

Patsis, P. A. and M. Katsanikas (Dec. 2014). "The phase space of boxy-peanut and X-shaped bulges in galaxies - I. Properties of non-periodic orbits". In: MNRAS 445, pp. 3525–3545. DOI: 10.1093/mnras/stu1988. arXiv: 1410.4921 [nlin.CD] (cit. on p. 36).

Patsis, P. A., C. Skokos, and E. Athanassoula (June 2003). "Orbital dynamics of three-dimensional bars - IV. Boxy isophotes in face-on views". In: MNRAS 342, pp. 69–78. DOI: 10.1046/j.1365-8711.2003.06511.x. eprint: astro-ph/0302198 (cit. on p. 36).

Peschken, N. and E. L. Łokas (Apr. 2018). "Tidally induced bars in Illustris galaxies". In: *ArXiv e-prints*. arXiv: 1804.06241 (cit. on pp. 29, 33, 34, 38, 39, 81, 109, 111, 112).

Pettitt, A. R. and J. W. Wadsley (Mar. 2018). "Bars and spirals in tidal interactions with an ensemble of galaxy mass models". In: MNRAS 474, pp. 5645–5671. DOI: 10.1093/mnras/stx3129. arXiv: 1712.00882 (cit. on p. 33).

Pfenniger, D. and D. Friedli (Dec. 1991). "Structure and dynamics of 3D N-body barred galaxies". In: A&A 252, pp. 75–93 (cit. on p. 27).

Piner, B. G., J. M. Stone, and P. J. Teuben (Aug. 1995). "Nuclear Rings and Mass Inflow in Hydrodynamic Simulations of Barred Galaxies". In: ApJ 449, p. 508. DOI: 10.1086/176075 (cit. on p. 9).

Pontzen, A. et al. (Feb. 2017). "How to quench a galaxy". In: MNRAS 465, pp. 547–558. DOI: 10.1093/mnras/stw2627. arXiv: 1607.02507 (cit. on p. 58).

Press, William H. et al. (1993). *Numerical Recipes in FORTRAN; The Art of Scientific Computing*. 2nd. New York, NY, USA: Cambridge University Press. ISBN: 0521437164 (cit. on p. 115).

Raha, N. et al. (Aug. 1991). "A dynamical instability of bars in disk galaxies". In: Nature 352, p. 411. DOI: 10.1038/352411a0 (cit. on pp. 36, 37, 95).

Rautiainen, P. and H. Salo (Oct. 2000). "N-body simulations of resonance rings in galactic disks". In: A&A 362, pp. 465–586 (cit. on p. 9).

Reese, A. S. et al. (June 2007). "Photometric Decomposition of Barred Galaxies". In: AJ 133, pp. 2846–2858. DOI: 10.1086/516826. eprint: astro-ph/0702720 (cit. on p. 7).

Regan, M. W. and P. Teuben (Jan. 2003). "The Formation of Nuclear Rings in Barred Spiral Galaxies". In: ApJ 582, pp. 723–742. DOI: 10.1086/344721. eprint: astro-ph/0210244 (cit. on p. 9).

Roberts Jr., W. W., J. M. Huntley, and G. D. van Albada (Oct. 1979). "Gas dynamics in barred spirals - Gaseous density waves and galactic shocks". In: ApJ 233, pp. 67–84. DOI: 10.1086/157367 (cit. on p. xii).

Robertson, B. et al. (May 2004). "Disk Galaxy Formation in a Λ Cold Dark Matter Universe". In: ApJ 606, pp. 32–45. DOI: 10.1086/382871. eprint: astro-ph/0401252 (cit. on p. 29).

Rodionov, S. A., E. Athanassoula, and N. Peschken (Mar. 2017). "Forming disk galaxies in major mergers. II. The central mass concentration problem and a comparison of GADGET3 with GIZMO". In: A&A 600, A25, A25. DOI: 10.1051/0004-6361/201628319. arXiv: 1701.02685 (cit. on p. 48).

Romano-Díaz, E. et al. (Nov. 2008). "Disk Evolution and Bar Triggering Driven by Interactions with Dark Matter Substructure". In: ApJ 687, L13, p. L13. DOI: 10.1086/593168. arXiv: 0809.2785 (cit. on pp. 28, 29, 33, 34, 111).

Sakamoto, K. et al. (Nov. 1999). "Bar-driven Transport of Molecular Gas to Galactic Centers and Its Consequences". In: ApJ 525, pp. 691–701. DOI: 10.1086/307910. eprint: astro-ph/9906454 (cit. on p. 9).

Sanders, R. H. and J. M. Huntley (Oct. 1976). "Gas response to oval distortions in disk galaxies". In: ApJ 209, pp. 53–65. DOI: 10.1086/154692 (cit. on p. xii).

Scannapieco, C. and E. Athanassoula (Sept. 2012). "Bars in hydrodynamical cosmological simulations". In: MNRAS 425, pp. L10–L14. DOI: 10.1111/j.1745-3933.2012.01291.x. arXiv: 1206.5308 (cit. on pp. 28, 29, 34).

Scannapieco, C. et al. (June 2009). "The formation and survival of discs in a ΛCDM universe". In: MNRAS 396, pp. 696–708. DOI: 10.1111/j.1365-2966.2009.14764.x. arXiv: 0812.0976 (cit. on p. 29).

Schaye, J. et al. (Jan. 2015). "The EAGLE project: simulating the evolution and assembly of galaxies and their environments". In: MNRAS 446, pp. 521–554. DOI: 10.1093/mnras/stu2058. arXiv: 1407.7040 (cit. on p. 29).

Sellwood, J. A. (Sept. 1980). "Galaxy models with live halos". In: A&A 89, pp. 296–307 (cit. on p. 27).

Sellwood, J. A. (June 1981). "Bar instability and rotation curves". In: A&A 99, pp. 362–374 (cit. on pp. 27, 32).

Sellwood, J. A. (2013). "Dynamics of Disks and Warps". In: *Planets, Stars and Stellar Systems. Volume 5: Galactic Structure and Stellar Populations*. Ed. by T. D. Oswalt and G. Gilmore, p. 923. DOI: 10.1007/978-94-007-5612-0_18 (cit. on p. 32).

Sellwood, J. A. (Jan. 2014). "Secular evolution in disk galaxies". In: *Reviews of Modern Physics* 86, pp. 1–46. DOI: 10.1103/RevModPhys.86.1. arXiv: 1310.0403 (cit. on pp. 7, 33).

Sellwood, J. A. and R. Z. Sánchez (June 2010). "Quantifying non-circular streaming motions in disc galaxies". In: MNRAS 404, pp. 1733–1744. DOI: 10.1111/j.1365-2966.2010.16430.x. arXiv: 0912.5493 (cit. on p. 7).

Sellwood, J. A. and A. Wilkinson (Feb. 1993). "Dynamics of barred galaxies". In: *Reports on Progress in Physics* 56, pp. 173–256. DOI: 10.1088/0034-4885/56/2/001. eprint: astro-ph/0608665 (cit. on pp. 9, 16).

Sérsic, J. L. (1963). "Influence of the atmospheric and instrumental dispersion on the brightness distribution in a galaxy". In: *Boletin de la Asociacion Argentina de Astronomia La Plata Argentina* 6, p. 41 (cit. on pp. 52, 66, 115).

Sérsic, J. L. (1968). *Atlas de Galaxias Australes*. Observatorio Astronomico de Cordoba (cit. on pp. 52, 115).

Shen, J. and J. A. Sellwood (Apr. 2004). "The Destruction of Bars by Central Mass Concentrations". In: ApJ 604, pp. 614–631. DOI: 10.1086/382124. eprint: astro-ph/0310194 (cit. on p. 37).

Shen, S., J. Wadsley, and G. Stinson (Sept. 2010). "The enrichment of the intergalactic medium with adiabatic feedback - I. Metal cooling and metal diffusion". In: MNRAS 407, pp. 1581–1596. DOI: 10.1111/j.1365-2966.2010.17047.x. arXiv: 0910.5956 (cit. on pp. 49, 50).

Shen, S. et al. (Mar. 2013). "The Circumgalactic Medium of Massive Galaxies at z ~ 3: A Test for Stellar Feedback, Galactic Outflows, and Cold Streams". In: ApJ 765, 89, p. 89. DOI: 10.1088/0004-637X/765/2/89. arXiv: 1205.0270 (cit. on pp. 49, 50).

Sheth, K. et al. (Oct. 2005). "Secular Evolution via Bar-driven Gas Inflow: Results from BIMA SONG". In: ApJ 632, pp. 217–226. DOI: 10.1086/432409. eprint: astro-ph/0505393 (cit. on p. 9).

Sheth, K. et al. (Mar. 2008). "Evolution of the Bar Fraction in COSMOS: Quantifying the Assembly of the Hubble Sequence". In: ApJ 675, pp. 1141–1155. DOI: 10.1086/524980. arXiv: 0710.4552 (cit. on p. 109).

Shlosman, I., M. C. Begelman, and J. Frank (June 1990). "The fuelling of active galactic nuclei". In: Nature 345, pp. 679–686. DOI: 10.1038/345679a0 (cit. on p. 8).

Shlosman, I., J. Frank, and M. C. Begelman (Mar. 1989). "Bars within bars - A mechanism for fuelling active galactic nuclei". In: Nature 338, pp. 45–47. DOI: 10.1038/338045a0 (cit. on p. 9).

Silk, J. and G. A. Mamon (Aug. 2012). "The current status of galaxy formation". In: *Research in Astronomy and Astrophysics* 12, pp. 917–946. DOI: 10.1088/1674-4527/12/8/004. arXiv: 1207.3080 [astro-ph.CO] (cit. on p. 28).

Simkin, S. M., H. J. Su, and M. P. Schwarz (Apr. 1980). "Nearby Seyfert galaxies". In: ApJ 237, pp. 404–413. DOI: 10.1086/157882 (cit. on p. 8).

Simmons, B. D. et al. (Dec. 2014). "Galaxy Zoo: CANDELS barred discs and bar fractions". In: MNRAS 445, pp. 3466–3474. DOI: 10.1093/mnras/stu1817. arXiv: 1409.1214 (cit. on p. 109).

Skibba, R. A. et al. (June 2012). "Galaxy Zoo: the environmental dependence of bars and bulges in disc galaxies". In: MNRAS 423, pp. 1485–1502. DOI: 10.1111/j.1365-2966.2012.20972.x. arXiv: 1111.0969 [astro-ph.CO] (cit. on p. 33).

Sokołowska, A. et al. (Mar. 2016). "Diffuse Coronae in Cosmological Simulations of Milky Way-sized Galaxies". In: ApJ 819, 21, p. 21. DOI: 10.3847/0004-637X/819/1/21. arXiv: 1504.04620 (cit. on pp. 46, 50, 51, 75).

Sokołowska, A. et al. (Feb. 2017). "Galactic Angular Momentum in Cosmological Zoom-in Simulations. I. Disk and Bulge Components and the Galaxy-Halo Connection". In: ApJ 835, 289, p. 289. DOI: 10.3847/1538-4357/835/2/289. arXiv: 1612.07362 (cit. on pp. 29, 34, 46, 51, 75, 110).

Sormani, M. C., J. Binney, and J. Magorrian (May 2015). "Gas flow in barred potentials". In: MNRAS 449, pp. 2421–2435. DOI: 10.1093/mnras/stv441. arXiv: 1502.02740 (cit. on p. 9).

Sotnikova, N. Y. and S. A. Rodionov (Jan. 2005). "Bending Instability of Stellar Disks: The Stabilizing Effect of a Compact Bulge". In: *Astronomy Letters* 31,

pp. 15–29. DOI: 10.1134/1.1854793. eprint: astro-ph/0412063 (cit. on p. 95).

Spekkens, K. and J. A. Sellwood (July 2007). "Modeling Noncircular Motions in Disk Galaxies: Application to NGC 2976". In: ApJ 664, pp. 204–214. DOI: 10.1086/518471. eprint: astro-ph/0703688 (cit. on p. 7).

Spergel, D. N. et al. (June 2007). "Three-Year Wilkinson Microwave Anisotropy Probe (WMAP) Observations: Implications for Cosmology". In: ApJS 170, pp. 377–408. DOI: 10.1086/513700. eprint: astro-ph/0603449 (cit. on p. 47).

Spinoso, D. et al. (Mar. 2017). "Bar-driven evolution and quenching of spiral galaxies in cosmological simulations". In: MNRAS 465, pp. 3729–3740. DOI: 10.1093/mnras/stw2934. arXiv: 1607.02141 (cit. on pp. 29, 30, 34, 48, 54, 57, 64, 73, 75, 98, 108).

Springel, V. et al. (Dec. 2008). "The Aquarius Project: the subhaloes of galactic haloes". In: MNRAS 391, pp. 1685–1711. DOI: 10.1111/j.1365-2966.2008.14066.x. arXiv: 0809.0898 (cit. on p. 72).

Stadel, J. G. (2001). "Cosmological N-body simulations and their analysis". PhD thesis. UNIVERSITY OF WASHINGTON (cit. on pp. 28, 47).

Stinson, G. et al. (Dec. 2006). "Star formation and feedback in smoothed particle hydrodynamic simulations - I. Isolated galaxies". In: MNRAS 373, pp. 1074–1090. DOI: 10.1111/j.1365-2966.2006.11097.x. eprint: astro-ph/0602350 (cit. on pp. 47, 49–51, 55).

Sundin, M., K. J. Donner, and B. Sundelius (Dec. 1993). "Change in angular velocity of perturbed galactic bars". In: A&A 280, pp. 105–116 (cit. on p. 38).

Sundin, M. and B. Sundelius (May 1991). "Unexpected behaviour in the rotation of perturbed barred galaxies". In: A&A 245, pp. L5–L8 (cit. on p. 38).

Toomre, A. (May 1964). "On the gravitational stability of a disk of stars". In: ApJ 139, pp. 1217–1238. DOI: 10.1086/147861 (cit. on pp. 32, 100).

Toomre, A. (1966). "On the Coupling of the Earth's Core and Mantle during the 26,000-Year Precession". In: *The Earth-Moon System*. Ed. by B. G. Marsden and A. G. W. Cameron. Vol. 65, p. 33 (cit. on p. 37).

Toomre, A. (1981). "What amplifies the spirals". In: *Structure and Evolution of Normal Galaxies*. Ed. by S. M. Fall and D. Lynden-Bell, pp. 111–136 (cit. on pp. 32, 100).

Tremaine, S. and M. D. Weinberg (July 1984). "A kinematic method for measuring the pattern speed of barred galaxies". In: ApJ 282, pp. L5–L7. DOI: 10.1086/184292 (cit. on pp. xi, 7, 35).

Valenzuela, O. and A. Klypin (Oct. 2003). "Secular bar formation in galaxies with a significant amount of dark matter". In: MNRAS 345, pp. 406–422. DOI: 10.1046/j.1365-8711.2003.06947.x. eprint: astro-ph/0204028 (cit. on pp. 30, 67).

Vogelsberger, M. et al. (Oct. 2014). "Introducing the Illustris Project: simulating the coevolution of dark and visible matter in the Universe". In: MNRAS 444, pp. 1518–1547. DOI: 10.1093/mnras/stu1536. arXiv: 1405.2921 (cit. on pp. 29, 34, 39).

Wadsley, J. W., J. Stadel, and T. Quinn (Feb. 2004). "Gasoline: a flexible, parallel implementation of TreeSPH". In: New A 9, pp. 137–158. DOI: 10.1016/j.

newast.2003.08.004. eprint: astro-ph/0303521 (cit. on pp. 28, 41, 44, 47).

Wadsley, J. W., G. Veeravalli, and H. M. P. Couchman (June 2008). "On the treatment of entropy mixing in numerical cosmology". In: MNRAS 387, pp. 427–438. DOI: 10.1111/j.1365-2966.2008.13260.x (cit. on pp. 49, 50).

Walcher, C. J. et al. (Sept. 2014). "CALIFA: a diameter-selected sample for an integral field spectroscopy galaxy survey". In: A&A 569, A1, A1. DOI: 10.1051/0004-6361/201424198. arXiv: 1407.2939 (cit. on p. 7).

Weiner, B. J., J. A. Sellwood, and T. B. Williams (Jan. 2001). "The Disk and Dark Halo Mass of the Barred Galaxy NGC 4123. II. Fluid-Dynamical Models". In: ApJ 546, pp. 931–951. DOI: 10.1086/318289. eprint: astro-ph/0008205 (cit. on p. 7).

Widrow, L. M. and J. Dubinski (Oct. 2005). "Equilibrium Disk-Bulge-Halo Models for the Milky Way and Andromeda Galaxies". In: ApJ 631, pp. 838–855. DOI: 10.1086/432710. eprint: astro-ph/0506177 (cit. on p. 17).

Wozniak, H. (Apr. 2007). "The distribution of stellar population age in galactic bars". In: A&A 465, pp. L1–L4. DOI: 10.1051/0004-6361:20067020. eprint: astro-ph/0701687 (cit. on p. 9).

Zana, T. et al. (Oct. 2018a). "Bar resilience to flybys in a cosmological framework". In: MNRAS 479, pp. 5214–5219. DOI: 10.1093/mnras/sty1850. arXiv: 1805.03658 (cit. on pp. 29, 76).

Zana, T. et al. (Oct. 2018b). "Barred galaxies in cosmological zoom-in simulations: the importance of feedback". In: *ArXiv e-prints*. arXiv: 1810.07701 (cit. on p. 85).

Zana, T. et al. (Jan. 2018c). "External versus internal triggers of bar formation in cosmological zoom-in simulations". In: MNRAS 473, pp. 2608–2621. DOI: 10.1093/mnras/stx2503. arXiv: 1705.02348 (cit. on pp. 29, 58).